Modellierung der Lärmausbreitung für Windparks
Modelling noise propagation for wind farms

Bachelorarbeit
Informatik

Mai 2020

Vorgelegt von Presented by	Laurin Heilmeyer Eisenbahnweg 8 52068 Aachen Matrikelnummer: 345690 laurin.heilmeyer@rwth-aachen.de
Erstprüfer First examiner	Prof. Dr. rer. nat. Erika Ábrahám Lehr- und Forschungsgebiet: Theorie der hybriden Systeme RWTH Aachen University
Zweitprüfer Second examiner	Prof. Dr. rer. nat. Thomas Noll Lehr- und Forschungsgebiet: Software Modellierung und Verifikation RWTH Aachen University
Externer Betreuer External supervisor	Dr. rer. nat. Pascal Richter Steinbuch Centre for Computing Karlsruhe Institute of Technology

Eigenständigkeitserklärung

Hiermit versichere ich, dass ich diese Bachelorarbeit selbständig verfasst und keine anderen als die angegebenen Quellen und Hilfsmittel benutzt habe. Die Stellen meiner Arbeit, die dem Wortlaut oder dem Sinn nach anderen Werken entnommen sind, habe ich in jedem Fall unter Angabe der Quelle als Entlehnung kenntlich gemacht. Dasselbe gilt sinngemäß für Tabellen und Abbildungen. Diese Arbeit hat in dieser oder einer ähnlichen Form noch nicht im Rahmen einer anderen Prüfung vorgelegen.

Aachen, im Mai 2020

Laurin Heilmeyer

Contents

Nomenclature

Physical constants

ρ_N	Normal atmospheric density.	$1.205\,\mathrm{kg/m^3}$
c_0	Normal atmospheric sound speed at $273.15\,\mathrm{K}$.	$331.3\,\mathrm{m/s}$
c_{20}	Normal atmospheric sound speed at $293.15\,\mathrm{K}$.	$343\,\mathrm{m/s}$
I_{ref}	Sound intensity reference value.	$10^{-12}\,\mathrm{W/m^2}$
p_N	Normal atmospheric pressure.	$101\,325\,\mathrm{Pa}$
P_{ref}	Sound power reference value.	$10^{-12}\,\mathrm{W}$
T_N	Normal atmospheric temperature.	$293.15\,\mathrm{K}$

Mathematical symbols

$\hat{}$	Amplitudes.
$\bar{}$	Average.
ln	Natural logarithm with base e.
log	Common (decadic) logarithm with base 10.
$\tilde{}$	Effective value.
$\underline{}$	Complex numbers.
$\vec{}$	Vectors.
H(x)	Heavisides' step function.
sgn(x)	The sign function.

Acoustic parameters

ρ	Sound density.	$\mathrm{kg/m^3}$
ρ_0	Atmospheric resting density .	$\mathrm{kg/m^3}$
σ	Flow resistivity of a given material.	$\mathrm{kg{\cdot}m^{-3}{\cdot}s^{-1}}$
f	Frequency.	Hz
I	Sound intensity.	$\mathrm{W/m^2}$
$L_p(A)$	A-weighted sound pressure level.	dB(A)

$L_{(\cdot)}$	Level of the subscripted $(\cdot)$ parameter.	dB
P	Sound power.	W/m^2
p	Sound pressure.	$Pa = kg/m{\cdot}s^{-2}$
p_0	Atmospheric resting pressure of air.	Pa
Z_0	Characteristic acoustic impedance.	$kg{\cdot}m^{-2}{\cdot}s^{-1}$
Z_a	Acoustic impedance.	$kg{\cdot}m^{-4}{\cdot}s^{-1}$
Z_s	Specific acoustic impedance.	$kg{\cdot}m^{-2}{\cdot}s^{-1}$

List of Figures

VII

VIII

List of Tables

1 Introduction

The rise of renewable energy is hard to deny, not only is the number of electric cars and solar systems in everyday life increasing, but also do statistics from international energy authorities, such as the *International Renewable Energy Agency* [1], confirm the significant trend. This is accompanied by an increasing focus of science and economy on this topic. Besides the motivation for technological progress and profit, also the emerging need to solve harmful side effects of already existing technology fuels this development. One popular technology are wind turbines, which show a global growth, as illustrated in Figure 1. With this increasing number of wind farms, the number of
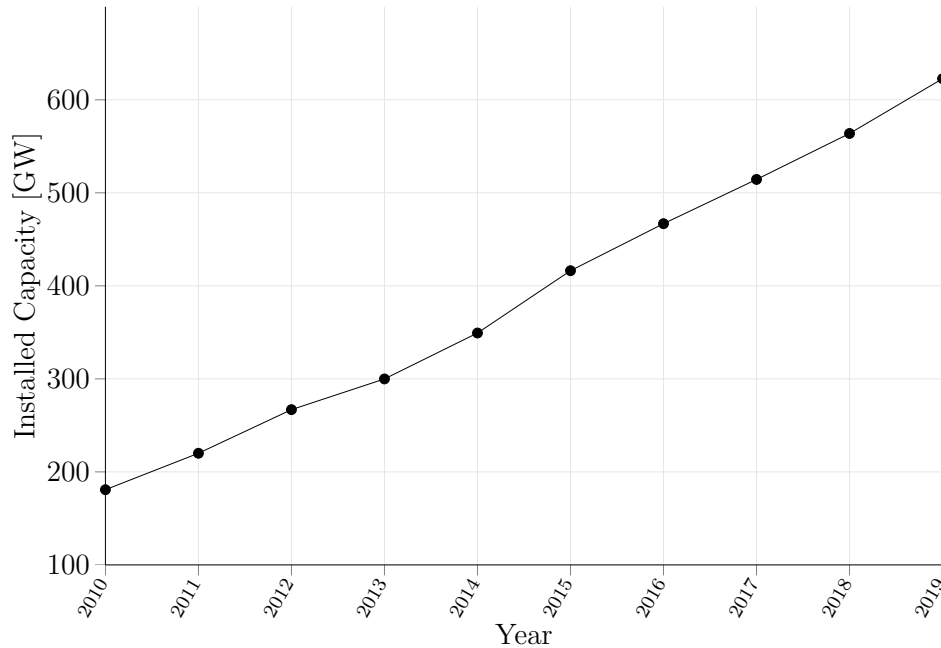
Figure 1: The installed capacity of wind turbines around the world from 2010 to 2019.
[1]

reports concerning health effects or other complaints is increasing as well. In case of wind farms, the main issue is related to noise emission. While the scientific literature does not provide clear evidence of wind farms causing any of the reported problems, the public discussion is heavily involved in this topic. This means, that new wind energy projects are more difficult to implement, due to the critical attitude of locals. From this context and the already existing legal noise immission regulations, the necessity for a model of noise radiation arises. One specific use case consists in the predictive simulation of noise, in order to offer, in the sense of persuasion, the possibility to experience any noise of planned installations before a project is implemented. For such a model, the requirements are special, because broad availability requires few computing resources. This means that the initial problem of this thesis consists of a precise noise propagation model, consuming as little as possible resources and yet account for different customizable environments.

1

1.1 Related Work

Sound prediction models for numerous industrial use cases have been in the interest of environmental engineering for decades. Increasing numbers of wind farms and the noise complaints involved lead to a wide range of new sound propagation models that deal specifically with wind turbines. The following section provides a summary of related work, which had appreciable influence on this thesis.

Starting with what will be designated in this work as the *classical approach*. The term *classical* stems from sound propagation models which have been developed since the 1970s around the same basic formula with more or less refined additions. A well established example of such a model is the DIN ISO 9613-2 [16]. Referring to the empirical nature and the fully analytical solutions to the problem, these kind of models are often referred to as *engineering models*, *analytical models* or *empirical models*. The general principle of this approach includes the direct calculation of total sound pressure level at the receiver location, considering geometric spreading, air absorption, ground impedance, reflections on surfaces and shielding through obstacles. As the name suggests, these influences are mainly calculated with empirically evolved formulas. Prominent examples of this category are *DIN ISO 9613-2* [16], *CONCAWE* [24] and *NMPB-2008* [13]. A more advanced approach but still to be categorized as a classical model, is presented with *Nord2000* by Plovsing [29] and Plovsing and Kragh [30]. It utilizes a semi-analytical method based on geometrical ray theory, to further advanced purely empirical calculations. This model accounts for refraction effects based on wind and temperature gradients. Similar ideas can be found in other models such as the *Harmonoise* [13]. Overall, the problem of classical models is the limited accuracy due to effects that are not easily captured by empirical formulas. Namely, atmospheric turbulent flow cannot be included. Furthermore, the limited flexibility, as they are only applicable to certain situations, is a big disadvantage compared to numerical approaches.

The second category as it appears in the context of this work can be referred to as *numerical models*. Taking into account one example by Prospathopoulos and Voutsinas [31], numerical ray tracing models account for more detailed ground and atmospheric absorption, wave refraction and diffraction especially with atmospheric turbulence. The total sound pressure is obtained from the contribution of the calculated rays at the receiver position, for a given frequency and sound power spectrum of the source. More advanced ray tracers as proposed by McBride and Burdisso [25], include temperature effects, wind speed and air humidity. Apart from ray tracing methods, the parabolic equation (PE) has shown good results for far field noise propagation over large surfaces. Direct comparison to the ISO-9613 model from Kaliski et al. [19] showed, improved results concerning more complex meteorological and topographic conditions. Lee et al. [21] presented a version of the PE method with flow field simulation based on the Reynolds-Averaged Navier-Stokes (RANS) equations. Similar combinations are presented in references [2] and [3]. A great advantage of the numerical models is the

great flexibility and the extensive inclusion of many influences without resorting to empirical values. However, this added value comes from increasing demand for resources and indeterminable boundary conditions which make the application of the models extremely costly.

1.2 Outline

In this thesis a model based on the classical approach is proposed. Regarding the related work described in the previous section, this thesis builds on the foundation of models like the ISO-9613 and especially improves the inflexibility to apply the model to many more situations relevant for wind farms. The goal is to enable an implementation that is executable with only little resources available and not difficult to apply due to many complex input values. Particularly avoidance of complex input values does not refer to values that are difficult to understand but rather to input values that are hardly measurable and therefore prevent the application of many models. For this purpose an introduction to the necessary terminology and principles of acoustic is given in Section 2, followed by the detailed description of the propagation model in Section 3. Subsequently, the model is validated against measurements and compared to relating models in Section 4. Finally, in Section 5 points achieved are summarized and further developments and possible improvements which directly conclude from the prior section are discussed.

2 Technical Acoustics

The term *sound* describes vibrations of a mediums' attributes, which travel through space as a wave. These vibrations are partly perceptible by living creatures, while others are only measurable. We can distinguish between sound in gas, liquids and structure-borne. Regardless in which medium sound waves propagate, it is strongly dependent on the elasticity of it. The medium concerned in this work is air, for the simulation of noise propagation in an outdoor environment. In air sound is an oscillating change of *pressure* and *density*. This means, to describe different kinds of sound, *frequency* and *amplitude* of its underlying vibration is mainly used. In general the physical structure of sound is termed *acoustic* or *sound field*. This denotes the spatial character of sound, which describes a source emitting sound waves, which cause measurable deviations in the medium around the source. For idealized conditions where sound propagates freely without attenuation or other effects, the acoustic field is called *free field*. For complex situations, e.g. indoor the term *diffuse field* labels the acoustic field with high rates of reflection.

For the sake of developing a model for *noise* propagation of wind turbines, the following Section 2.1 introduces fundamental definitions related to sound, explaining tonal concepts and their perception. Subsequently Section 2.2 to Section 2.7 introduce necessary aspects of the acoustic field, including parameters and idealized models to depict real world sound phenomena in sufficient mathematical concepts. The entire chapter is primarily based on Reference [27], Reference [37] and Reference [13].

2.1 Fundamentals

The motivation of this work is based on the human perception of sound. Therefore it is important to distinguish between the physical process of perception and its psychological impact. The physical cause-effect-chain is mathematical comprehensible, variation of pressure in air travels from the source to the receiver and is transformed to neurological signals by a sensory organ. The amount of pressure variation is called sound pressure p, given in the unit Pa and the variation rate is given in frequency f with unit Hz, as the count of vibrations per second. The sound pressure is the cause of what humans perceive as volume, while frequency is the cause of sound quality. The human audible range is about 16 Hz to 16 kHz according to Möser [27], thus it is called *audible sound*. From an engineering's perspective other ranges are relevant as well. Below the audible range, *infrasound* is often considered in construction as it can cause damage in form of structure-borne vibrations. Furthermore *ultrasound*, which identifies the range above 16 kHz, has a broad application scope, from sonar technology to medical diagnosis. This work is mainly concerned about audible sound and infrasound, since a public dialogue addresses correlation of wind turbine infrasound and medical syndromes [35].

4
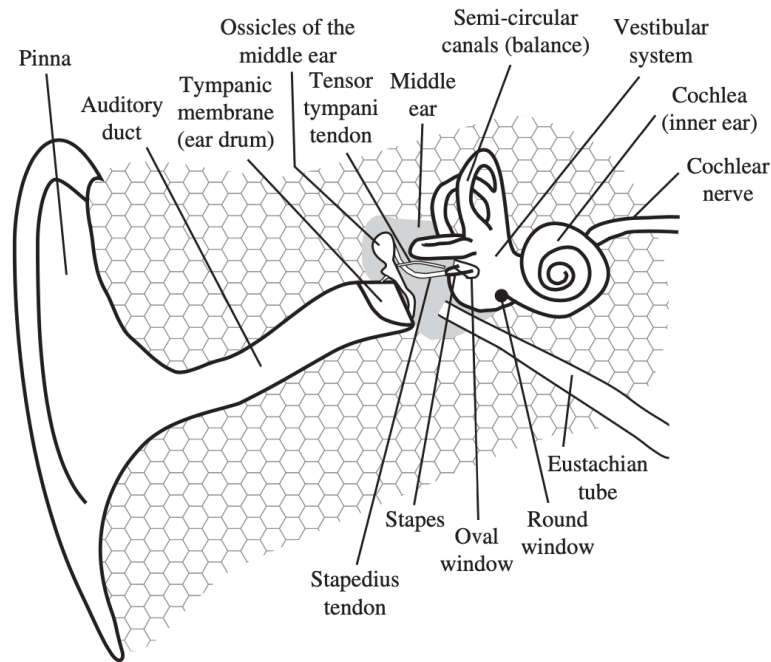
Figure 2: Scheme of the human ear. [13]

2.1.1 Audible Sound

The focus of this thesis is audible sound. In general boundaries of this range are not strict. The upper boundary has multiple influences, which decrease its value with increasing age. Continuous stress or extreme exposure in terms of high pressure can act as amplifications. Referring to Möser [27], the value of 16 kHz refers to healthy individuals at the age of 20 and the decrease rate averages at 1kHz per decade of life. The lower boundary is similar to light, a *critical flicker frequency*. This means below the boundary consecutive sound events are perceived as such, but if the frequencies are above the boundary, events are not perceived apart and become one continual sound. This fact is related to how the human perception of sound works. When sound waves reach the ear, they initially aggregate at the *auricle* and afterwards travel through the *external auditory canal* to the *tympanic membrane*. This membrane transforms the pressure vibration of air into proportional mechanical vibrations, which then travel further as vibrations in the fluid of the *cochlea*. The cochlea is longitudinally divided in two channels by the *basilar membrane*, which contains around 25 000 hair cells on the surface. Vibrations reaching the cochlea travel through the *oval window* membrane along the upper channel, to the apex of the cochlea and back through the lower channel. At the end of the lower channel the *round window* acts as the pressure release for the wave and swallows the vibration. The key part if this transformation chain are the hair cells on the basilar membrane, which get induced by the vibration. The motion of the membrane creates a force on the hair cells, which triggers an electrochemical reaction, which results in an electrically signal through the connected auditory nerve fibers to the brain. The cochlea has no homogeneous structure. Varying thickness of the tissue

5
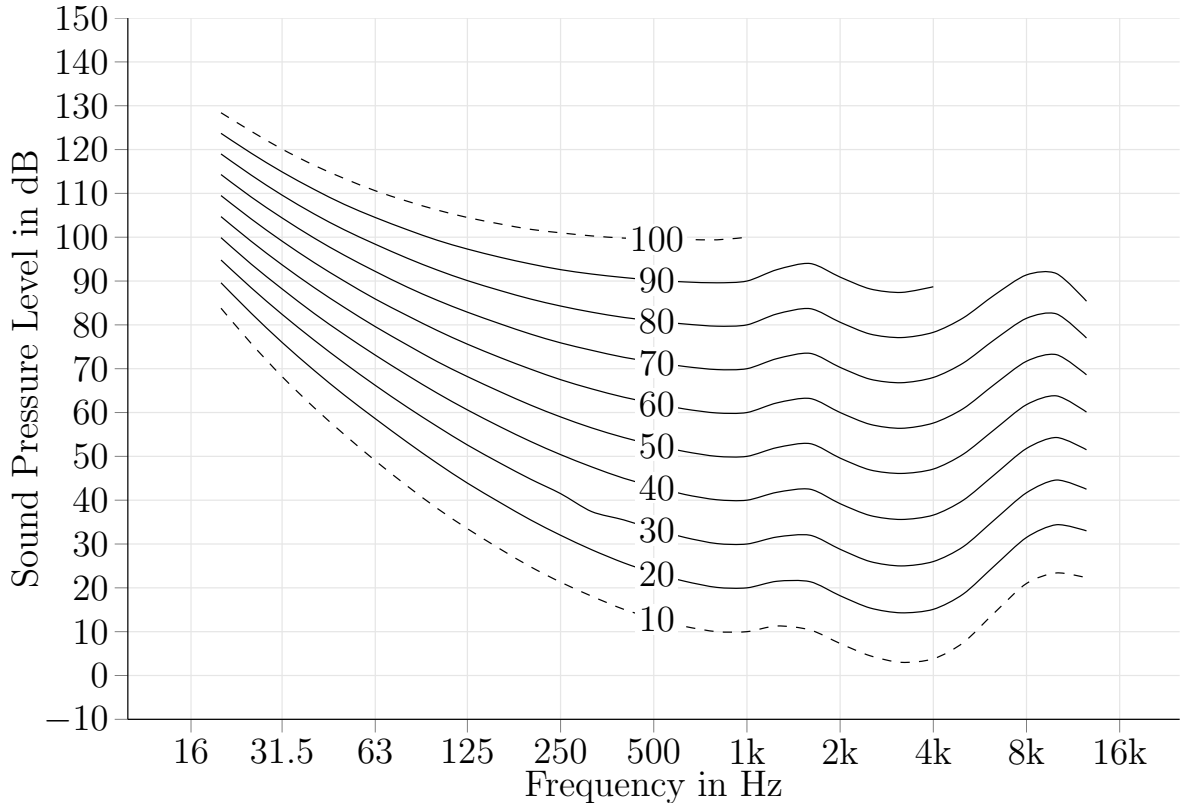
Figure 3: Isophones of tones with equal loudness perception. The curve for 100 phon and for 10 phon are dashed, because there is not enough experimental data available (According to the reference [17]).

leads to different regions respond more strongly than others. While the frequency of the vibrations stays consistent, the size changes. High frequencies cause a stronger reaction at the beginning, starting from the oval window, while lower frequencies peak at the apex. Each auditory nerve fiber is connected to a number of hair cells in a small region on the basilar membrane. The responding fire rate of nerves explains the flickering at lower frequencies, below 16 Hz the fire rate results in distinguishable tones while above the boundary the fire rate translates into continuous sound.

Furthermore sound pressure relates to perceived loudness and frequency relates to pitch. But there is a strict partition of theses parameters. While loudness and pitch are psychological measures, frequency and pressure describe the physical phenomena. As of now there is no precise theory of how the translation between them works. Nevertheless sound pressure is accountable for volume and frequency for pitch. For a psycho-acoustic scale, which is based on empiric measurement and constructed over subjective perception of research participants, *phon* measures the loudness of sound. A value with unit *phon* describes the perceived loudness of a reference sinus tone with a frequency of 1 kHz. The reason of such a scale is the dependence of volume and frequency. Figure 3 shows curves of equal volume perception as *isophones*. It shows that in general the lower frequency, the more pressure is needed for the same volume

(a) Pure tone as an harmonic function of time, with sound pressure on the ordinate and time on the abscissa.

(b) Natural tone as a function of time, with sound pressure on the ordinate and time on the abscissa.
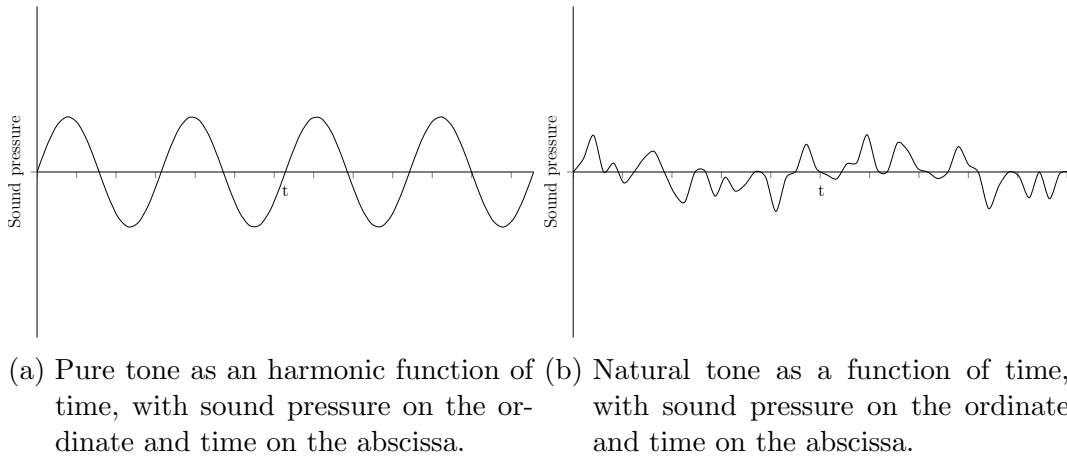
Figure 4: Idealized pure tone and its analogy in the real world. Both denote functions of time.

[17]. As the human ear has limited bandwidth the upper end results in a similar behaviour. In addition to the phon scale, the *sone* scale is used to compensate the fact that phon is not proportional to perception. A sound event with 40 phon doubles the volume perception of a sound event with 50 phon. Therefore, the sone scale assigns 1 sone to 40 phon and then increases in proportional steps to perceived loudness. This means 2 sone doubles the volume and 4 sone quadruples the volume. The choice of such a scale includes as well, that the volume perception is proportional to the logarithm of physical parameters. Because the basilar membrane has its strongest motion only for some regions, these regions are associated with a range of frequencies. Precisely the *characteristic frequency* determines the point of most sensitivity for a nerve and the *critical band* determines the width of frequency ranges, where tones with slightly different frequencies are not distinguishable. The bandwidths of each critical band increases with frequency and correlates with the magnitude of the sound wave, but in general low frequencies have higher resolution with less sensitivity. For that reason the technical description of sound is based on the idea, that complex sound consists of a spectrum of single frequency tones. The idealized concept is the *pure tone*, with a periodic change of pressure and a single frequency. Mathematical speaking a pure tone is a sinusoidal or cosinusoidal function. In contrast the *natural tone* is a periodic change of pressure, but composed of multiple higher (harmonic) frequencies of lower amplitude. These two terms should be carefully distinguished, since the natural tone is perceived as a pure tone by humans, but both terms are often simply referred to as a tone. Figure 4 illustrates the difference of the natural tone in 4b and the pure tone 4a. Figure 5 shows the corresponding composition. This fact is the reason that arbitrary acoustic processes can be disassembled in its frequency spectrum.
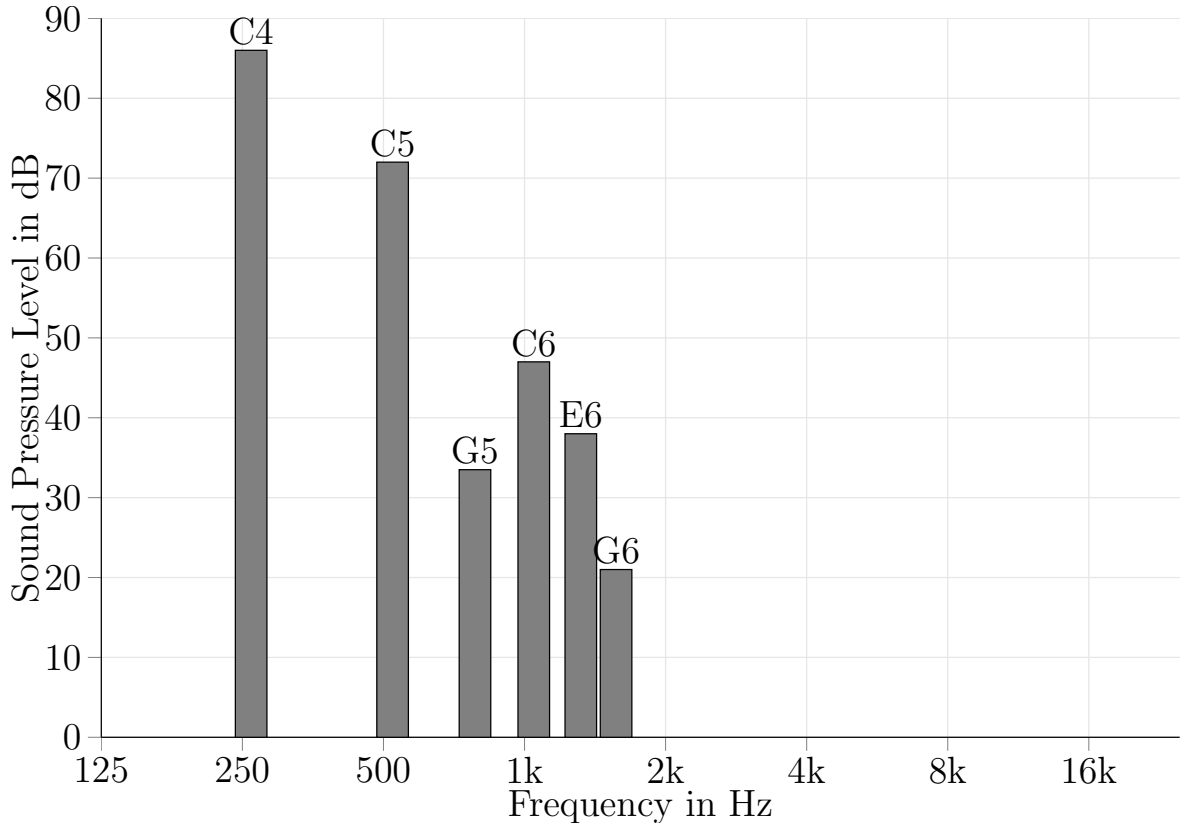
Figure 5: The discrete spectrogram of the natural C4 played by a piano. On the abscissa is sound pressure amplitude in dB and on the ordinate the center frequency of the resonating musical note.

2.1.2 Frequency Filters

The human pitch perception of sound introduces the concept of frequency *weighting filters*. As already discussed frequency is related to pitch. However the perception is based on frequency ratio not differences. The difference between two tone pairs is perceived as equal, if the frequency ratio is equal. In combination with the discrete nature of audio nerves, sound frequencies are often discretised or *filtered*. The term *filter* describes the projection of frequencies into ranges with one center frequency. One example is the musical scale of octaves, where one octave doubles the frequency and is denoted with same note and changing subscript. Figure 4 illustrates that with the note C_4. In technical matters for different resolutions, different filters are used. Most common acoustic filters are the octave, one-third octave and narrow band filter with the *Fast Fourier Transform Analysis* (FFT). In general a filter is characterized by its bandwidth Δf, the bottom boundary f_B, the upper boundary f_U and the center frequency f_c. The bandwidth equals the difference $f_U - f_B$ and is proportional to the center frequency as in Equation (1). Therewith it's sufficient to specify the ratio of

8
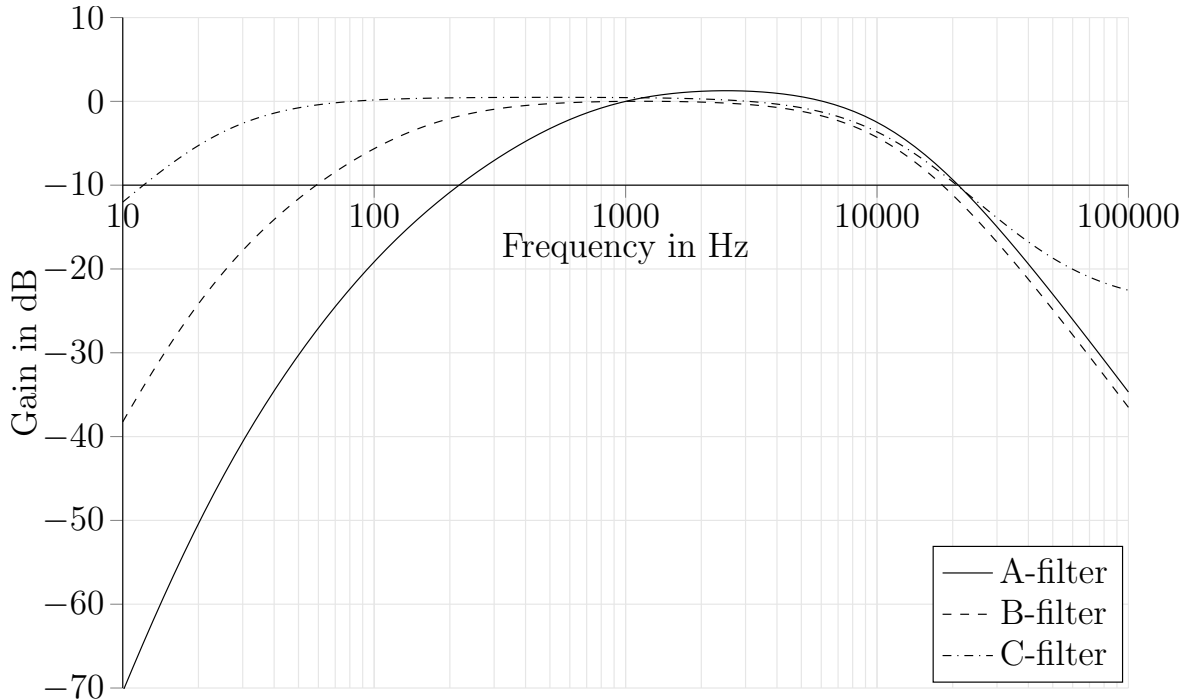
Figure 6: Filter curve of the A,B,C-filter.

boundaries to determine the filter,

$$f_c = \sqrt{f_U f_B}. \tag{1}$$

Referring to DIN [10], the octave filter doubles the bottom boundary in the upper boundary as written in Equation (2). The one-third filter is determined by Equation (3). The naming derives from the fact that three partitioned one-third bands make up one octave band,

$$f_U = 2f_B \Longleftrightarrow f_c = \sqrt{2}f_U, \Delta f = \frac{f_c}{\sqrt{2}}, \tag{2}$$

$$f_U = \sqrt[3]{2}f_B \Longleftrightarrow f_c = \sqrt[6]{2}f_U, \Delta f = (1 - \sqrt[3]{2})f_U. \tag{3}$$

The use of different filters has obvious impact on measurements. When using a broad-band filter compared to a narrow-band one, values tend to be higher because of the higher center frequencies. That's why the specification of the used filter in case of measurements is mandatory. In order to mimic the human frequency resolution, the *A-filter* is commonly used [17]. In contrast to prior mentioned band-pass filters, the A-filter is used to weight certain frequencies, to imitate the sensitivity of the human ear. This filter is based on the inverse of the volume perception curve in Figure 3, with 30 dB and 1 kHz. The values of the filter are named *a weighted noise level*. The corresponding unit is Decibel(A) [dB(A)] with a trailed capital A. Basically the filter adds (amplifies) and subtracts (attenuates) certain amounts based on the loudness curve. For higher frequencies other filters are used, denoted by capital B, C and D. While

9
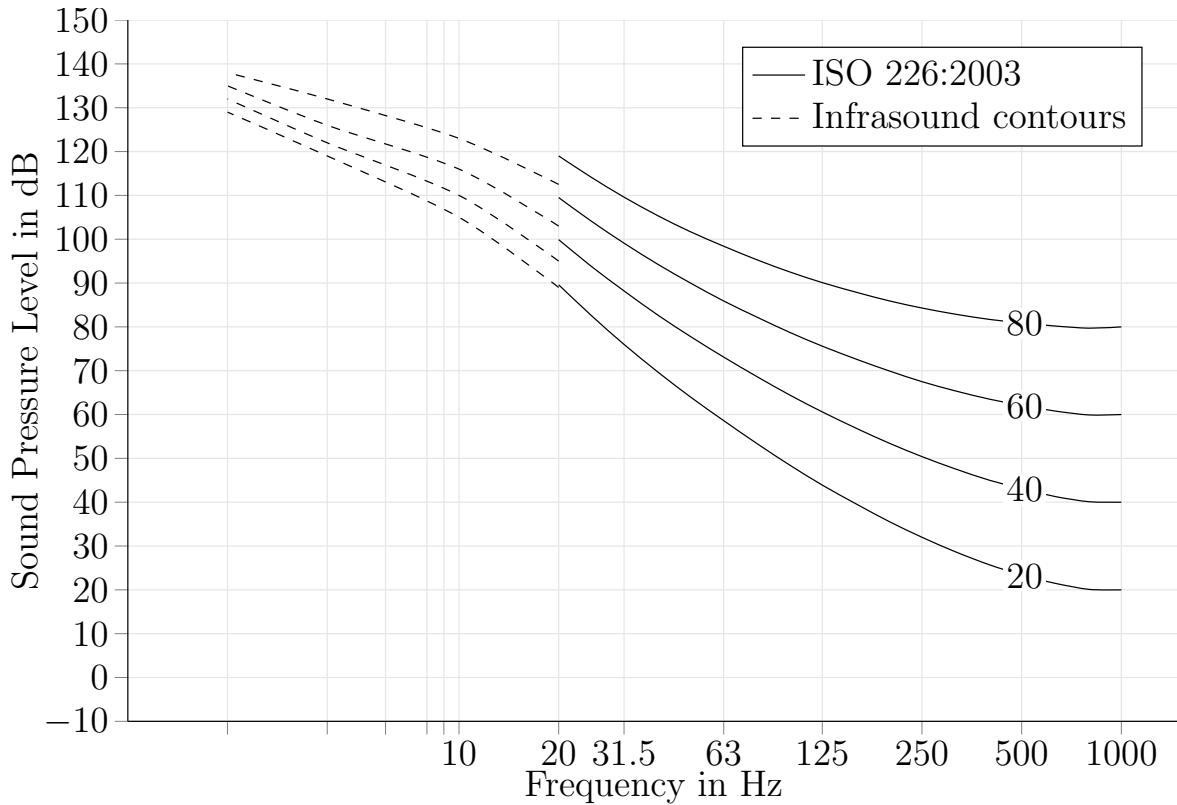
Figure 7: Extended loudness curves for infrasound at 20, 40, 60 and 80 phon. Data is approximated according to Møller and Pedersen [28].

only the A-filter is broadly adopted, it is needles to say that the complex perception process of humans can't be adequately represented by A-weighted values. While at the limit of 20 kHz nothing is weighted, band-pass filters often take the frequency portion above this limit into account, which produces unreasonable high values. Furthermore low frequent portions result in a very high attenuation, contrary the cognition depicted in 3.

2.1.3 Infra Sound

Typically, the lower limit of the audible range is given as 16 Hz or 20 Hz and the frequency region below is labelled as infra sound. Technically, infrasound differs from the audible range because of its longer wave length, which results in less attenuation or acoustic shielding. Concerning the human perception of infra sound, the border to audible sound is rather broad in contrast to the upper limit and according to Møller and Pedersen [28], all humans are able to perceive sound around a few Hertz. Nevertheless the threshold for pressure is increasing for decreasing frequency, which reduces natural occurrences of this kind of perceptible infra sound. However natural sources exist. Besides thunder and earthquakes, people are exposed to $10 - 20$ Hz sounds when driving a car with open window at a certain speed. Furthermore the perception of sound

drastically changes below 20 Hz. Cognition of pitch and the general tonal character disappears, replaced by the perception of pressure at the ear drum. In addition rather than continuous sound, it is perceived as flickering beats. Most importantly, in the outdoor free acoustic field, it is difficult to produce high sound pressure for infrasound to be perceptible. Studies (Figure 7) show, that for pure tones in the free field below 16 Hz, pressure levels up to 120 dB are the threshold. Referring van Kamp and van den Berg [36] most studies show that infra sound produced by wind turbines is not audible. Measurements of real wind turbines showed that the audible threshold for frequencies below 20 Hz are significantly undercut. Furthermore, Yokoyama et al. [38] documented in a laboratory environment, that wind turbine sound where infrasound frequencies were filtered out, could not be differentiated by the participants from the original sound. Other effects which occur in public discussion and scientific literature, mention *annoyance* and *health* effects. As stated in van Kamp and van den Berg [36], Bolin et al. [6] there is no evidence that wind turbine infra sound contributes directly to neither of these.

2.2 Basic Parameters

Most parameters in this context describe the instantaneous value of a periodic change. Therefore corresponding symbols, if not stated otherwise, denote the difference towards the resting value and not the total value. Unless explicitly stated otherwise in the context, subscript zeros indicate the average ambient values of a parameter. For example, p_0 usually indicates the average ambient pressure of an inhomogeneous medium such as air. While most parameters are defined as functions of time and location or as vectors, it is important to note that often times the root mean square or instantaneous value of time and location is implicitly used in calculations if not denoted otherwise. This circumstance is due to the fact that for periodic operations or directional variables in certain contexts only the amount is of interest for interpretation. Usually, the root mean square is symbolized by a superscript tilde. For any vector the arrow notation $\vec{\cdot}$ is used. For periodic functions the use of complex amplitudes is denoted with an underline of symbols, e.g. $\underline{\cdot}$.

2.2.1 Acoustic Field Parameters

In air sound is the oscillation of its particles, thus a repeating change of pressure. This deviation of the resting pressure p_0 is called *sound pressure* and denoted with p and the deviation between ρ and ρ_0 is called *sound density*. The movement of the mediums' particles is called *sound particle velocity*. In the international system of units (SI), pressure is expressed in Pa, sound density is measured in kg/m^3 and sound speed in m/s. In comparison with the static air pressure, which is around 10^5 Pa, the sound pressure of common sound events are relatively small, e.g. the human auditory pain threshold is commonly named as 200 Pa, while sound that is barely audible has around 2×10^{-5} Pa (at 1 kHz)[22]. The fact that the human range of audible sound has such a large domain of values when describing acoustic fields leads to the use of a logarithmic

scale. Corresponding values are measured in levels and have the unit decibel, leading to the human audible domain of 0 to 140 dB. The sound pressure level (SPL) L_p is based on the human auditory threshold with $p_{\text{ref}} = 2 \times 10^{-5}$ Pa as the reference value. Because of the logarithmic scale, sound pressure levels of different sound sources are not simply aggregate by addition. If n sound sources are incoherent, that is if the waves have no related phases, the total sound pressure level L_{tot} can be calculated with Equation (5). In case of n equal sound pressure levels L_{tot} can be simplified to Equation (6),

$$L_p = 20 \ \log\left(\frac{p}{p_{\text{ref}}}\right) = 10 \ \log\left(\frac{p^2}{p_{\text{ref}}^2}\right) \ , \tag{4}$$

$$L_{\text{tot}} = 10 \ \log\left\{\sum_i^n \left(\frac{p_i}{p_{\text{ref}}}\right)^2\right\} = 10 \ \log\left(\sum_i^n 10^{\frac{L_{p_i}}{10}}\right), \tag{5}$$

$$L_{\text{tot}} = L_p + 10 \ \log_{10}(n). \tag{6}$$

In addition, for time variant sounds, the *energy equivalent continuous sound level L_{eq}* allows for comparison, by calculating the root mean square of the ratio between effective pressure and the reference value p_{ref},

$$L_{\text{eq}} = 10\log\left(\frac{1}{T}\int_0^T \frac{\tilde{p}^2(t)}{p_{\text{ref}}^2}\mathrm{d}t\right) = 10\log\left(\frac{1}{T}\int_0^T 10^{\frac{L(t)}{10}}\mathrm{d}t\right). \tag{7}$$

Finally, *sound volume flow* q correlates the impacted area with particle velocity. Sound volume flow quantifies the volume of the medium which moves through the enveloping surface. If the particle velocity is consistent over the whole area, it can be simplified to product of effective velocity and impact area,

$$q = \int_S \vec{v} \cdot d\vec{S}. \tag{8}$$

Outdoor sound fields are considered rotation-free regarding the particle velocity $\vec{v}$. Assuming $\text{rot}(\vec{v}) = 0$ one can use a velocity potential $\vec{v} = \text{grad}(\Phi)$ which simplifies calculation in some cases.

2.2.2 Energy Field Parameters

The moving oscillation of the mediums particles described by the wave equations in Section 2.3 implies energy transport. Compression of the medium and acceleration of particles premises potential energy. Considering the linear hook principle for the finite gas mass (Fig. 8), this energy E is equal to a proportional factor s and the compression force F. Replacing $F = p \cdot S$ and $s = \frac{E \cdot S}{\Delta x} = \frac{\rho_0 c^2 S}{\Delta x}$, with the mediums' modulus of elasticity E, one gets Equation (9) for the potential energy. In terms of kinetic energy Newton provides the corresponding rule and leads to Equation (10) and overall that leads to *sound energy* in Equation (11). Conceptual every particle

has energy, therefore one can take the infinitesimal volume and name the relating parameter *energy density* $E = \frac{E_V}{V}$,

$$E_{pot} = \frac{1}{2}\frac{F^2}{s} = \frac{1}{2}\frac{p^2 S^2 \Delta x}{\rho_0 c^2 S} = \frac{1}{2}\frac{p^2 V}{\rho_0 c^2}, \tag{9}$$

$$E_{kin} = \frac{1}{2}mv^2 = \frac{1}{2}\rho_0 v^2 V, \tag{10}$$

$$E_V = \frac{1}{2}(\frac{p^2}{\rho_0 c^2} + \rho_0 v^2) \cdot V, \tag{11}$$

$$E = \frac{E_V}{V} = \frac{1}{2}(\frac{p^2}{\rho_0 c^2} + \rho_0 v^2). \tag{12}$$

As a consequence, the energy travels in form of a wave as well. In case of a generic function for pressure $p = f(t - \frac{x}{c})$, the sound energy is described by $E(x,t) = \frac{p^2}{\rho_0 c^2} = \frac{1}{\rho_0 c^2}f^2(t - \frac{x}{c})$. As one can observe, the energy travels in a quadratic relation to the pressure function. In practice, it is sufficient to consider the principle of energy conservation. The correlation of energy with sound pressure is related to *performance*. In order to explain this term, one can refer again to the finite gas mass, where the out flowing energy is in point $x + \Delta x$ equals to $I(x + \Delta X)S\Delta t$ and the in flowing $I(x)S\Delta t$ in point x. The Difference between inflow and outflow has to be $VE(t + \Delta t) - VE(t)$, leading to Equation (13),

$$S\Delta x(E(t + \Delta t) - E(t)) = S(I(x) - I(x + \Delta x))\Delta t. \tag{13}$$

After dividing with $S\Delta x\Delta t$ and approaching Δx, Δt to zero one gets $\frac{\partial I}{\partial x} = -\frac{\partial E}{\partial t}$. Inserting energy density E, make use of the chain rule $\frac{\partial p^2}{\partial x} = 2p\frac{\partial p}{\partial x}$ and use the law of inertia (36) leads to Equation (14),

$$\frac{\partial I}{\partial x} = p\frac{\partial v}{\partial x} + v\frac{\partial p}{\partial x} = \frac{\partial(pv)}{\partial x}. \tag{14}$$

After integration one gets sound intensity overall in all three dimensions. One gets Equation (15) for the *sound intensity*,

$$\vec{I} = p \cdot \vec{v}, \tag{15}$$

$$P = \int \vec{I} \cdot d\vec{S}. \tag{16}$$

Finally the performance in the impacted area S is then described by Equation (16), where S is the perpendicular surface vector. Conveniently, for sound intensity and performance, there is a index scale as well, with $I_{\text{ref}} = 10^{-12}\,\text{W/m}^2$ and $P_{\text{ref}}10^{-12}\,\text{W}$.

2.2.3 Sound Speed

The disciplines of *aerodynamics* provide the necessary correlations of sound pressure, sound density and medium temperature T to determine the acoustic field. First of all, the high velocity of sound particles makes the correlation adiabatic, which means there is no exchange of energy in form of heat with the environment. This fact provides the Adiabatic Formula (17), with κ as the adiabatic exponent, which is the quotient of heat capacities with constant volume c_V and constant pressure c_P.

$$\frac{p}{p_0} = \kappa \frac{\rho}{\rho_0} \tag{17}$$

$$\kappa = \frac{c_v}{c_p} \tag{18}$$

By solving the adiabatic formula (17) for density and replacing $\kappa \frac{p_0}{\rho_0}$ with c^2, the resulting Equation (19) introduces a new parameter c. Resolving the equation for c, and replacing the quotient of pressure and density with the Boyle-Mariotte-Equation (20), where R is the ideal gas and M_{mol} the molar mass of air. This leads to Equation (21),

$$\rho = \frac{p}{c^2}, \tag{19}$$

$$p = \frac{R}{M_{mol}} \rho T, \tag{20}$$

$$c = \sqrt{\kappa \frac{R}{M_{mol}} T}. \tag{21}$$

Evidently parameter c describes the sound speed and considering the composition of air $M_{mol} \approx 28.8 \frac{g}{mol}$ and temperature $T = 288\,\text{K}$, sound travels with $c \approx 341\,\text{m/s}$ through air.

2.2.4 Acoustic Impedance

The term *acoustic impedance* has a close analogy to electrical impedance. In the sense of physical meaning, the term refers to the resistance of the medium, to the cause of the particle oscillation. However, in acoustics several impedance terms are used for different relations. The general term acoustics impedance refers to the ratio of sound pressure and particle velocity at a surface area. Thereby, it is written as ratio of sound pressure and sound volume flow in Equation (23). Note, S refers to the impacted area as in Equation (8). The term *specific* acoustic impedance is written in Equation (23) and refers to the ratio of sound pressure and particle velocity at a certain point instead of surface area S. For sound radiators, a *mechanical acoustic impedance* Z_m in Equation (24) may be used. Here, the applied force, which is causing the wave oscillations is set in proportion with particle velocity.

Independent of the mathematical definition, impedance is important when describing the strength of sources and effects at medium boundaries. Furthermore it should be

noted for plane waves, pressure and velocity have equal phase. This results in a specific impedance, that is equal to the product of sound speed and density. In this particular case the specific impedance is called *characteristic* acoustic impedance Z_0. For normal dry air with $T = 293.15\,\text{K}$, that is $c_N = 343.4\,\text{m/s}$ and $\rho = 1.204\,\text{kg/m}^3$ one gets $Z_0 = 413.5\,\text{kg·m}^{-2}\text{·s}^{-1}$. In comparison to water under similar conditions one gets $Z_0 = 1.48 \times 10^6\,\text{kg·m}^{-2}\text{·s}^{-1}$,

$$\underline{Z}_a = \frac{\underline{p}}{\underline{q}} = \frac{\underline{Z}_s}{S}, \tag{22}$$

$$\underline{Z}_s = \frac{\underline{p}}{\underline{v}}, \tag{23}$$

$$\underline{Z}_m = \frac{\underline{f}}{\underline{v}}, \tag{24}$$

$$Z_0 = \rho_0 \cdot c. \tag{25}$$

As seen in the above equations, the acoustic impedance term can given as a complex parameter. Thus, the real part of the impedance $\text{Re}\{Z_a\}$ is called *acoustic resistance* and the imaginary part $\text{Im}\{Z_a\}$ *acoustic reactance*. While the resistance analogously to electricity determines the energy loss of the system, the reactance determines the resonation of the mediums' mass. This means in the context of a sound source, the reactance determines the additional load for the sound source in the near field, while the resistance determines the radiated energy in the far field.

2.2.5 Directional Radiation

The *directional factor* $\underline{\Gamma}$ is the ratio of two different far field pressure amplitudes with equal distance to the source, but different angles. Therefore the denominator defines a point of reference with φ_0 and θ_0 and the same radius as the nominator. In practice the point of reference is usually the direction of maximum emission and the root mean square of pressure amplitudes is used. In addition the *direction degree* Γ^2 names the square of the direction factor and the *directional gain* is the relating index parameter,

$$\Gamma = \frac{\tilde{p}(\varphi, \theta)}{\tilde{p}(\varphi_0, \theta_0)}, \tag{26}$$

$$D = 10 \cdot \log\left(|\Gamma|^2\right) = 20 \cdot \log(\Gamma). \tag{27}$$

The *statistical direction factor* Γ_s defines the ratio of pressure amplitudes with angle φ and θ to the root mean square of the pressure amplitude of all directions with the same distance. The *direction impact measure* G is the relating level unit,

$$\Gamma_s = \frac{\tilde{p}(\varphi, \theta)}{\sqrt{\tilde{p}(\varphi, \theta)}}, \tag{28}$$

$$G = 20 \cdot \log \Gamma_s. \tag{29}$$

The *directivity factor* γ is the ration between the sound power of a reference zero order spherical radiator, with omnidirectional uniform emission and a real source. The emission of the reference source is set to the maximum of the real source. Furthermore the directivity factor equals to the ratio of the statistical direction factor and direction degree. This parameter describes how much the source concentrates it emitted sound power in certain direction. Thus, on the one hand the monopole source has a $\gamma = 1$ and on the other hand, a dipole source has a $\gamma = 3$. The *directivity index* names the relating logarithmic unit,

$$\gamma = \frac{P_{\text{ref},\tilde{p}_{\max}}}{P_{\text{real}}} = \frac{\Gamma_s^2}{\Gamma^2}, \tag{30}$$

$$d = 10 \cdot \log(\Gamma). \tag{31}$$

For graphical representation the *directional characteristic* is the polar diagram of the directional parameters. For a constant distance and frequency the diagram displays any parameter depending on the emission angle.

2.3 Wave Equations for Sound in Gases

Altogether, the acoustic field describes fluctuations of the mediums resting values, that travel through gases as nondispersive and longitudinal waves. This behaviour is illustrated finitely with a gas mass representing the medium in Figure 8. The wave travels with speed c, while the affected particles themselves have a velocity and direction $\vec{v}$. For illustration, Figure 8 has a small Δx, which is of infinitesimal length in reality. For the sake of simplicity, the following formulas are derived for one dimensional waves in positive x direction and afterwards extended in three dimensions. While the mass
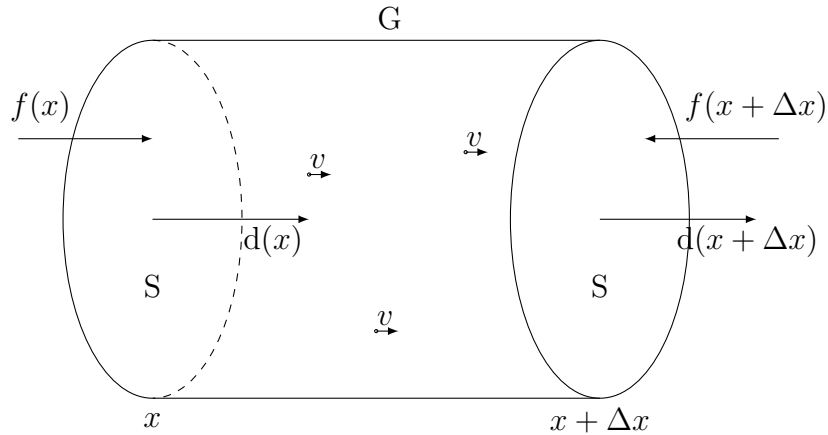
Figure 8: A finite gas body G with length Δx, a deformation $d(x)$ of the left surface and a deformation $d(x + \Delta x)$ of the right surface. By having a finite body the calculation can be described with mass, volume and surface S.

of the medium is unchanged, a force f is causing a deformation, leading to a change of density. Before this force is applied, the mass of G is $\rho_0 V = \rho_0 S \Delta x$. With the deviation of density $\rho_g = \rho_0 + \rho$, the mass of G gets equal to $\rho_g S(\Delta x + d(x + \Delta x))$.

The precondition of no change of mass leads to Equation (32), where the resting mass is equal to the impacted mass. By dividing with S one gets Equation (33), in which one can neglect the relative small $\rho(d(x+\Delta x) - d(x))$ in favour of the remaining terms. In consequence one gets Equation (34) for infinitesimal density $\Delta x \to \mathrm{d}x$,

$$(\rho_0 + \rho)(\Delta x + d(x + \Delta x) - d(x))S = \rho_0 \Delta x S, \tag{32}$$

$$\rho \Delta x + \rho_0(d(x + \Delta x) - d(x)) + \rho(d(x + \Delta x - d(x)) = 0, \tag{33}$$

$$\frac{\rho}{\rho_0} = -\frac{\partial d(x)}{\partial x}. \tag{34}$$

Thereby, the sound density is equal to the negative deformation for $\Delta x \to \mathrm{d}x$. By replacing the deformation with the particle velocity $v(x,t) = \frac{\partial d}{\partial t}$ and $\rho = p/c^2$ as is customary, one gets the *continuity law* of acoustics written in Equation (35). Lastly Newton's *law of inertia* states, that the velocity of which particles move is dependent on the force $f(x)$ and the antagonistic force $f(x + \Delta x)$. The acceleration is higher for a lower mass of particles. This correlation provides the law of inertia for acoustics, in Equation (36), with mass written as the product of volume times density. Since in most waves the pressure and particle velocity have the same form, it is practically to replace the deformation d with $v = \frac{\partial d}{\partial t}$ and for reasons of consistency $\rho = \frac{p}{c^2}$. In total these equations formulate the rules for sound wave propagation. For a more compact form, the combination of both laws provide the one dimensional acoustic wave equation for gases in Equation (37),

$$\frac{\partial v}{\partial x} = -\frac{1}{\rho_0 c^2}\frac{\partial p}{\partial t}, \tag{35}$$

$$\rho_0 \frac{\partial v}{\partial t} = -\frac{\partial p}{\partial x}, \tag{36}$$

$$\frac{\partial^2 p}{\partial x^2} = \frac{1}{c^2}\frac{\partial^2 p}{\partial t^2}. \tag{37}$$

Lastly, it is necessary to extend the acoustic field in three dimensions. Therefore simply the deformation in the missing directions is extended, which leads to the new continuity Equation (38),

$$\frac{1}{\rho_0}\frac{\partial p}{\partial t} = -\frac{\partial v_x}{\partial x} - \frac{\partial v_y}{\partial y} - \frac{\partial v_z}{\partial z}. \tag{38}$$

The law of inertia can be extended in a similar way, by calculating the correlation component wise in Equation (39),

$$\rho_0 \frac{\partial v_x}{\partial t} = -\frac{\partial p}{\partial x}, \tag{39a}$$

$$\rho_0 \frac{\partial v_y}{\partial t} = -\frac{\partial p}{\partial y}, \tag{39b}$$

$$\rho_0 \frac{\partial v_z}{\partial t} = -\frac{\partial p}{\partial z}. \tag{39c}$$

One gets the three dimensional acoustic wave equation in Equation (40), by deriving the law of inertia and introducing that into the derivation of the continuity equation, with respect to t. For a more compact notation one can use the divergence operator div and gradient operator grad,

$$\frac{\partial^2 p}{\partial x^2} + \frac{\partial^2 p}{\partial y^2} + \frac{\partial^2}{\partial z^2} = \frac{1}{c^2}\frac{\partial^2 p}{\partial t^2} = \Delta p = \frac{1}{c^2}\frac{\partial^2 p}{\partial t^2}, \tag{40}$$

$$\mathrm{div}(v) = -\frac{1}{\rho_0 c^2}\frac{\partial p}{\partial t}, \tag{41}$$

$$\mathrm{grad}(p) = -\rho_0\frac{\partial v}{\partial t}. \tag{42}$$

If parameters are assumed to be harmonic, i.e. representable by sine or cosine functions, the wave equations can be formulated in the so-called *Helmholtz equations*. Through these simplifications the above wave equations can be written in Helmholtz form, as shown in Equation (43), with the *Laplace* operator. Thus, the relationships resulting from the law of inertia Equation (42), can be rewritten as in Equation (44). The correlation between density and pressure can be rewritten as in Equation (45),

$$\triangle \underline{p} = -k^2\underline{p}, \tag{43}$$

$$\underline{v_i} = -\frac{1}{j\omega\rho_0}\frac{\partial \underline{p}}{\partial x_i}, \tag{44}$$

$$\underline{\rho} = \frac{\underline{p}}{c^2}. \tag{45}$$

2.4 Solutions to the Wave Equations

In general arbitrary functions with $t \pm \frac{x}{c}$ denoted for pressure in Equation (46) are solutions to the wave equations. However, for this thesis the use of harmonic functions is sufficient and offers many advantages. While the model is concerned with noise, which has a broadband spectrum of frequencies, the concept of decomposition in harmonic functions offers a easily implementable basis.

$$p(x,t) = f(x \pm \frac{x}{c}) \tag{46}$$

Harmonic solutions of the Helmholtz equations are preferably notated in the more compact notation of complex amplitudes. Figure 9 illustrates an one dimensional pressure distribution in positive x direction, which is denoted in Equation (47) as a cosine function,

$$p(x,t) = \hat{p}\cos\left(\omega t - kx + \varphi_0\right). \tag{47}$$

Therefore, t is the time in seconds, x the distance in meters, $\omega = 2\pi f$ the angular frequency with frequency f in Hertz and c the propagation speed of sound in meters per second. The variable $\hat{p}$ denotes the pressure amplitude and in literature the *wave*
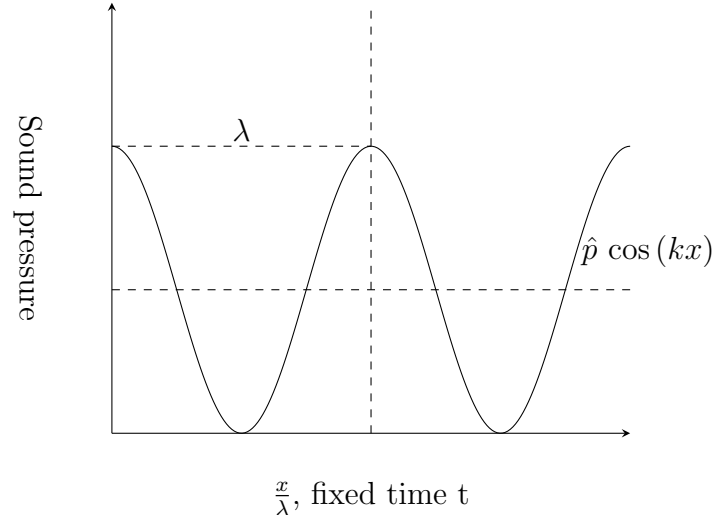
Figure 9: Progressively moving wave in x-direction.

number $k = \frac{\omega}{c}$ is typically used. This way, the change of phase related to time can be denoted with the term ωt and the change of phase related to location with the term kx. Finally, φ_0 is occasionally added as the *zero phase angle*, for an initial offset. As shown in Figure 9 the location variable $\lambda = \frac{c}{f}$ is the analogue of time period $T = \frac{1}{f}$, to denote the distance of one period. The preferred notation based on the *euler equations* is denoted in Equation (49). By convention, the real part of the complex amplitude is interpreted as the harmonic wave function. It should be noted that in literature usually, a wave propagating in positive x direction is notated with a negative sign in the exponent,

$$e^{\pm ix} = \cos(x) \pm i\sin(x), \tag{48}$$

$$p(x,t) = \mathrm{Re}\{\hat{p}e^{\pm j(kx+\omega t)}\}. \tag{49}$$

2.4.1 Plane Spreading

Plane progressive waves get their name from plane wave fronts with a flat propagation. The pressure is in phase with the particle velocity. Therefore the specific impedance of the field is equal to the characteristic impedance $Z_0 = c \cdot p_0$ and has a real value. In addition, direction of sound intensity I is parallel to propagation direction and the mean value can be calculated with pressure and particle velocity or as the product of energy density and sound speed,

$$Z_s = Z_0 = \rho_0 c, \tag{50}$$

$$I = p \cdot v = Z_0 \cdot v^2 = \frac{p^2}{Z_0}. \tag{51}$$

2.4.2 Spherical Spreading

In most outdoor cases sound sources produce *spherical fields*, which can be naturally denoted in a spherical coordinate system. The radius r describes the distance from the source, with azimuth angle ϕ and declination angle θ. Assuming waves with concentric and consistent wave fronts, Equation (53) formulates a solution for pressure, with parameter A usually determined by the source strength. This idealised symmetric acoustic field only occurs with an idealized source called *zero order radiator* (See Section 2.7), consisting of a constant radial expanding and contracting sphere, with particle velocity v. In spherical emission the wave fronts equate to spherical shells, which come towards plane fronts with growing distance. For $\lambda < r$ the acoustic field is called *near field*, for $\lambda > r$ *far field*. In this context the *Helmholtz number He* as the ratio of radius to wave length is used to differentiate near and far field,

$$He = k \cdot r = \frac{2\pi f}{c} r = \frac{2\pi r}{\lambda}. \tag{52}$$

In general near sound fields have high portion of reactive power with less effective power. That is because 90° phase shift of pressure and particle velocity. In consequence the acoustic impedance Z in the near field is different from the far field, where the wave fronts approximate to planes and the situation in Section 2.4.1 applies. In the near field the phase difference results in Equation (54) for the field impedance. As a result, the amount of sound intensity can be calculated as the product if effective pressure and particle velocity or as the quotient of pressure and acoustic impedance,

$$p = \frac{A}{r} e^{-jkr}, \tag{53}$$

$$Z = Z_0 \frac{jkr}{1 + jkr}. \tag{54}$$

2.5 Boundary Effects

Since real mediums are not indefinite and sound propagation is strongly dependent on properties of its medium, different effects occur when sound waves cross the borders. Intuitively expressed, the more different the properties of the mediums, the heavier are the changes to the wave. In the context of this work important effects are *reflection*, *refraction*, *diffraction* and *absorption* of sound waves. All these effects do occur in combination or separately. Reflection refers to the throw back of a wave at a boundary surface, refraction refers to the bending of a wave at an interface and diffraction refers to the bending at obstacles.

In the boundary layer of different mediums the wave has to full fill the condition of continuity, which means the pressure and particle velocity in the first medium has to be equal to the pressure and particle velocity in the second medium. However, with different characteristic impedance values, the ratio of particle velocity and pressure changes. This fact is compensated with a reflection wave, which makes the acoustic

field in front of the border a composite of two waves, the incoming and the reflected. At the same time a part of the sound energy passes into the second medium and a transmission wave travels through the second medium. Figure 10 illustrates the
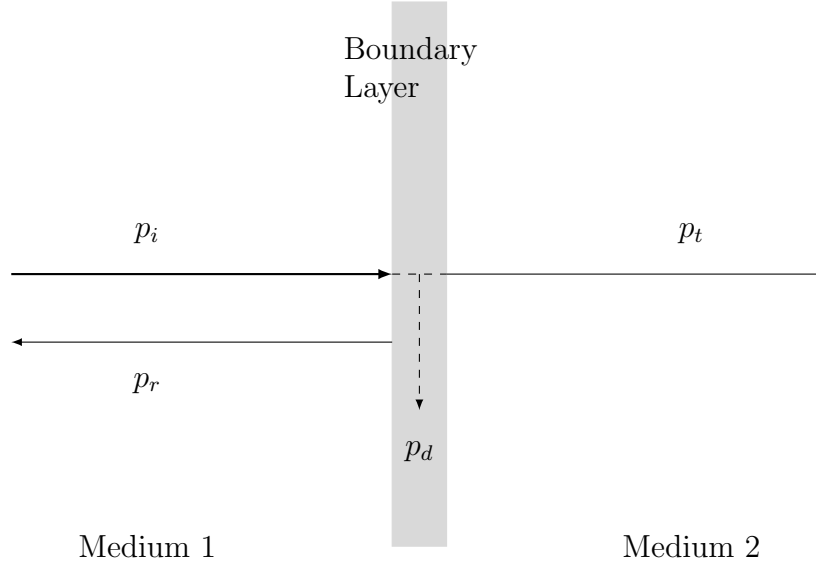
Figure 10: The reflection of a sound wave on a boundary surface.

acoustic field in terms of sound pressure balance. While partly the wave is reflected, another part is *dissipated*, which means a loss in transformation to heat. The rest is transmitted in to the second medium. It therefore applies that the sum of transmission and dissipation is equal to the sum of incoming and reflecting wave, as written in Equation (55),

$$p_i - p_r = p_d + p_t. \tag{55}$$

The ratio of reflection to incoming sound pressure is named *reflection factor* and is written in Equation (56). In case of a plane perpendicular wave it is equal to the ratio of differences between the two impedances of the medium,

$$R = \frac{p_r}{p_i} = \frac{Z_1 - Z_2}{Z_1 + Z_2}. \tag{56}$$

Depending on the medium this ratio can be complex or real, given by the fact that there can be phase difference between pressure and particle velocity. Finally, the sum of transmission and dissipation is named absorption. Equation (57) describes the absorption coefficient which is essentially the opposite of the reflection factor,

$$\alpha = 1 - |R|^2. \tag{57}$$

Besides the influence on pressure amplitude, the propagation through medium boundaries affects the propagation direction aswell. Similar to optics, refraction occurs. That means, *Snells law* can be applied, that provides a relation between the angle of incidence and angle of refraction. Figure 11 illustrates the changed direction of the wave
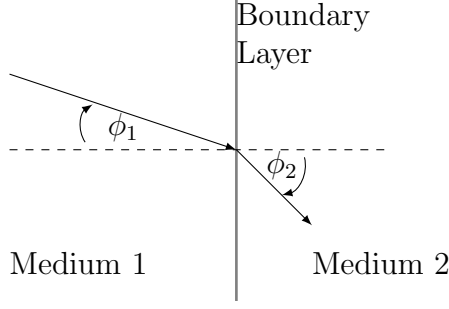
Figure 11: Snells law applied on a boundary layer between two mediums.

passed through the boundary layer. While the incoming wave in the first medium has angle ϕ_1 to the boundary surface normal, the passing wave in the second medium has angle ϕ_2. Snells law provides the correlation of both angles in Equation (58) with sound speed c_1 in the first medium and c_2 in the second. When considering a continuous change of the sound speed, the wave path has a continuous changing angle, resulting in bent paths,

$$\frac{\sin(\phi_1)}{c_1} = \frac{\sin(\phi_2)}{c_2}. \tag{58}$$

2.6 Propagation in Porous Media

Due to the more complex and inhomogeneous structure of porous mediums, sound propagates in form of compression waves through arbitrary channels filled with gas or fluids. According to Möser [27], waves can travel dispersive or non-dispersive depending on their frequency. In any case, the sound wave is subject to an attenuation that depends on the nature and thickness of the material. Physically, this effect is described by the *porosity* which is mathematically speaking the ratio of fluid or gas volume in the channels and the total volume of the medium. In combination with a empiric structure factor to account for dead ended channels, the correlation of particle velocity inside and outside of the medium is written in Equation (59),

$$v_{\text{outside}} = \frac{\text{porosity}}{\text{structure factor}} \cdot v_{\text{inside}} = \frac{\Omega}{\kappa} v_{\text{inside}}. \tag{59}$$

An observable relation between normal (outside) particle velocity motivates the definition of the *flow resistivity* σ and flow resistance σ_{r}. While the flow resistance is the measurable ratio of pressure before and behind the porous material, the flow resistivity is the flow resistance per unit length l,

$$\sigma = \frac{\sigma_r}{l}. \tag{60}$$

Note that for the sake of simplicity, the given Equations only illustrate the physical meaning of the parameters. From this presentation of porous mediums, the propagation of sound is described by augmented wave equations dealing with the more complex

22

correlations, including the resistance to air flow. Important in this context, is the concept of *complex wave numbers* given in the following Equation,

$$k_c = k\sqrt{\kappa}\sqrt{1 - j\frac{\sigma\Omega}{\omega\rho\kappa}}. \tag{61}$$

These wave numbers include the flow resistance and the effect on sound propagation. In literature often a *acoustic propagation constant* is used. Propagation constants are written as in Equation (62) and are related to complex wave numbers as denoted. The real part α corresponds denote the attenuation coefficient of the amplitude, while the imaginary β denotes the phase coefficient. The resulting pressure distribution is shown in Equation (63),

$$k_b = \alpha + j\beta = jk_c, \tag{62}$$

$$p(x) = \hat{p}e^{-k_b x} = \hat{p}e^{-\alpha x}e^{-j\beta x}. \tag{63}$$

2.7 Radiator Models

To generalize common occurring effects in sound radiation, elemental idealized models are used. Analogously to electrical engineering, an ascending order of radiator is constructed each representing a certain real world use case. Subsequently more complex and sophisticated models of certain real world sound phenomena can be constructed by combining these *elemental radiators*. The construction is successively combining predecessors. As a consequence the naming scheme refers to the construction step. Each nth step doubles the use of the first model, thus it is described as a multi pole of $2^N order$. The following section is based on Reference [37] and summarises the construction using the first two important models.

2.7.1 Zero-Order Radiator - Monopole

The *zero-order* radiator names a spherical sound source with an uniform finite pulsating radius, often illustrated as a breathing ball. In addition, the *monopole* radiator denotes a zero-order radiator with infinitesimal radius. In general the produced sound field follows the rules of spherical spreading with a directional factor of $\Gamma = 1$, which describes a point symmetrical acoustic field. Sound pressure propagates as in Equation (53) and is inversely proportional to the distance of the source,

$$\underline{v} = \frac{1}{\rho_0 c_0} \frac{\underline{A}}{r} (1 + \frac{1}{jkr}) e^{-jkr}. \tag{64}$$

The particle velocity in Equation (64) consists of two parts, the left hand side of the inner bracket term represents the far field decrease and the right hand term the near field decrease. As a result $(1 + \frac{1}{jkr})$ determines a decrease with proportional factor $\frac{1}{r^2}$ in the near field, while the far field has a much lower decrease with $\frac{1}{r}$. In summary the acoustic field can conveniently be distinguished into near field with $He << 1$ and far

field with $He >> 1$. The transition between these parts is continuous.

In the near field the phase shift of pressure and particle velocity results in a complex acoustic impedance, consisting of reactance Z_r^{Rea} and resistance Z_r^{Res}. For a finite radius $r = R$, the particle velocity on the surface of the radiator is denoted with v_R. In addition the boundary condition $\underline{v}_0 = \underline{v}_R$ takes effect and the acoustic radiation impedance is represented as the sum of reactance and resistance. While the reactance contains the amount of reactive power considerable in the near field, the resistance is accountable for the sound power emitted into the far field. It describes the strength of the radiator and can be simplified for the condition $1 \ll He \gg 1$. To simplify matter $S = 4\pi R^2$ denotes the enveloping surface of the radiator,

$$\underline{v}_{near} \approx \frac{1}{\rho_0 c_0} \frac{\underline{A}}{r} e^{-jkr} \tag{65}$$

$$\underline{Z}_r = Z_r^{Rea} + Z_r^{Res} = \rho_0 c_0 \frac{(kR)^2}{1 + (kR)^2} + j\rho_0 c_0 \frac{kR}{1 + (kR)^2} \tag{66}$$

$$P = \tilde{q}^2 \frac{\rho_0 c_0}{4\pi R^2} = \tilde{v}_n^2 S \rho_0 c_0 \quad \text{for He} >> 1 \tag{67}$$

$$P = \tilde{q}^2 \frac{\rho_0 c_0 k^2}{4\pi} \quad \text{for He} << 1 \tag{68}$$

In case of the far field, velocity can be denoted as in Equation (69) and because of the wave approaching plane spreading with increasing distance, the acoustic impedance approaches the characteristic impedance. In this way the sound intensity can be simplified to Equation (70),

$$\underline{v}_{far} \approx \frac{1}{\rho_0 c_0} \frac{\underline{A}}{r} e^{-jkr}, \tag{69}$$

$$\underline{I}_{far} = \tilde{p}\tilde{v} = \frac{\tilde{p}^2}{Z_0} = \tilde{v}^2 Z_0. \tag{70}$$

For the monopole with an infinitesimal radius the condition $He \to 0$ takes effect. Thus, previous conclusions for the far field are adopted and the sound power gets independent of the radiators' shape. The sound flow for He approaching zero solved for A delivers more compact Equations (72) - (73) for pressure and velocity. It is worth to note that sound flow and sound power depend on the frequency for $He \ll 1$,

$$\lim_{He \to 0} \underline{q} = \frac{4\pi}{jk\rho_0 c_0} \underline{A}, \tag{71}$$

$$\underline{p} = j\frac{k}{4\pi} \rho_0 c_0 \underline{q} \frac{e^{-jkr}}{r}, \tag{72}$$

$$\underline{v} = j\frac{k}{4\pi} \underline{q}(1 + \frac{1}{jkr})\frac{e^{-jkr}}{r}. \tag{73}$$

3 Noise Propagation Model

The general idea of this model is the analytical estimation of the sound pressure level at a given receiver position, based on provided sound power levels of multiple sources. It is important to note that the following methods are only applicable for the given scenario of a simple wind farm, composed of multiple wind turbines of the same type on a straight homogeneous ground. Furthermore, every simulation only provides the sound pressure level for a specified (human) receiver, which is at a naturally lower height compared to the wind turbines. Beyond, more complicated scenarios than those dealt with in the following chapters, are excluded. For example, sound absorbing barricades such as mountains are explicitly neglected but vegetation like trees that influence the sound propagation, are not.

The general approach is the calculation of the sound pressure in every one-third octave band of the broadband noise signal, as defined in Section 2.1.2. Since the amount of wind turbines in a wind farm is considered a homogeneous quantity and the sound signals from different turbines can be regarded as incoherent, the calculations are carried out for each individual wind turbine and the resulting levels are added up incoherently. The overall sound pressure estimation for a single turbine is depicted in Equation (74),

$$L_{\mathrm{R}} = L_{\mathrm{S}} - \left(A_{\mathrm{div}} + A_{\mathrm{atm}} + A_{\mathrm{gr}} + A_{\mathrm{sc}}\right). \tag{74}$$

L_{R} describes the continuous sound pressure level for a frequency band with center frequency f at the receiver position. L_{S} describes the sound power level of a source for the given center frequency f. The various A-terms represent all attenuation effects which are taken into account. These effects include geometrical spreading A_{div}, air absorption A_{atm}, influence from the ground A_{gr} and scattering zones A_{sc}. While the sound power level is an input provided by measurements or relating sound prediction models, the attenuation terms are calculated as described in the following sections. The procedure to determine any attenuation term is either to calculate the ratio of unaffected sound pressure to affected sound pressure at the receiver, or directly semi-empiric loss coefficients. Due to the logarithmic nature of the level measure, the terms can be arithmetical added or subtracted in total.

To begin with, Section 3.1 describes necessary coordinate and parameter transformations, when dividing the problem into scenes consisting of a single source and receiver. Afterwards, Section 3.2 focuses on how the individual turbines are modelled. After that, the calculation of geometrical spreading in Section 3.3 is described. In Section 3.4 the calculation of air absorption is defined, followed by Section 3.6 for the ground effect and Section 3.7 for scattering zones. Furthermore, in Section 3.5 the influence of meteorological conditions is introduced. Note that the meteorological influence is not directly taken into account with a single attenuation term but with the general influence on sound rays, which are employed in other terms. As a consequence, the last Sections from Section 3.8 to Section 3.11 deal with the calculation of necessary parameters, required for the previous analysis regarding the attenuation terms.
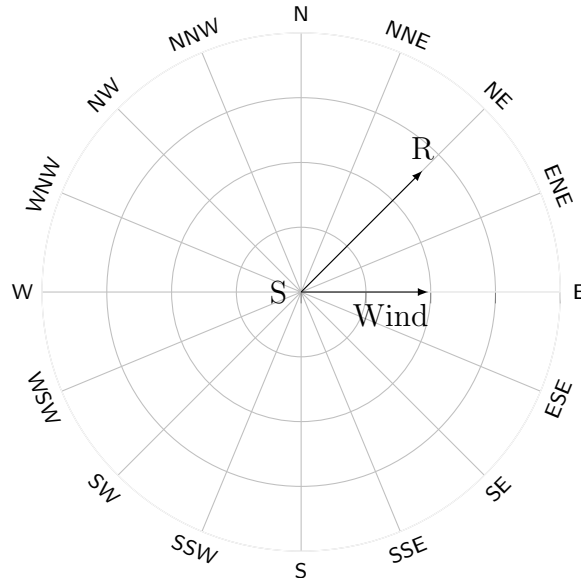
Figure 12: Wind speed denoted as a polar vector pointing in eastern direction with a certain magnitude in m/s. The vector from source to receiver can be considered as a directional vector since the magnitude is of no consequence. In the particular case drawn, the model will assume a light downwind.

3.1 Coordinate and Parameter Transformations

The section above implies the *divide and conquer* principle in the general approach of the simulation. This is due to the fact that the simulation only operates on pairs consisting of a single turbine and a single receiver position. In order to create these pairs some input parameter transformations and coordinate transformations have to be performed. First, the reduction from three spacial dimension to two is necessary. This step is straightforward done, by calculating the horizontal distance between the individual entities of one pair and reducing the horizontal space to this distance. The second necessary transformation concerns wind speed. While the model requires a vertical wind gradient for a single two dimensional scene, the wind speed is provided as depicted in Figure 12. In this particular example, the wind flows in eastern direction, which means depending on the scene, that a downwind, crosswind or upwind situation exists and that the wind speed must be calculated from the given wind vector. Therefore, as illustrated in Figure 12, a vector from source to receiver is determined. With this, the angle between the vectors is used to determine the wind speed component for further calculations. This means, that crosswind situations are assumed to have no wind speed at all.

3.2 Source and Receiver Model

In this section the modelling of the source and receiver is described briefly. As illustrated in Figure 13 the source is denoted with S at height h_S. The receiver is denoted
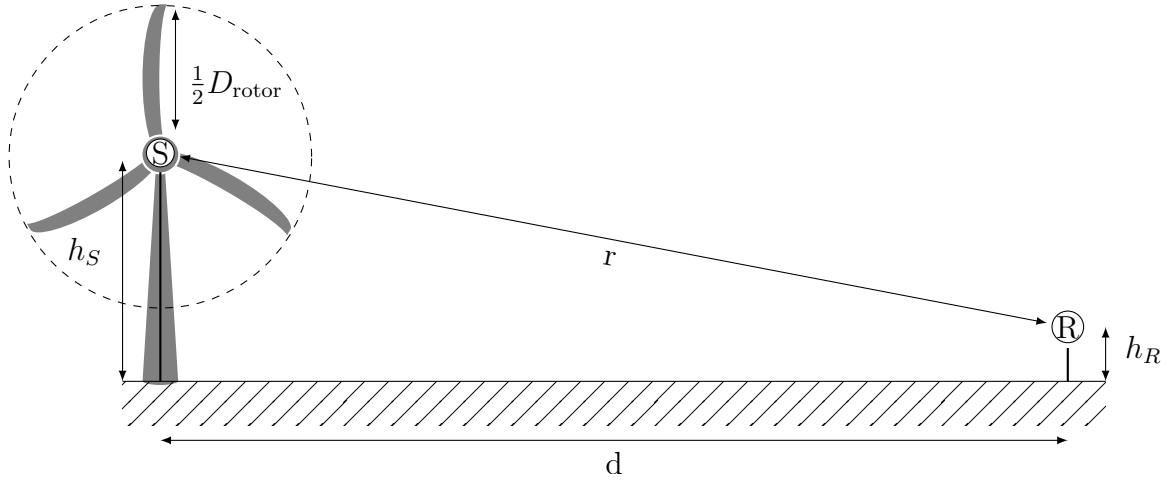
Figure 13: General model of receiver and wind turbine as a point source.

with R and located at height h_R. For the rest of this thesis, the horizontal distance is denoted with d and the euclidean distance with r. As discussed in Section 2.7, the turbine can be idealized as a point source, if the distance r is adequate. That means aswell, the receiver must be located in the far field of the source. Speaking of wind turbines, the part responsible for the sound can be reduced to the parameter rotor diameter D_{rotor} as its size. Since in principle only distances of more than several hundred meters from the sound source are of interest and the average diameter of the wind turbine is below 100 meters, the turbine is replaced by a point source at hub height. For this purpose, the following preconditions have to be met:

$$D_{\text{rotor}} \ll r \tag{75}$$

$$He \gg 1. \tag{76}$$

According to Reference [13] this condition is met when the receiver distance is more than 1.5 times the rotor diameter. Furthermore, the term L_{S} is either obtained by measurements, or a corresponding prediction model and is assumed to include the directional characteristic of the wind turbine in the given direction to the receiver. According to related studies and to allow for better comparison, the use of the widely employed sound power measurement standard *IEC 61400-11* [11] is assumed.

3.3 Geometrical Spreading

In this section the calculation of the attenuation term A_{div} is described. Based on the assumption of a point source, the term A_{div} accounts for basic geometrical loss of energy by the spherical spreading of the acoustic field. As described in 2.4.2, all loss effects are neglected at this point and a homogeneous spherical acoustic field is assumed. This means Equation (77) can be used as a function of radius to calculate the far field intensity I. The imaginary area A corresponds to the omnidirectional radiation

Symbol	Description	Unit
Input		
r	The euclidean distance between source and receiver.	m
Output		
A_{div}	The attenuation term for geometrical spreading loss.	dB

Table 1: Input and output for the calculation of geometrical spreading.
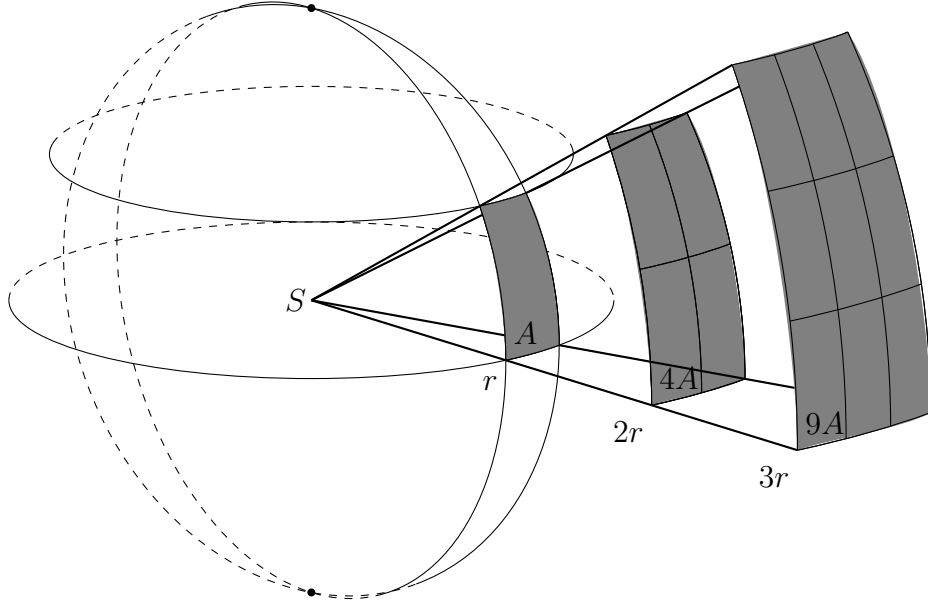
Figure 14: The inverse square law with imaginary area A covering the acoustic field. Parameter I denotes the sound intensity and P the sound power.

of the source and is the envelope of the acoustic field. The decrease of sound intensity I is known as the *inverse square law* as depicted in Figure 14.

$$I(r) = \frac{P}{A} = \frac{P}{4\pi r^2} \tag{77}$$

As previously introduced, sound pressure is proportional to the square root of the sound intensity, thus resulting in a proportional decrease of sound pressure at distance r. Since the effects of the atmosphere are neglected, reference impedance for air is used with $Z_0 = 400\,\mathrm{kg \cdot m^{-2} \cdot s^{-1}}$. Consequently, intensity level and sound pressure level have equal values. As a result, the calculation of the intensity depending on the distance r from the receiver delivers a formula for the sound pressure level at the same distance,

$$L_w - 10 \cdot \log(4\pi r^2) \approx L_w - 20 \cdot \log(r) + 11. \tag{78}$$

Notably, in literature corrections are often made if the source is only partly radiating of the spherical angle, which is usually the case if sources are directly placed near

reflecting surfaces. In case of wind turbines, a correction would make sense for reflecting ground conditions. However, this effect is considered in other attenuation terms and thus neglected at this point. In total, the term A_{div} as in Equation (79) is frequency independent and denotes the loss due to ideal geometrical spreading.

$$A_{\text{div}} \approx 20 \cdot \log(r) + 11 \tag{79}$$

3.4 Air Absorption

Symbol	Description	Unit or domain
	Input	
r	The euclidean distance between source and receiver.	m
T_a	The ambient atmospheric temperature.	K
p_a	The ambient atmospheric pressure.	kPa
H	Concentration of water vapour in the atmosphere.	%
H_r	(Optional) Relative humidity, can be provided as a replacement for H.	$0 \leq H_r \leq 1$
	Output	
A_{atm}	The attenuation term for air absorption.	dB

Table 2: Input and output for the calculation of air absorption.

In this section the calculation of A_{atm} is described. The input parameters are given in Table 2. Due to molecular processes, the sound propagation in air is noticeably dampened. In essence, molecular friction and relaxation are responsible for this effect. Friction describes the loss of energy when oscillating molecules collide. Relaxation describes the energy consumption needed for the excitation of molecules to the state of oscillation. The primary molecules involved in relaxation are oxygen (O_2) and nitrogen (N_2). Depending on temperature and humidity, this effect increases with increasing frequency. Low air humidity and temperature have a reinforcing effect. The *air absorption coefficient* α_{atm} is defined as an empiric loss coefficient corresponding to the center frequency of a single one third band. The coefficient is given in decibel per meter and is set in proportion to the distance r in meters to the source in Equation (80),

$$A_{\text{atm}} = \alpha_{\text{atm}} \cdot r. \tag{80}$$

The absorption coefficient is calculated as indicated in Reference [15], where all appearing constants were determined in a laboratory environment. The resulting equation consists of three terms, α_{cl} summarizes *classical absorption* due to rotation and friction, the two remaining, α_O and α_N, determine the relaxation effect of the main responsible molecules. Prerequisite for the calculation of the vibrational relaxation are the corresponding relaxation frequencies in Equations (82) and (81). For common denomination, each symbol referring to oxygen is marked with a subscript O and for nitrogen with a subscript N. Inputs for the calculation are ambient atmospheric

pressure p_a, ambient atmospheric temperature T_a and molar concentration of water vapour H. In addition, reference temperature $T_N = 293.15\,\text{K}$ and reference pressure $p_N = 101.325\,\text{kPa}$ are employed,

$$f_N = \frac{p_a}{p_N} \left(\frac{T_a}{T_N}\right)^{\frac{-1}{2}} \left(9 + 280 \cdot H \cdot \exp\left\{-4.170\left[\left(\frac{T_a}{T_N}\right)^{\frac{-1}{3}} - 1\right]\right\}\right), \qquad (81)$$

$$f_O = \frac{p_a}{p_N} \left(24 + 4.04 \cdot 10^4 \cdot H \cdot \frac{0.02 + H}{0.391 + H}\right). \qquad (82)$$

Overall, the absorption coefficient for a specific pure tone frequency f is calculated as in Equation (83),

$$\alpha_{\text{atm}} = 8.686 f^2 \left(\alpha_{cl} + \left(\frac{T_a}{T_N}\right)^{\frac{-5}{2}} (\alpha_O + \alpha_N)\right), \qquad (83)$$

$$\alpha_{cl} = 1.84 \cdot 10^{-11} \left(\frac{p_a}{p_N}\right)^{-1} \left(\frac{T_a}{T_N}\right)^{\frac{1}{2}}, \qquad (84)$$

$$\alpha_O = 0.01275 \left(\exp\left\{\frac{-2239.1}{T_a}\right\}(f_O + \frac{f^2}{f_O})^{-1}\right), \qquad (85)$$

$$\alpha_N = 0.1068 \left(\exp\left\{\frac{-3352.0}{T_a}\right\}(f_N + \frac{f^2}{f_N})^{-1}\right). \qquad (86)$$

If the molar concentration of water vapour is not available it is calculated as shown in Equation (87). Therefore, the *relative humidity H_r* and *saturation vapour pressure p_{sat}* are used. The relative humidity is, at a given temperature, the ratio in per cent of partial water vapour pressure in air and the saturation vapour pressure regarding a plane surface of liquid water at the same temperature. The saturation pressure term determines the point of thermodynamic equilibrium between water vapour and the condensed water at the surface. Equation (88) is used to calculate p_{sat}. The term T_{tp} denotes the triple-point isotherm temperature of water, approximated with $273.16\,\text{K}$. That is the point in which water coexists in its liquid, gas or solid phase,

$$H = H_r \left(\frac{p_{\text{sat}}}{p_N}\right)\left(\frac{p_N}{p_a}\right), \qquad (87)$$

$$p_{\text{sat}} = p_N \cdot 10^C, \qquad (88)$$

$$C = -6.8346 \left[\left(\frac{T_{tp}}{T_a}\right)^{1.261}\right] + 4.6151. \qquad (89)$$

While the above formulas have an acceptable accuracy for pure tones, the application onto frequency bands is not without an additional source of errors. As described by Joppa et al. [18], bandpass-filtered data is dominated by lower frequencies and thus the prior introduced methods for pure tones will overpredict the attenuation for a band

center frequency. Depending on the resolution of the band-pass filter and the frequency dependence of the attenuation, the error rises in unacceptable ranges. Therefore a correction on the pure tone coefficient is applied, given by Equation 90 [30],

$$A_{\text{atm}} = A_{\text{atm}} \cdot (1.0054255 - 0.00122622 \cdot A_{\text{atm}})^{1.6} \tag{90}$$

3.5 Meteorological Conditions

For subsequent attenuation terms, geometrical sound rays are employed. These rays are heavily influenced by the meteorological conditions of the atmosphere. Therefore, the following section introduces the concept of how sound rays are modified by atmospheric conditions.

From a macroscopic perspective, the medium where sound propagates is the at-

Increasing wind speed

Shadow
zone
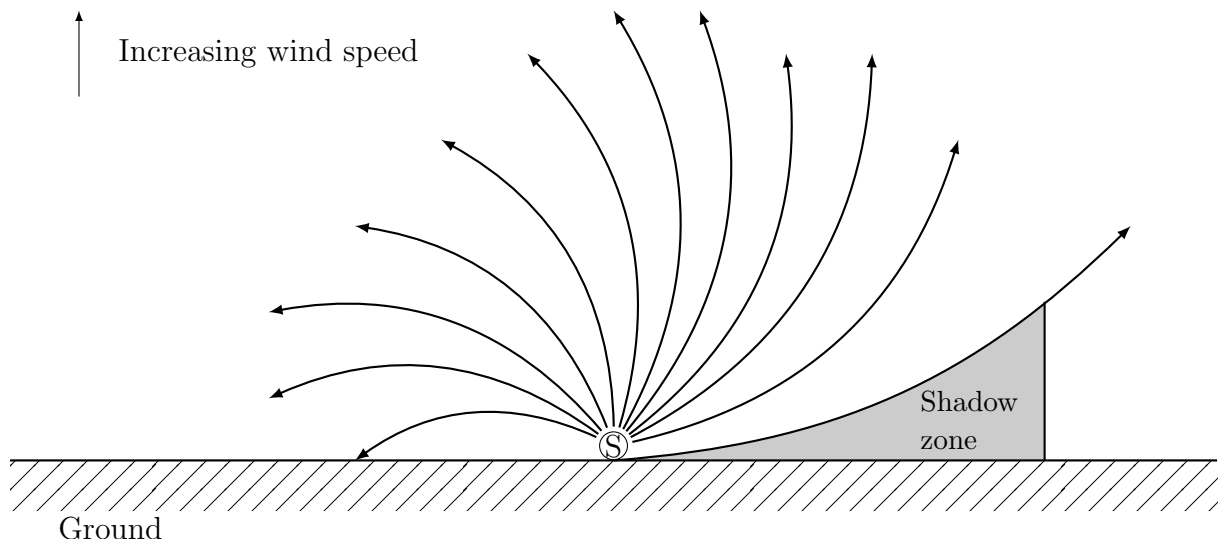
Ground

Figure 15: Refraction relative to the ground, caused by normal wind shear.

Decreasing temperature

Increasing temperature

Shadow
zone

Ground
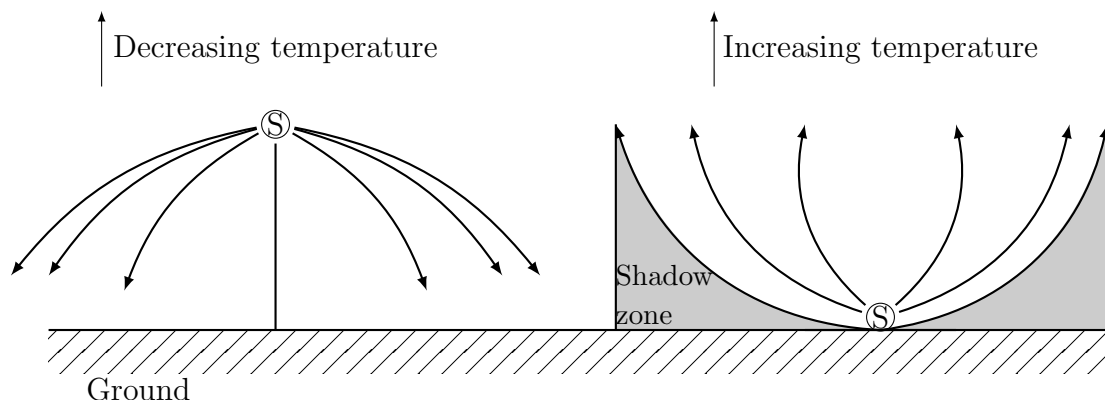
Figure 16: Refraction due to the temperature gradient.

mosphere and not just air. The most important aspects of atmospheric influences

considered in this model are temperature and wind gradient. With growing altitude the wind speed increases. This effect is described by the vertical wind speed gradient, typically referred to as *wind shear*. The same applies for the temperature, which depending on the meteorological situation, decreases or increases with growing altitude. This effect is described by the *vertical temperature gradient*. This simple description of the complicated inhomogeneous situation of the atmosphere is obviously already limited in its dimensions to the vertical direction. Horizontal changes are neglected, which has proven to be sufficient in this context and in other models. Overall, both gradients can be described by a *sound speed profile*, as both can be narrowed to their effect on the sonic gradient. Special about the temperature change is the potential presence of an *inversion layer*. Instead of decreasing with altitude, the temperature increases with altitude in this specific layer. The general effect of both gradients is refraction of the sound wave, i.e. the direction of sound waves is changed. When modelling sound waves as rays, Figure 15 and Figure 16 show how they are refracted towards, or away from the ground. A temperature inversion causes refraction towards the ground, a strong normal temperature gradient causes upward refraction. In addition, a strong downwind directed wind shear causes refraction towards the ground and upwind directed away from the ground. The wind shear usually prevails the temperature effect and only weak wind speed gradients can surpass upward refraction in downwind conditions.

3.6 Ground Attenuation

It appears that a wind turbine is not able to radiate energy uniformly in all directions because it is usually limited by the ground. Therefore, this section introduces the effects of the ground and defines the calculation of A_{gr}

In various models the ground is considered as a simple reflective barrier, which leads to a hemispherical spreading of the source. However, this way it is not possible to account for interaction of ground reflected waves and primary wave. For that reason, the ground effect is modelled with sound rays. The general idea is illustrated in Figure 17 with an additional ray, that is reflected of the ground. The first part of this additional ray, from source to ground, is denoted with r_S and is called the *incident ray*. The second part is denoted with r_R and is referred to as the *reflected ray*. The point of incidence on the ground is denoted with P and is equally called the point of reflection. On the one hand, the *angle of incidence* is denoted with ϕ and is measured between the ground surface normal and incident ray. On the other hand, ϕ is also the *angle of reflection* and measured between the surface normal and reflected ray. The whole concept is based on the *law of reflection* from optics, which states that the angle of incidence is equal to the angle of reflection. For that reason, both angles are denoted as ϕ. This law implies the possibility to consider a vertical imaginary substitute source I, with the illustrated sound ray instead of the real ray. In any way, the reflected ray contributes to the sound pressure at the receiver with the prerequisite of an horizontal approximately straight homogeneous ground. Essentially, the degree of contribution depends on how strong air and ground differ as propagation mediums for sound. Consequently, the modelling of the ground and the characteristics of the sound ray determine the following analysis.
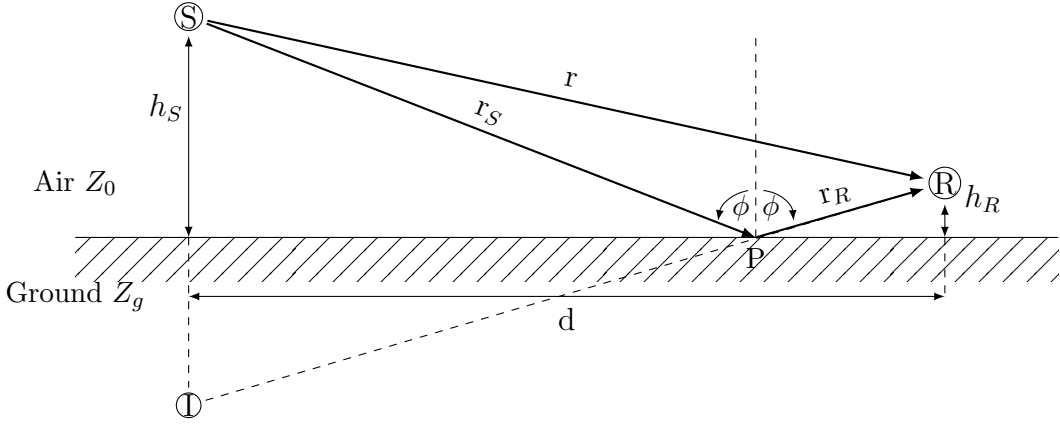
Figure 17: Modelling the hemispherical spreading with acoustic rays. The ground adds a reflected ray which contributes to the total pressure amplitude at the receiver. The degree of the contribution depends on the ground properties and the relation between direct and reflected ray.

In Section 3.9 the calculation of the characteristic impedance of the ground Z_g is defined, that is the single parameter summarizing the ground properties. The subsequent Section 3.10 introduces the *reflection coefficient* based on the impedance model to determine how much sound the ground absorbs or reflects. The analysis of the reflection coefficient starts with simple plane waves, resulting in the *planar reflection coefficient* R_p. Afterwards, the simple planar coefficient is extended for the complex behaviour of spherical wave fronts, concluding to the *spherical reflection coefficient* Q. This leads to the following Section 3.6.1 and Section 3.6.2, where the pressure contribution of the reflected ray is calculated. This calculation is divided into two sections for different meteorological scenarios but both result in the determination of the ground attenuation term A_{gr} for the given situation. The general approach of both Sections is to calculate the ratio of sound pressure with reflection to sound pressure without reflection. To obtain this ratio, it has to be distinguished between two situations. Based on the simple situation illustrated by Figure 17, the first scenario considers the description, where a reflected and direct ray reach the receiver. The second situation occurs, when a receiver is inside a meteorological shadow zone, as defined in Section 3.5. Here, no simple reflected ray exists but instead a diffraction coefficient is employed. The condition whether the receiver is located in such a zone is provided by the following Equation,

$$d > 0.95\sqrt{h_S(\frac{2}{|\xi_n|} - h_S)} + \sqrt{h_R(\frac{2}{|\xi_n|} - h_R)}. \tag{91}$$

In case the equation is fulfilled, the horizontal distance d between receiver and source is large enough for the receiver to be located inside the shadow zone.

3.6.1 Ground Attenuation outside of a Shadow Zone

Symbol	Description	Unit or Domain
	Input	
d	The horizontal distance between source and receiver.	m
h_S	The height above the ground of the source.	m
h_R	The height above the ground of the receiver.	m
$c(h)$	The linear sound speed profile.	m/s
Q	The spherical reflection coefficient.	-
F_i	The coherence coefficient of the ith ray.	$0 \leq F_i \leq 1$
	Output	
A_{gr}	The attenuation term for ground effects.	dB

Table 3: Input and output for the calculation of the ground attenuation outside the shadow zone.

In order to determine A_{gr} with the receiver outside of the shadow zone, the travel distance of the sound rays is required. Since the decrease of sound pressure is proportional to travelled distance, the ratio of travel distances is equal to the ratio of sound pressure amplitudes.

For the calculation of ray lengths, the method in Section 3.8 is used. Therefore, the point of incidence between ray and ground is determined with the following Equation [30],

$$2d_G^3 - 3d \cdot d_G^2 + (\frac{h_S}{\xi_n}(2 + \xi_n h_S) + \frac{h_R}{\xi_n}(2 + \xi_n h_R) + d^2)d_G - \frac{h_S}{\xi_n}(2 + \xi_n h_S)d = 0. \quad (92)$$

When this Equation has multiple solutions, the solution with maximum distance d_G to the source is chosen. Depending on the degree of curvature, the height of the source, the height of the receiver and the horizontal distance between the two, the applied procedures have to account for the situations in Figure 18 and 19. The key difference between all situations is the resulting position of point P, which is described by the horizontal distance d_G. The calculation of the total travel distance of the reflected ray $r_{\text{ref}} = r_S + r_R$ is divided into two steps. First of all, the travel distance r_S from source to point of incidence is calculated. Afterwards, the travel distance from point of incidence to receiver r_R is added. For the calculation of r_S, point P is considered to be the receiver. For the calculation of r_R, the situation is flipped. Point P is considered the receiver, while the original receiver is considered the source. This flip of receiver and P ensures the precondition of a higher source holding true.

As described in Section 3.8.1, the contributing rays are combined coherently to obtain the resulting pressure amplitude. Therefore, let the primary direct ray be denoted as p_1 and the reflected ray as p_2. The corresponding travel distances are r_{ref} for the reflected ray and r_{dir} for the direct ray. The resulting pressure functions are denoted

(a) High curvature and small height difference result in the illustrated situation, with the point of incidence in the middle.

(b) Less curvature and small height difference result in the illustrated situation, with the point of incidence in the middle.

Figure 18: Point of incidence for the reflected ray with small height difference, different curvatures and downward refraction.

in Equations (93) - (94), with the spherical reflection coefficient Q (Section 3.10). The amplitude of both terms is replaced with the equal ratio of path distances,

$$p_1 = \frac{e^{j \cdot \omega \cdot \tau_{\text{dir}}}}{r_{\text{dir}}}, \tag{93}$$

$$p_2 = Q \frac{e^{j \cdot \omega \cdot \tau_{\text{ref}}}}{r_{\text{ref}}}. \tag{94}$$

With reference to Section 3.8.2, the ratio of amplitudes can be obtained with Equation (139), where p_{gr} is the coherent combination of reflected and primary ray,

$$A_{\text{gr}} = -10 \log \left(\frac{|p_{gr}|^2}{|p_1|^2} \right) = \left\{ |1 + F_2 \frac{p_2}{p_1}|^2 + (1 - F_2^2) \left| \frac{p_2}{p_1} \right|^2 \right\}. \tag{95}$$

3.6.2 Ground Attenuation inside a Shadow Zone

Symbol	Description	Unit
	Input	
d	The horizontal distance between source and receiver.	m
h_S	The height above the ground of the source.	m
h_R	The height above the ground of the receiver.	m
$c(h)$	The linear sound speed profile.	m/s
	Output	
A_{gr}	The attenuation term for ground effects.	dB

Table 4: Input and output for the calculation of the ground effect inside the shadow zone.
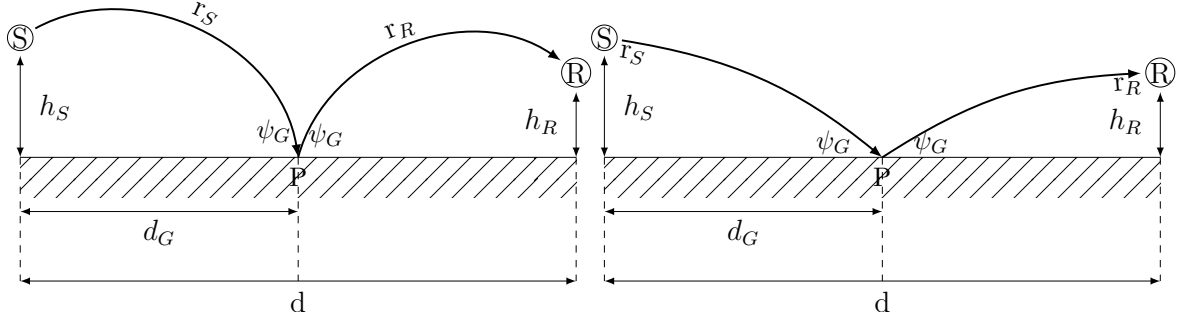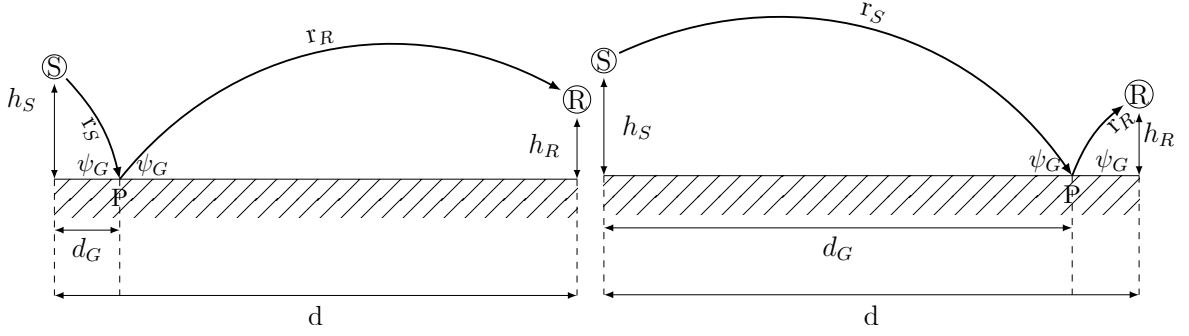
(a) High curvature and big height difference result in the illustrated situation, where the point of incidence is close to S.

(b) High curvature and big height difference result in the illustrated situation, where the point of incidence is close to the R.

Figure 19: Point of incidence for the reflected ray with big height differences, but two possible solutions for the reflection point P.

This Section focuses on the calculation of the term A_{gr}, if the receiver is located inside a shadow zone. In this region no ray is reaching the receiver directly, resulting in a strong reduction of the pressure amplitude. The condition whether the receiver is in a shadow zone or not is given in Equation (91). In this context, the ground attenuation is composed of two terms written in Equation (96). L_{gr} accounts for diffuse ground waves and L_{sz} accounts for the shielding effect of the shadow zone,

$$A_{\mathrm{gr}} = -(L_{\mathrm{gr}} + L_{\mathrm{sz}}). \tag{96}$$

The first term is based on Equation (94). Instead of using p_2, a composite imaginary ray p_2' is introduced. This ray is composed of the direct and reflected ray with a grazing angle $\psi_G = 0$ for the determination of the reflection coefficient Q (ground wave). The travel distance of this imaginary ray is denoted with r_{co} and is defined as the path distance of the direct ray. Since the primary ray acts as the reference for all phase angles, the ground effect is determined by the calculation of the reflection coefficient Q with previously mentioned parameters of r_{co},

$$L_{\mathrm{gr}} = 20 \log(|1 + Q|). \tag{97}$$

Figure 20 illustrates the process where the unified ray disregards the ground and reaches the receiver in the shadow zone. As a consequence, the more the receiver is in the shadow zone, the weaker is the resulting contribution of L_{gr}. The horizontal distance d_m is calculated as described in Section 3.8. The vertical distance h_m from the ground plane and the apex of the imaginary ray is used to define an absorbing shielding wall. Subsequently, the term L_{sz} is calculated by assuming diffraction over this wall in a neutral atmosphere with no curved rays. Equation (98) contains the overall formula for L_{sz}, with D_{sz} as the diffraction coefficient based on wedge shapes by Plovsing [29]. Instead of the amplitude ratio, the equivalent ratio of travel distance is employed,

$$L_{sz} = 20 \log \left(|D_{sz}| \frac{d}{r_S + r_R} \right). \tag{98}$$

36
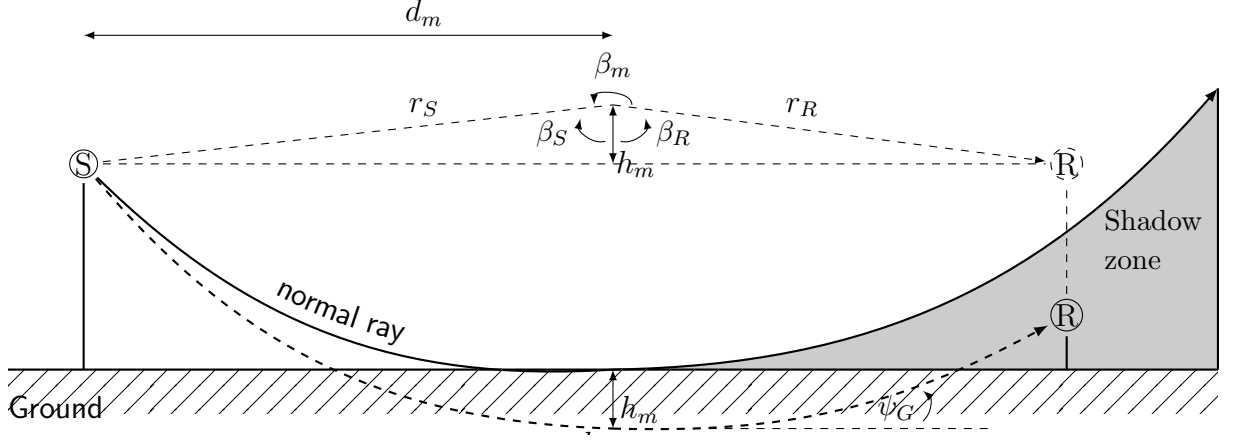
Figure 20: Due to strong upwards curving, the receiver is inside a shadow zone. Thus, the normal ray doesn't reach the receiver. Only diffracted sound and arbitrary reflections arrive. Therefore, an imaginary combined ray, composed of direct and reflected ray, is constructed. Based on this ray the shielding effect of the shadow zone L_{sz} is calculated.

The angles β_m, β_S and β_R are given by the following Equations,

$$\beta_m = 2\pi - (\beta_S + \beta_R), \tag{99}$$

$$\beta_S = \arcsin\left(\frac{d_m}{r_S}\right), \tag{100}$$

$$\beta_R = \arcsin\left(\frac{d - d_m}{r_R}\right). \tag{101}$$

The diffraction coefficient is given by:

$$D_{sz} = 2X_1 \cdot X_2, \tag{102}$$

$$X_1 = \frac{\pi}{\sqrt{2}} \frac{\sin(|X_2|)}{|X_2|} \frac{e^{j\pi/4}}{\sqrt{1 + \left(\frac{2\tau_S \cdot \tau_R}{\tau^2} + \frac{1}{2}\right)\frac{\cos^2(|X_2|)}{2}}} X_3, \tag{103}$$

$$X_2 = \frac{1}{4}(-3\pi + \beta_m) + \pi H(\pi - \beta_m), \tag{104}$$

$$X_3 = \mathrm{sgn}(X_4)(f(|X_4|)) - jg(|X_4|)), \tag{105}$$

$$X_4 = \sqrt{\frac{4\omega \cdot \tau_S \cdot \tau_R}{\pi(\tau_S + \tau_R)}} \frac{\cos(|X_2|)}{\sqrt{\frac{1}{4} + \left(\frac{2\tau_S \tau_R}{(\tau_S + \tau_R)^2} + \frac{1}{2}\right)\cos^2(|X_2|)}}. \tag{106}$$

The travel times of the ray parts r_S and r_R are denoted with τ_S and τ_R. The overall travel time of the ray traversing the constructed shield is denoted with $\tau = \tau_S + \tau_R$. Since the term L_{sz} neglects the effect of reflection, the spherical reflection coefficient is omitted. The term $sgn(x)$ represents the signum function and $H(x)$ is the *Heavisides'*

step function. The terms $f(x)$ and $g(x)$ are the auxiliary Fresnel functions and are calculated with the constants a_i in Table 5 as follows,

$$f(x) = \begin{cases} \frac{1}{\pi x} & \text{if } x \geq 5 \\ \sum_{n=0}^{12} a_n x^n & \text{if } 0 < x < 5 \end{cases}, \tag{107}$$

$$g(x) = \frac{1}{\pi^2} x^3. \tag{108}$$

a_0	a_1	a_2	a_3
0.49997531354311	0.00185249867385	-0.80731059547652	1.15348730691625
a_4	a_5	a_6	a_7
-0.89550049255859	0.44933436012454	-0.15130803310630	0.03357197760359
a_8	a_9	a_{10}	a_{11}
-0.00447236493671	0.00023357512010	0.00002262763737	-0.00000418231569
a_{12}			
0.00000019048125			

Table 5: Constants for a_i

3.7 Scattering Zones

Symbol	Description	Unit
	Input	
d	The horizontal distance between source and receiver.	m
h_S	The height above the ground of the source.	m
h_R	The height above the ground of the receiver.	m
$c(h)$	The linear sound speed profile.	m/s
$\overline{h}_{\text{obj}}$	The average height of the ith scattering zone and equally of the objects inside the zone.	m
n	Tree density provided as the number of trees per square meter.	m^{-2}
d_{trunk}	The average trunk diameter of objects in the zone.	m
l_{sc}	The length of the ith scattering zone.	m
d_{sc}	The distance between source and the start of the ith scattering zone.	m
	Output	
A_{sc}	The attenuation term for scattering zones.	dB

Table 6: Input and output for the calculation of scattering zones.

The term *scattering zone* refers to an area where sound rays are not entirely blocked, but strongly scattered. At wind farms, such areas are usually vegetation zones like
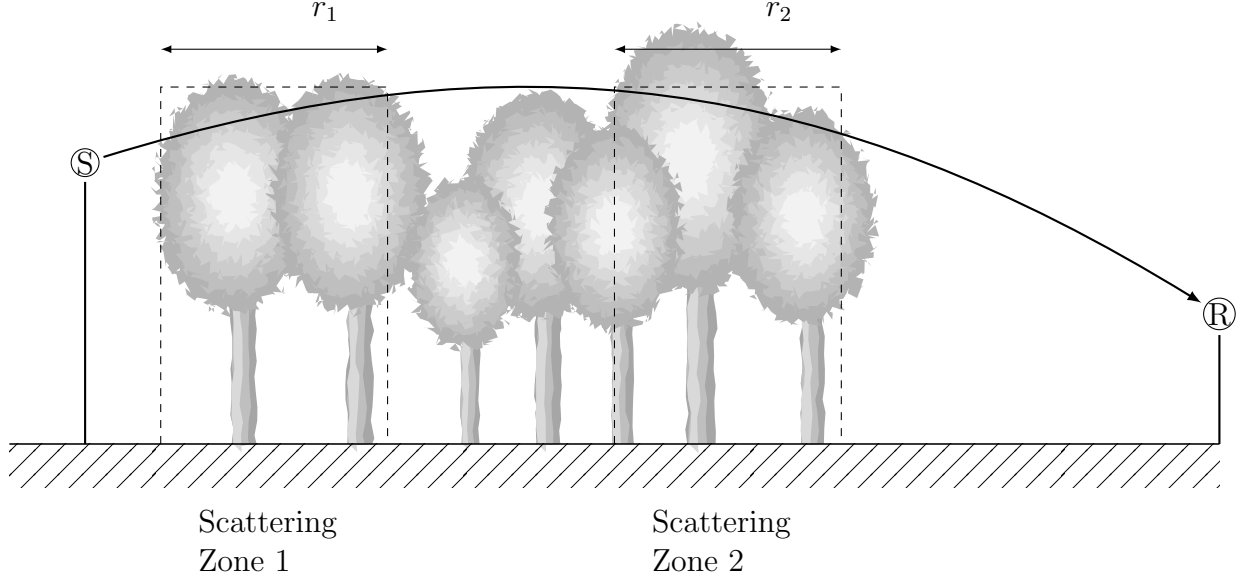
Figure 21: Ray affected by a scattering zone. Ray path lengths r_1 and r_2 represent the parts of the ray which are affected by intersection with the zone (e.g. foliage of trees).

forests. The effect of scattering zones regarding the pressure amplitude at the receiver is considered in this Section. The applied approach is taken from Hansen et al. [13] based on Plovsing [29].

The calculation is given in Equation (109) and is defined for forests, or similar objects. The corresponding ray path lengths are given in Figure 21. The ray path length r_{sc} describes the sum of affected path lengths, that are calculated, based on the height of the ray in Section 3.8. As seen in the Figure 21 both zones are composed of multiple objects. Due to this inhomogeneity, the height of the ray is calculated in discrete steps along the path, to determine whether a segment is affected or not. The empiric coefficient k_f represents a frequency weighting for the affected ray and values for the interpolation are written in Table 10. The correction term $\Delta L(h', \alpha_{sc}, r'))$ is determined with interpolation from values in Table 7. The coefficient α_{sc} represents the approximated absorption coefficient of the objects in the scattering zone. The parameter $\overline{h}_{\text{obj}}$ is the average height of object in the scattering zone. It is important to note, that the this attenuation effect is only calculated for the primary ray, which is usually the one with the highest pressure amplitude.

$$A_{sc} = -k_f \left(\frac{r_{sc} \cdot n \cdot d_{\text{trunk}}}{1.75} \right)^2 \cdot 1.25 \Delta L(h', \alpha_{sc}, r') + 20 \log(8r') \tag{109}$$

$$r' = n \cdot d_{\text{trunk}} \cdot r_{sc} \tag{110}$$

$$h' = n \cdot d_{\text{trunk}} \cdot \overline{h}_{\text{obj}} \tag{111}$$

r'	h' = 0.01			h' = 0.1			h' = 1		
	$\alpha_{sc} = 0$	$\alpha_{sc} = 0.2$	$\alpha_{sc} = 0.4$	$\alpha_{sc} = 0$	$\alpha_{sc} = 0.2$	$\alpha_{sc} = 0.4$	$\alpha_{sc} = 0$	$\alpha_{sc} = 0.2$	$\alpha_{sc} = 0.4$
0.0625	6.0	6.0	6.0	6.0	6.0	6.0	6.0	6.0	6.0
0.125	0	0	0	0	0	0	0	0	0
0.25	-7.5	-7.5	-7.5	-6.0	-7.0	-7.5	-6.0	-7.0	-7.5
0.5	-14.0	-14.25	-14.5	-12.5	-13.5	-14.5	-12.5	-13.0	-14.0
0.75	-18.0	-18.8	-19.5	-17.3	-18.0	-19.0	-16.0	16.8	-17.7
1.0	-21.5	-22.5	-23.5	-20.5	-21.6	-22.8	-19.3	-20.5	-26.3
1.5	-26.3	-27.5	-29.5	25.5	-27.2	-29.0	-24.0	-25.5	-26.3
2.0	-31.0	-32.5	-34.5	-30.0	-32.0	-33.3	-27.5	-29.5	-30.8
3.0	-40.0	-42.5	-45.5	-37.5	-40.5	-42.9	-34.2	-36.0	-37.8
4.0	-49.5	-52.5	-56.3	-45.5	-49.5	-52.5	-40.4	-42.8	-45.5
6.0	-67.0	-72.5	-78.0	-62.0	-67.0	-72.0	-52.5	-56.2	-60.0
10.0	-102.5	-113.0	-122.5	-94.7	-103.7	-112.5	-78.8	-84.0	-89.7

Table 7: Values used for the interpolation of $\Delta L(h', \alpha_{sc}, r')$ [13]

3.8 Sound Rays

Symbol	Description	Unit
	Input	
d	The horizontal distance between source and receiver.	m
h_S	The height above the ground of the source.	m
h_R	The height above the ground of the receiver.	m
$c(h)$	The linear sound speed profile.	m/s
ξ_n	The normalized sound speed gradient.	-
d_X	The horizontal distance to point X on the ray, from which the height of X should be calculated.	m
	Output	
τ_{ray}	The travel time of the concerned ray.	s
r_{ray}	The travel distance of the concerned ray.	m
h_{X}	The height of a given segment on the ray.	m

Table 8: Input and output for the calculation of ray parameters.

Since numerical simulation of wave propagation is avoided, effects based on waves have to be simulated otherwise. For this reason, methods from geometrical acoustics are used. The core concept of these methods is the *sound ray* that approximates the propagation of sound waves as a geometrical ray from the place of origin to reception. This representation is already a considerable approximation but it is still accurate as shown in numerous ray tracing algorithms. Consequently, in the following sections the necessary tools for determining the parameters of sound rays are described.
Besides the spatial arrangement of source and receiver, the sound speed gradient c(h) with the coefficient ξ_n is the key influence on the path length. The following equations are introduced for curved rays in a downward refracting atmosphere with $\xi_n > 0$. Afterwards, the same equations are modified for an upward refracting atmosphere with $\xi_n < 0$. For a neutral atmosphere $\xi_n = 0$, a value close to zero is chosen $\xi_n = 10^{-10}$, to keep consistency of the equations [29].

The general idea is based on Hidaka et al. [14], who outlines the fact that linear sound speed profiles produce rays shaped like circular arcs. That implies basic trigonometric identities can be used for the length calculation. In principle, the length of the arc is determined by applying *Pythagoras's theorem*. With infinitesimal small tangents along the arc, the path is approximated as the sum of these tangents. This concept is illustrated in Figure 22 with the infinitesimal length of the tangent ds as the hypotenuse of the underlying triangle. Thus, ds is given by Equation (112),

$$\mathrm{d}s = \sqrt{\mathrm{d}x^2 + \mathrm{d}h^2}. \tag{112}$$

By using the inclination angle ψ_G, the length of the arc can be obtained by integration
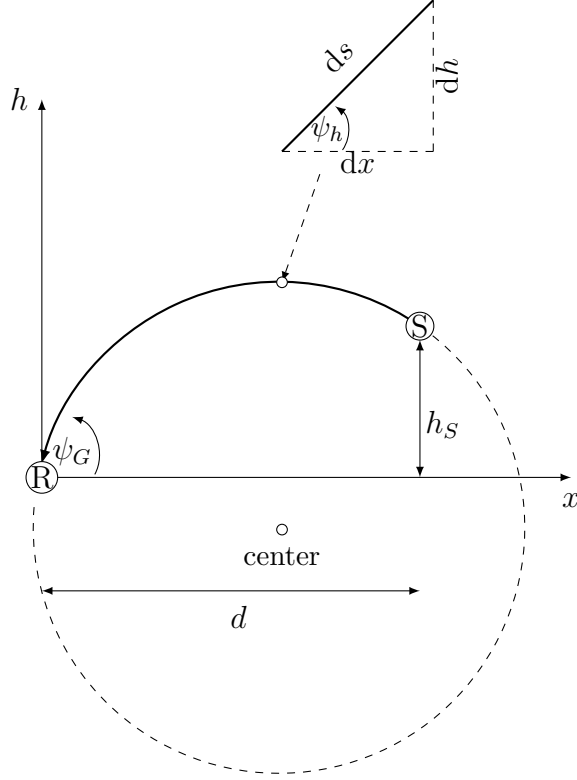
Figure 22: A sound ray originating at source S, with height h_S and horizontal distance d from receiver R. The receiver is located at the origin of the coordinate system. The ray is approximated with infinite small segments ds along the path. The segments are the hypotenuse of the underlying triangle.

over the height h as follows,

$$s(h) = \int_0^h \frac{ds}{\sin(\psi_h)}. \tag{113}$$

Note that the length of the arc is calculated starting from receiver to source, which fits the given example, but the same idea applies to any given situation. With respect to Snell's law, described in Section 2.5, the angle ψ_h changes continuously with the height as follows,

$$\frac{\cos(\psi_h)}{c(h)} = \frac{\cos(\psi_G)}{c_G}. \tag{114}$$

Particularly, the starting angle is ψ_G at height $h = 0$ followed by angle ψ_h at height $h > 0$, which is determined with the linear sound speed profile and in respect to the above law. Consequently, we get the following for ψ_h,

$$\psi_h = \arccos\left(\frac{\cos(\psi_G) \cdot c(h)}{c_G}\right) = \arccos\left[\cos(\psi_G) \cdot (1 + \xi_n h)\right]. \tag{115}$$

After integration with respect to h, the path length is obtained by assuming the receiver

at the origin of the coordinate system and any source at height $h = h_S$,

$$s(h) = \frac{1}{\xi_n \cos \psi_G} \left[\arcsin \left((1 + \xi_n h) \cos \psi_G \right) - \frac{\pi}{2} + \psi_G \right].$$ (116)

The travel time is obtained by including the time $\mathrm{d}t$, necessary to pass over the segment $\mathrm{d}s$,

$$\mathrm{d}t = \frac{\mathrm{d}s}{c(h)}.$$ (117)

By integration with respect to h, the travel time is obtained as follows,

$$t(h) = \int_0^h \mathrm{d}\tau = \frac{1}{2\xi_n \cdot c_G} \ln \left(\frac{D_h(0)}{D_h(h)} \right),$$ (118)

$$D_h(x) = \frac{1 + \sqrt{1 - (1 + \xi_n x)^2 \cos^2 \psi_G}}{1 - \sqrt{1 - (1 + \xi_n x)^2 \cos^2 \psi_G}}.$$ (119)

It is important to note, that the equations above are defined for the single parameter height, which leads to some ambiguity, depicted in Figure 23. Depending on the geometry of source, receiver and degree of curvature, the apex of the arc can be located between source and receiver. This fact, leads to multiple points on the arc with equal height, as illustrated with the height h_S relating to two points. To deal with this problem, the horizontal distance to the apex d_m is employed. As shown by Hidaka
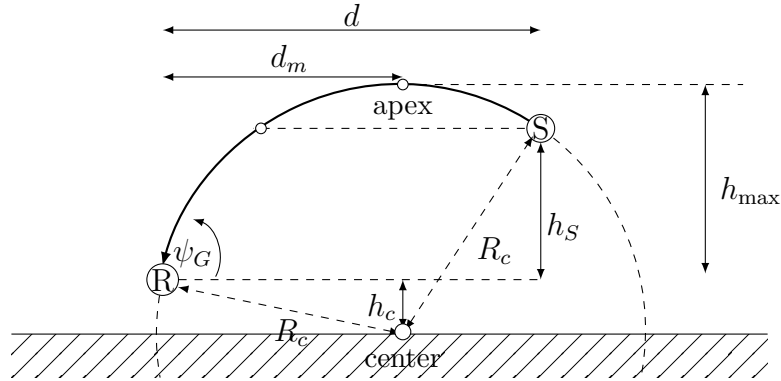
Figure 23: The apex of the curvature is between source and receiver. Thereby, two points on the arc have the same height, which has to be considered when defining the arc length as a function of height.

et al. [14], by integration of the horizontal component with respect to h, the following circular equation is obtained,

$$\left(x - \frac{\tan(\psi_G)}{\xi_n} \right)^2 + \left(h + \frac{1}{\xi_n} \right)^2 = \left(\frac{1}{\xi_n \cos(\psi_G)} \right)^2.$$ (120)

This equation determines the underlying circle with the radius R_c, horizontal distance d_m and height h_c,

$$R_c = \frac{1}{|\xi_n| \cos(\psi_G)},$$ (121)

$$d_m = \frac{\tan(\psi_G)}{\xi_n}, \tag{122}$$

$$h_c = -\frac{1}{\xi_n}. \tag{123}$$

If $d_m > d$ the above equations can be used since the apex is behind or equal to the source. If $d \leq d_m$, the complete ray path of the circular segment above the ground is determined as the double of the path length to the apex. Afterwards the excess path from source to ground is subtracted, resulting in the intended path length from receiver to source via the apex of the arc,

$$r_{\mathrm{ray}} = \begin{cases} s(h_S) & \text{if } d_m \geq d \\ 2 \cdot s(h_{\max}) - s(h_S) & \text{if } d_m < d. \end{cases} \tag{124}$$

The corresponding travel time be written as follows,

$$\tau_{\mathrm{ray}} = \begin{cases} t(h_S) & \text{if } d_m \geq d \\ 2 \cdot t(h_{\max}) - t(h_S) & \text{if } d_m < d. \end{cases} \tag{125}$$

Up until now, the path length and travel time for a ray are only determined for rays from source to receiver at coordinate origin. For the application of Snell's law with respect to the sound speed profile, the method is limited to the ground plane. However, for the model arbitrary situations should be allowed. In order to apply the preceding analysis, with source and receiver above the ground, the linear sound speed profile is modified to start at receiver height. This allows the receiver to be assumed in the origin of the coordinate system as previously. The sound speed profile is modified with
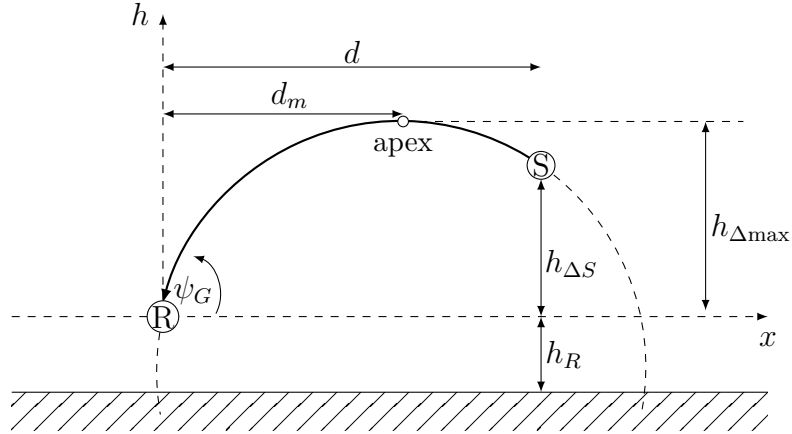
Figure 24: To account for a receiver at height h_R, the coordinate system origin is located at the receiver and the sound speed profile is shifted for h_R.

the sound speed c_R at height h_R as follows,

$$c(h) = c_R(1 + \xi_n(h - h_R)), \tag{126}$$

$$\xi_n = \frac{\Delta c}{\Delta h} \frac{1}{c_R}, \tag{127}$$

$$c_R = c_G(1 + \xi_n h_R) \tag{128}$$

Lastly, for the calculation in case of an upward refracting atmosphere ($\xi_n < 0$), on the one hand the coordinate system is simply shifted, on the other hand $\xi_n = -\xi_n$, which results in the situation above. Figure 25 illustrates the process. Note that the height of the receiver is $h_{\Delta R} = h_S - h_R$. While in the figure, receiver and source are drawn as they appear, for the application of the prior described procedures, the positions are swapped. Finally, for some applications the reverse problem has to be considered. In
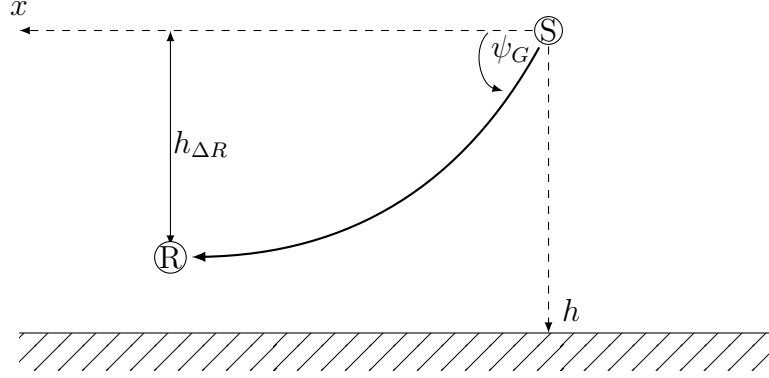
Figure 25: For upwards curved rays the coordinate system is shifted and the prior method is applied, with the illustrated parameters. Note that for application of above equations the receiver is swapped with the source.

some cases it is necessary to determine the height of a point on the ray if only the horizontal distance is known. The determination of this height for a given point X, is done in relation to the center of the circular ray. As shown by Figure 26, the distance d_m to the center and the radius R_c constitute a rectangular triangle with angle ϑ. From Equation (122) and Equation (121), the necessary width d_s of the adjacent leg can be determined. If $d_m = d_X$ the desired height of X is equal to the apex height, thus $h_X = h_{\max}$. In any other case, d_s is determined with Equation (129),

$$d_s = |d_m - d_X|. \tag{129}$$

Thereby, the angle ϑ is obtained as follows,

$$\vartheta = \arccos\left(\frac{d_s}{R_c}\right) \tag{130}$$

This results in Equation (131) for the desired height h_X,

$$h_X = R_c \cdot \sin(\vartheta) + h_c \tag{131}$$
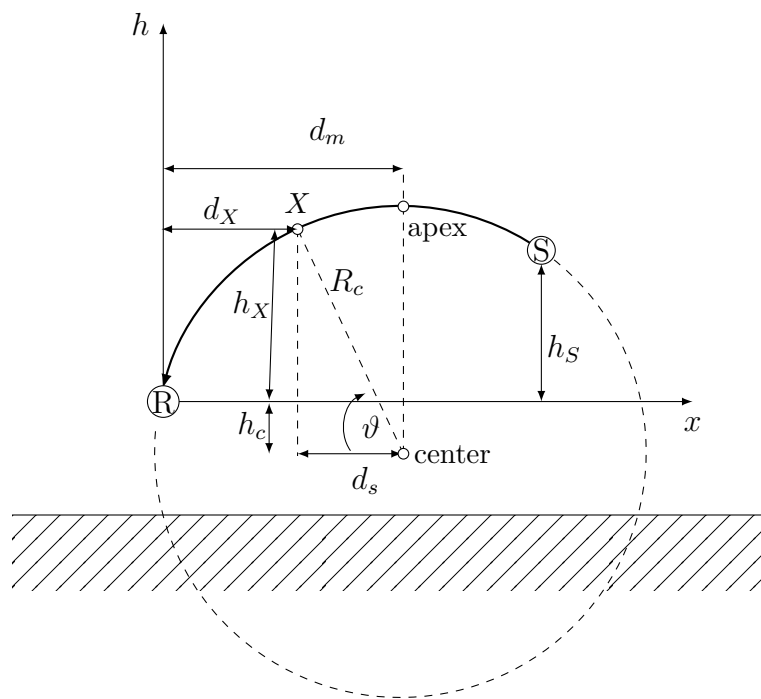
Figure 26: The determination of the height for a certain point on the ray path is done, relative to the center.

3.8.1 Representation and Combination of Sound Rays

Sound rays represent sound waves which propagate along the ray path. To account for changed propagation times and travel distances caused by attenuation effects, it is necessary to perform a *coherent combination* of multiple sound rays. On the contrary to incoherent addition of sound pressure amplitudes, which is assumed in this model where no ray theory is applied, the phase relation of different sound waves is included. Therefore, an appropriate representation of the sound wave is necessary. Every one third band of the sound spectrum is treated as a pure tone function, which enables a simple representation with relative phase terms.

For illustration of the process, let sound ray 1 be defined by Equation (132) and sound ray 2 by Equation (133). As pointed out by L'Espérance et al. [23] the representation of the phase term is only done with consideration of the time dependence. This choice is based on the variation of the wave number k with height, which is included in the calculation of the travel time but not in the location specific phase term with constant k. Additionally it is important to note that a positive time dependence is assumed with $e^{+j\omega t}$ as opposed to Section 2.4. This convention is compatible with other methods and uncritical with prior introduced conventions, since only the dimensionless relative phase between rays is investigated,

$$p_1 = \hat{p}_1 \cdot e^{j\omega t} = \hat{p}_1 \cdot e^{j\varphi_1}, \tag{132}$$

$$p_2 = \hat{p}_2 \cdot e^{j\omega t} = \hat{p}_2 \cdot e^{j\varphi_2}. \tag{133}$$

The coherent combination of sound rays is mathematical expressed as vector addition. As introduced in Section 2.4, the real part of the exponential terms represents the oscillatory function. The result of the coherent combination of ray 1 and ray 2 in Equation (134), depends on the phase angle φ_i,

$$p_{\text{res}} = \left| \hat{p}_1 e^{j\varphi_1} + \hat{p}_2 e^{j\varphi_2} \right| \tag{134}$$

The term phase angle is relative and denotes the shift between two vectors. In this context, the model should account for coherence between primary ray and rest. Therefore, every phase term φ_i is relative to the primary ray. To simplify subsequent calculations, the angle of the primary ray is set to zero. Since all pressure amplitudes $\hat{p}_i$ are positive and positive time dependence is assumed, every phase angle can be obtained as in Equation (135),

$$\varphi_i = \arctan\left(\frac{\text{Im}\{p_i\}}{\text{Re}\{p_i\}}\right). \tag{135}$$

This means the phase angle of p_{res} can be calculated as follows,

$$\varphi_{\text{res}} = \arctan\left(\frac{\text{Im}\{p_1\} + \text{Im}\{p_2\}}{\text{Re}\{p_1\} + \text{Re}\{p_2\}}\right) = \arctan\left(\frac{\hat{p}_1 \sin(\varphi_1) + \hat{p}_2 \sin(\varphi_2)}{\hat{p}_1 \cos(\varphi_1) + \hat{p}_2 \cos(\varphi_2)}\right). \tag{136}$$

The application of the law of cosine on the complex plane of the vector addition parallelogram of p_1, p_2 and p_{res} yields to Equation (137) The ratio of two sound rays can be calculated directly, as shown in Equation (138),

$$\hat{p}_{\text{res}}^2 = \hat{p}_1^2 + \hat{p}_2^2 + 2\hat{p}_1\hat{p}_2 \cos(|\varphi_1 - \varphi_2|), \tag{137}$$

$$\frac{p_1}{p_2} = \frac{\hat{p}_1}{\hat{p}_2} \frac{e^{j\varphi_1}}{e^{j\varphi_2}} = \frac{\hat{p}_1}{\hat{p}_2} e^{j(\varphi_1 - \varphi_2)}. \tag{138}$$

3.8.2 Partial Coherence

Symbol	Description	Unit
	Input	
$\Delta\tau$	The difference between ray travel times of primary ray and ith ray.	ms
$\overline{T}$	The average temperature along the ray path.	K
d	The horizontal distance between source and receiver.	m
h_R	The height above the ground of the source.	m
h_S	The height above the ground of the receiver.	m
C_v	Strength of atmospheric turbulence due to wind.	$\mathrm{m^{4/3} \cdot s^{-2}}$
C_t	Strength of atmospheric turbulence due to temperature.	$\mathrm{K \cdot s^{-2}}$
	Output	
F_i	The overall coherence coefficient for the ith ray.	$0 \le F_i \le 1$
F_f	The coherence coefficient for bandwidth errors.	$0 \le F_f \le 1$
$F_{\Delta\tau}$	The coherence coefficient for travel time variations.	$0 \le F_{\Delta\tau} \le 1$
F_t	The coherence coefficient for atmospheric turbulences.	$0 \le F_t \le 1$
F_r	The coherence coefficient for surface roughness.	$0 \le F_r \le 1$
F_s	The coherence coefficient for scattering zones.	$0 \le F_s \le 1$

Table 9: Input and output for the calculation of coherence coefficients.

The assumption of a representative harmonic function for a spectrum is an idealization, which neglects complex temporary phase relations of the corresponding spectral wave. To account for this inaccuracy and for environmental influences which reduce the coherence effect, an empiric coefficient is employed. With the help of this coefficient a *partial coherent* combination of rays is implemented. Particularly, the combination of rays is depicted in Equation (139), which consists of the weighted coherent part and incoherent part. Note that for the level calculation performed later, the pressure squares are used,

$$|p_{res}|^2 = |1 + \sum_{i=2}^{N} F_i \cdot p_i|^2 + \sum_{i=2}^{N}(1 - F_i^2)|p_i|^2. \tag{139}$$

The partial coherence coefficients F_i provided by Plovsing [29], are implemented to account for atmospheric turbulence, frequency band error, atmospheric refraction, surfaces and scattering due to obstacles including vegetation. That means aswell, only the coherence between a primary ray and the rest is regarded, as coherence between multiple reflection or other weak contributions can be neglected [13]. This approach has shown enough accuracy and reduces computational complexity.
The partial coherence coefficient F_i in Equation (140) is calculated as the product of

48

multiple coefficients corresponding to a single attenuation effect. The index of the coefficient denotes the partial coherence between primary ray and the consecutively numbered secondary ray i,

$$F_i = F_f F_{\Delta\tau} F_t F_r F_s. \tag{140}$$

The first factor F_f is responsible for the error relating to the spectrum bandwidth for center frequency f. It is given by Equation (141), with $\Delta\tau$ representing the difference of wave travel time between primary ray and the concerned secondary ray,

$$F_f = \begin{cases} 1 & \text{if } X_1 = 0 \\ \frac{\sin(X_1)}{X_1} & \text{if } 0 < X_1 < \pi \\ 0 & \text{if } X_1 \geq \pi, \end{cases} \tag{141}$$

$$X_1 = 0.23\pi \cdot f \cdot \Delta\tau. \tag{142}$$

The factor $F_{\Delta\tau}$ is responsible for a time variation in the refraction effect. Due to atmospheric fluctuations, the effect of refraction is not as steady as described in Section 3.5. Thus, the error in this idealization is taken into account with Equation (143), where $\Delta\tau_+ = |\tau_{1+} - \tau_{2+}|$ denotes the difference between the upper limits of expected travel time variations, due to atmospheric fluctuations of the primary ray τ_{1+} and concerned ray τ_{2+},

$$F_{\Delta\tau} = \begin{cases} 1 & \text{if } X_2 = 0 \\ \frac{\sin(X_2)}{X_2} & \text{if } 0 < X_2 < \pi \\ 0 & \text{if } X_2 \geq \pi, \end{cases} \tag{143}$$

$$X_2 = 2\pi \cdot f \cdot |\Delta\tau_+ - \Delta\tau|. \tag{144}$$

The upper limits of the variation are calculated with the upper limit of the employed sound speed profile. With reference to Equation (207), the fluctuations of coefficients A and B have to be considered. By assuming a Gaussian distribution the fluctuation terms A_+ and B_+ are calculated as in Equation (145) and Equation (146), with s_A and s_B as the standard deviations of the related term. The upper limit of the travel time terms is calculated the same way as the normal travel time, but with the adapted sound speed profile,

$$A_+ = A + 1.7s_A, \tag{145}$$

$$B_+ = B + 1.7s_B. \tag{146}$$

The factor F_t refers to atmospheric turbulence and is given by Equations (147) to (150). Note that the calculation is modified from the original reference by Hansen et al. [13]. In this context $\overline{T}$ is the average temperature over the secondary ray path in Kelvin, $\overline{c}_T$ is the average sound speed corresponding to the average temperature, d is the horizontal distance between source and receiver, d_q is the half mean square separation of the direct and reflected ray paths between source and receiver, C_t is the

$\frac{k \cdot d_t}{2}$	0	0.7	1	1.5	3	5	10	20
k_f	0	0	0.05	0.2	0.7	0.82	0.95	1

Table 10: Values for factor k_f

strength of turbulence due to temperature and C_v is the strength of turbulence due to wind. Values of the turbulence strength parameters are obtained from measurements,

$$F_t = \begin{cases} e^{X_3}, & \text{if } X_3 \geq -1 \\ (2 + X_3)e^{-1} & \text{if } -2 < X_3 < -1 \\ 0 & \text{if } X_3 \leq -2, \end{cases} \quad (147)$$

$$X_3 = -0.1365\gamma_T \cdot (\frac{f}{\bar{c}_T} \cdot d_q^{5/3} \cdot d), \quad (148)$$

$$\gamma_T = \frac{C_T^2}{T} + \frac{22C_v^2}{3\bar{c}_T^2}, \quad (149)$$

$$d_q = \frac{h_S \cdot h_R}{h_S + h_R}. \quad (150)$$

The factor F_r in Equations (151) to (153), describes the effect of surface roughness, which not only impacts the wind gradient, but the sound propagation in general. The main parameter of this coefficient is the root mean square σ_r of height variations at the ground in metres. The angle ϕ is defined in Figure 17,

$$F_r = \begin{cases} e^{\frac{1}{2}g(X)}, & \text{if } -2 \leq g(X) < 0 \\ (2 + \frac{1}{2}g(X))e^{-1} & \text{if } -4 < g(X) < -2 \\ 0 & \text{if } g(X) \leq -4, \end{cases} \quad (151)$$

$$g(X) = \begin{cases} 0 & \text{if } X \leq 0.026686 \\ 0.55988(0.115448 - X) - 0.049696 & \text{if } 0.026686 < X < 0.115448 \\ -0.066 + 1.066X - 8.543X^2 + 4.71X^3 - 0.83X^4 & \text{if } X \geq 0.115448, \end{cases}$$
$$(152)$$

$$X = k \cdot \sigma_r \cdot \sin\left(\frac{\pi}{2} - \phi\right). \quad (153)$$

The factor F_s is related to effects of scattering zones. As suggested by Plovsing [29] the parameter is only used for forests (or similar vegetation zones), where direct sound rays are blocked and only diffracted and reflected sound reaches the receiver. Therefore a statistical approach is applied, in case of the presence of a scattering zone as described in Section 3.7. The parameter n denotes the number of trees (or similar objects) per square metre in the corresponding area, d_t is the mean tree trunk diameter, k_f is the composite coefficient of trunk diameter and wave number k. The length of impact on the ray path is denoted with r_{sc}. Values for k_f are linearly interpolated or extrapolated with Table 10. The expression $r_f \cdot n \cdot d_t$ is limited by 1.75, if it exceeds this value, it is set to 1.75

$$F_s = 1 - k_f(\frac{r_{sc} \cdot n \cdot d_t}{1.75})^2 \quad (154)$$

50

3.9 Ground Properties

Symbol	Description	Unit
	Input	
f	The center frequency of the concerned one third band.	Hz
σ	The measured flow resistivity for the underlying ground material.	kg·m^{-3}·s^{-1}
l	(Optional) Surface layer thickness.	m
	Output	
Z_g	Complex characteristic impedance of the ground.	kg·m^{-2}·s^{-1}

Table 11: Input and output for the calculation of the specific ground Impedance.

In this Section the calculation of necessary ground properties is described. That includes the *complex characteristic impedance Z_g*, the *complex wave number* and the *normalized complex density* of the ground.

The approximation of the characteristic impedance Z_g is developed from the one parameter Model of Delany and Bazley [9]. Thus it relies only on flow resistivity σ of the ground. The flow resisitivity describes the opposition of the medium to the propagation of the sound wave, in terms of applied pressure and resulting particle velocity. It is a composite of the porosity and viscosity of the material. As seen on the acoustic propagation constant k_g and Z_g written in Equation (155) and Equation (156), the dominant parameter for the frequency dependence of the impedance, is the flow resistivity in combination with the ambient density,

$$Z_g = \rho_0 c \sqrt{1 + i(\frac{\sigma}{2\pi f \rho_0})}, \tag{155}$$

$$k_g = \frac{2\pi f}{c} \sqrt{1 + i(\frac{\sigma}{2\pi f \rho_0})}. \tag{156}$$

According to Delany and Bazley [9], most characteristic impedance values can be further approximated, by simply assuming a standard value for $\rho_0 = \rho_N = 1.205 \, \text{kg/m}^3$, to reduce the formula to the single dominant input parameter. This parameter is denoted with σ_f and written in Equation (161), as the ratio of frequency and flow resistivity. However, the authors conclude, that the single parameter model produces physical unrealistic values for higher frequencies and values of the frequency/flow resistivity ratio below 0.01 or above 1.0. Thereby, several newer empiric models provide improved expressions, that are based on the idea of Delany and Bazley [9], but overcome these limitations. Consequently, the empiric model given by Hansen et al. [13], with the *normalised complex density ρ_g* and the *normalised complex compressibility κ_g* as given below is used if the flow resisitivity exceeds $500 \, \text{kPa·s·m}^{-2}$,

$$Z_g = \rho_0 c_0 \sqrt{(\rho_g \kappa_g)}, \tag{157}$$

$$k_g = \frac{2\pi f}{c_0} \sqrt{\frac{\rho_g}{\kappa_g}}, \tag{158}$$

$$\rho_g = \frac{1}{1+X}, \tag{159}$$

$$\kappa_g = \frac{1}{1 - 0.4 \cdot Y}. \tag{160}$$

The terms X and Y are summarized below, with the input parameter multiplied with the atmospheric density,

$$\sigma_f = \rho_0 \cdot \frac{f}{\sigma}, \tag{161}$$

$$X = \frac{X_3(X_1 - X_3)X_2^2 - X_4^2 X_1^2}{X_3^2 X_2^2 + X_4^2 X_1^2} + j \frac{X_1^2 X_2 X_4}{X_3^2 X_2^2 + X_4^2 X_1^2}, \tag{162}$$

$$\begin{aligned} X_1 &= 1 + 9.66\sigma_f, & X_2 &= \sigma_f(1 + 0.0966\sigma_f), \\ X_3 &= 2.537 + 9.66\sigma_f, & X_4 &= 0.159(1 + 0.7024\sigma_f), \end{aligned} \tag{163}$$

$$Y = 0.592 \left\{ \frac{Y_3(Y_1 - Y_3)Y_2^2 - Y_4^2 Y_1^2}{Y_3^2 Y_2^2 + Y_4^2 Y_1^2} \right\} + j \frac{Y_1^2 Y_2 Y_4}{Y_3^2 Y_2^2 + Y_4^2 Y_1^2}, \tag{164}$$

$$\begin{aligned} Y_1 &= 1 + 8.26896\sigma_f, & Y_2 &= 0.856\sigma_f(1 + 0.0826896\sigma_f), \\ Y_3 &= 2.537 + 8.26896\sigma_f, & Y_4 &= 0.159(1 + 0.6012544\sigma_f). \end{aligned} \tag{165}$$

3.10 Reflection Coefficients

Symbol	Description	Unit
Input		
Z_g	Complex characteristic impedance of the ground.	$\text{kg·m}^{-2}\text{·s}^{-1}$
k_g	Complex wave number for the ground.	-
f	Frequency of the concerning wave.	Hz
σ	Flow resisitivity of the ground.	kPa·s·m^{-2}
ϕ	The incidence angle of the reflection.	rad
r_S	Path length of the ray from source to point of incidence.	m
r_R	Path length of the ray from source to point of incidence.	m
Output		
R_p	The reflection coefficient for plane waves.	-
Q	The reflection coefficient for spherical waves.	-

Table 12: Input and output for the calculation of the reflection coefficients.

The general process of reflection of plane waves, as depicted in Section 2.5 serves as a basis. Equation (166) illustrates how sound waves are described when propagating diagonally in a (x, y) plane with incidence angle ϕ as in Figure 17,

$$p(x,y) = \hat{p} \cdot e^{jk(\cos(\phi)x + \sin(\phi)y)}. \tag{166}$$

Principles introduced in Section 2.5 serve as a starting point for this 2 dimensional case. This would imply another sound beam pointing into the ground with an refraction angle depending on the ratio of the impedances and a complex mechanism of dissipation and propagation through porous media. However, only the reflected sound ray is of interest for the model. Depending on the surface layer characterization, the speed of sound at the surface layer is much less compared to the speed of sound in air, what ensures that the transmission wave travels perpendicular into the ground, with no refraction angle. Moreover in this situation the ground impedance is independent of the incidence angle of the sound wave, which derives the term *local reaction*. Instead of being dependent on the angle of incidence and thus of the pressure distribution at this region, the reaction on the ground surface only depends on the point of incidence. These assumptions are known as *locally reacting* boundary conditions at the ground surface and regarding to Chessell [7] are adequate for predicting sound propagation over some grounds. According to Hansen et al. [13] the precondition for this assumption is fulfilled with Equation (167),

$$\frac{\rho_0 f}{\sigma} < 10^{-3}. \tag{167}$$

The opposite is the assumption of an *extensively reacting* boundary condition, where the reaction at the ground is affected by the displacements at other locations and the transmission wave has to be considered. To summarize, depending on the rule in Equation (167), different set of formulas for the reflection coefficient are applied and described in the following section. Regardless of this assumption, the effects of the spherical wave are included in addition to the reflected planar wave. In the literature, two additional waves are referred to for this purpose. One is a ground wave, which is caused by diffusion of the source, and the other is a surface wave, which propagates only near the ground. The surface wave amplitude decreases exponentially, is less influenced by refraction and other atmospheric conditions, but is of little importance for downwind propagation. It also occurs mainly at low frequencies and is one of the reasons why sound is less attenuated at low frequencies.

3.10.1 Planar Reflection Coefficient

The above equation for diagonal waves and the situation illustrated in Figure 17 results in a plane wave reflection factor for waves, as in Equation (168). With the cosine of angle of refraction β as defined in Equation (169),

$$R_p = \frac{Z_g \cos(\phi) - Z_0 \cos(\beta)}{Z_g \cos(\phi) + Z_0 \cos(\beta)}, \tag{168}$$

$$\cos(\beta) = \sqrt{1 - (\frac{k}{k_g})^2 \sin^2(\phi)}. \tag{169}$$

The angle β is by convention the angle between surface normal into the ground and the transmission wave propagating inside the ground. Note, that in the following section j is used for the imaginary unit to avoid confusion with indices. The characteristic

impedance of air is calculated with ρ_0 in kg/m^3 and c_0 in m/s, both at ground level. The resulting reflection coefficient can be understood as as in Equation (170), where φ_R is the phase angle between reflected and incident ray and the amplitude represents the rate of amplitude attenuation,

$$R_p = |R_p|e^{j\varphi_R}. \tag{170}$$

Assumption of a locally reacting surface implies $k_g \gg k$. As a consequence, the term $\cos(\beta)$ tends to zero and the reflection coefficient for plane waves reduces to Equation (171),

$$R_p = \frac{Z_g \cos\phi - Z_0}{Z_g \cos\phi + Z_0} \tag{171}$$

3.10.2 Spherical Reflection Coefficient

The spherical reflection coefficient is written in Equation (172) with φ_Q as the phase angle between reflected and incident ray. The calculation procedure of Q is taken from Hansen et al. [13] and from Plovsing [29],

$$Q = R_p + (1 - R_p)\left[YG(w)\right]^{n_G} = |Q|e^{j\varphi_Q}. \tag{172}$$

The term n_G was added for more precise solution for grazing incidences and its value is given by Equation (173),

$$n_G = 1 - 0.7e^{-16(h_S + h_R)/\lambda}. \tag{173}$$

The term $G(w)$ in Equation (174), is called the *boundary loss factor* and its argument w the *numerical distance*,

$$G(w) = 1 - j\sqrt{\pi}wg(w), \tag{174}$$

$$g(w) = e^{-w^2}\text{erfc}(-jw). \tag{175}$$

The term Y as defined in Equation (176), can be simplified depending on the boundary condition for the surface reaction,

$$Y = \frac{Y_1 Y_2}{Y_3 Y_4 Y_5}. \tag{176}$$

For a locally reacting surface $\frac{\rho_0 f}{\sigma} < 10^{-3}$ the following terms are employed,

$$w = \frac{1}{2}(1 - j)\sqrt{2k(r_S + r_R)}(\cos\phi + \frac{\rho_0 c_0}{Z_g})\frac{1}{\sqrt{1 + \sin\phi}}, \tag{177}$$

$$Y_1 = Y_3 = \cos\phi + \frac{\rho_0 c_0}{Z_g}, \tag{178}$$

$$Y_2 = \sqrt{1 + \sin\phi}, \tag{179}$$

$$Y_4 = 1, \tag{180}$$

$$Y_5 = \sqrt{2\sin\phi}, \tag{181}$$

$$Y_6 = Y_2^2. \tag{182}$$

For a extensively reacting surface $\frac{\rho_0 f}{\sigma} \geq 10^{-3}$ the following terms are employed,

$$w = \frac{1}{2}(1-j)\sqrt{2k(r_S + r_R)}\frac{Y_3}{\sqrt{Y_6}}, \tag{183}$$

$$Y_1 = \left[\cos\phi + \frac{\rho_0 c_0}{Z_g}\sqrt{1 - \frac{k^2}{k_g^2}\sin^2\phi}\right]\sqrt{1 - \frac{k^2}{k_g^2}}, \tag{184}$$

$$Y_2 = \left[\sqrt{1 - \frac{\rho_0}{\rho_g^2}} + \frac{\rho_0 c_0}{Z_g}\sqrt{1 - \frac{k^2}{k_g^2}}\cos\phi + \left(1 - \left(\frac{\rho_0 c_0}{Z_g}\right)^2\right)\sin\phi\right]^{1/2}, \tag{185}$$

$$Y_3 = \cos\phi + \frac{\rho_0 c_0}{Z_g}\sqrt{1 - \frac{k^2}{k_g^2}}\left(1 - \frac{\rho_0}{\rho_g^2}\right)^{-1/2}, \tag{186}$$

$$Y_4 = \sqrt{1 - \frac{k^2}{k_b^2}\sin\phi}, \tag{187}$$

$$Y_5 = \sqrt[3]{1 - \frac{\rho_0}{\rho_g^2}}\sqrt{1 - (\frac{\rho_0 c_0}{Z_g})^2}\sqrt{2\sin\phi}, \tag{188}$$

$$Y_6 = 1 + \left(\frac{\rho_0 c_0}{Z_g}\sqrt{1 - \frac{k^2}{k_b^2}}\cos\phi + \sqrt{1 - \frac{\rho_0 c_0}{Z_g}}\sin\phi\right)\left(1 - \frac{\rho_0}{\rho_g^2}\right)^{-1/2}. \tag{189}$$

The term g(w) includes the complementary complex error function erfc() by Abramowitz and Stegun and is approximated depending on the value of the numerical distance. Therefore, let w_r be the real part of w and w_i be the imaginary part of w. If $w_r \leq 3.9$ and $w_i \leq 3$, g(w) is given as,

$$g(w) = -\sum_{i=1}^{2} H_3 + j\sum_{i=1}^{3} K_i, \tag{190}$$

$$H_1 = \frac{0.8w_i}{\pi(w_r^2 + w_i^2)} + \frac{2w_i \cdot 0.8}{\pi}\sum_{n=1}^{5}\frac{e^{-0.64n^2}(w_r^2 + w_i^2 + 0.64n^2)}{(w_i^2 - w_r^2 + 0.64n^2)^2 + 4w_r^2 w_i^2}, \tag{191}$$

$$H_2 = \begin{cases} T_H & \text{if } w_i < \dfrac{\pi}{0.8}, \\ \dfrac{1}{2}T_H & \text{if } w_i = \dfrac{\pi}{0.8}, \\ 0 & \text{if } w_i > \dfrac{\pi}{0.8}, \end{cases} \tag{192}$$

$$H_3 = \frac{w_r}{\pi} \cdot \frac{2\sqrt{\pi}\exp\left\{-(\frac{\pi^2}{0.64})\right\}}{1 - \exp\left\{-(\frac{\pi^2}{0.64})\right\}} \tag{193}$$

$$T_H = 2 \exp\left\{-[w_r^2 + 2(w_i \frac{\pi}{0.8}) - w_i^2]\right\} \frac{X_1 X_3 - X_2 X_4}{X_3^2 + X_4^2}, \tag{194}$$

$$K_1 = \frac{0.8 w_r}{\pi(w_r^2 + w_i^2)} + \frac{2 w_r \cdot 0.8}{\pi} \sum_{n=1}^{5} \frac{e^{-0.64 n^2}(w_r^2 + w_i^2 - 0.64 n^2)}{(w_i^2 - w_r^2 + 0.64 n^2)^2 + 4 w_r^2 w_i^2}, \tag{195}$$

$$K_2 = \begin{cases} -T_k & \text{if } w_i < \dfrac{\pi}{0.8}, \\ -\dfrac{1}{2} T_k & \text{if } w_i = \dfrac{\pi}{0.8}, \\ 0 & \text{if } w_i > \dfrac{\pi}{0.8}, \end{cases} \tag{196}$$

$$K_3 = \frac{w_r}{\pi} \cdot \frac{2\sqrt{\pi} \exp\left\{-(\frac{\pi^2}{0.64})\right\}}{1 - \exp\left\{-(\frac{\pi^2}{0.64})\right\}} \tag{197}$$

$$T_K = 2 \exp\left\{-[w_r^2 + 2(w_i \frac{\pi}{0.8}) - w_i^2]\right\} \frac{X_1 X_4 + X_2 X_3}{X_3^2 + X_4^2}, \tag{198}$$

$$\begin{array}{ll} X_1 = \cos(2 w_r w_i), & X_2 = \sin(2 w_r w_i), \\ X_3 = \exp\left\{-2 w_i \frac{\pi}{0.8}\right\} - \cos\left(2 w_r \frac{\pi}{0.8}\right), & X_4 = \sin\left(2 w_r \frac{\pi}{0.8}\right). \end{array} \tag{199}$$

If $w_r > 3.9$ or $w_i > 3$ and for both applies $w_i, w_r \leq 6$, g(w) is given as,

$$g(w) = jw\left(\frac{0.4613135}{w^2 - 0.1901635} + \frac{0.09999216}{w^2 - 1.7844927} + \frac{0.002883894}{w^2 - 5.5253437}\right). \tag{200}$$

If $w_i, w_r > 6$, g(w) is given as,

$$g(w) = jw\left(\frac{0.5124242}{w^2 - 0.275255} + \frac{0.05176536}{w^2 - 2.724745}\right). \tag{201}$$

3.11 Linear Sound Speed Profile

This section describes the definition of the linear sound speed profile, which is employed in other sections for the calculation of the sound speed at a certain height. Before the linear approximation of the sonic profile can be determined, the wind speed The idea for a linear approximation of the sonic profile is inspired by Hidaka et al. [14] and the approximation method itself is taken from Hansen et al. [13] based on Plovsing [29]. In the following description, units are omitted for the sake of clarity, but are listed in Table 13. In general heights are considered in meters, time is considered in seconds and temperature in kelvin.

The vertical wind speed gradient is generally related to the fluctuations of ground properties, or in suitable terminology the *surface roughness length* z_0. For a neutral atmosphere (Pasquill stability category D), the logarithmic velocity profile in Equation (202) approximates the wind speed at a certain height. Values of z_0 can be obtained by ground surface studies and U_0 represents the measured wind speed at height of h_0,

$$U(h) = U_0 \frac{\ln(h/z_0 + 1)}{\ln(h_0/z_0 + 1)}. \tag{202}$$

Symbol	Description	Unit
	Input	
h_S	The height of the source above the ground.	m
h_R	The height of the receiver above the ground.	m
U_0	Measured wind speed component at height h_0.	m/s
h_0	The height of the anemometer above the ground.	m
z_0	Surface roughness length.	m
T_G	Temperature at ground height (1 m above ground).	K
$\frac{\mathrm{d}T}{\mathrm{d}h}$	The vertical temperature gradient.	K $\cdot$m^{-1}
	Output	
$c(h)$	Linear sound speed profile.	m $\cdot$s^{-1}
ξ_n	Normalized sound speed gradient.	-

Table 13: Input and output for the calculation of the linear sound speed profile.

The first step to derive an equivalent linear sound speed profile, is the combination of the wind gradient and the temperature gradient. The procedure is based on the assumption, that the contribution of wind speed and temperature to the sonic gradient can be related with a linear and a logarithmic term. Consequently, the sound speed at a certain height is calculated as written in Equation (203), where A is the constant for wind speed and B is the constant for temperature,

$$\hat{c}(h) = A \cdot \ln(\frac{h}{z_0} + 1) + B \cdot h + c_0. \tag{203}$$

The parameter $c_0 = 331.3\,\mathrm{m/s}$ represents the sound speed at ground sea level with stationary air (Pasquill stability category D) at 273.15 K. With reference to Section 2.2.3, the speed of sound at height h is proportional to the temperature T in kelvin, which concludes to Equation (204),

$$c = c_0\sqrt{T/273}. \tag{204}$$

Thereby, the vertical sound speed gradient due to the atmospheric ambient temperature is obtained by differentiating Equation (204) with respect to h, resulting in Equation (205). Parameter T_G is the atmospheric ambient temperature at 1 m height, sound speed c_T is calculated with Equation (204) at $T = T_G$ and $\frac{dT}{dh}$ is constant,

$$B = \frac{\partial c}{\partial h_T} = \frac{\mathrm{d}T}{\mathrm{d}h}\frac{\partial c}{\partial T} = \frac{\mathrm{d}T}{\mathrm{d}h}\frac{1}{\sqrt{T}}\frac{c_T}{2\sqrt{273}} = \frac{\mathrm{d}T}{\mathrm{d}h}\frac{10.025}{\sqrt{T_G}}. \tag{205}$$

The logarithmic term is based on Equation (202), which factorizes constant A as in Equation (206),

$$A = \frac{U_0}{\ln(\frac{h_0}{z_0} + 1)}. \tag{206}$$

The equivalent linear sound speed profile used for the calculation of the curvature is written in Equation (207),

$$c(h) = c_G + \frac{\Delta c}{\Delta h} h = c_G \cdot (1 + \xi_n h). \tag{207}$$

The sound speed gradient $\frac{\Delta c}{\Delta h}$ is defined as the average gradient between h_R and h_S. It is determined according to Equation (208). In addition, ξ_n in Equation (209) is the sound speed gradient normalised with c_G. The sound speed c_G at the lowest height is calculated with the average sound speed at the average height between h_R and h_S as follows,

$$\frac{\Delta c}{\Delta h} := \frac{\hat{c}(h_S) - \hat{c}(h_R)}{h_S - h_R}, \tag{208}$$

$$\xi_n = \frac{\Delta c}{\Delta h} \frac{1}{c_G}, \tag{209}$$

$$\bar{c} = \frac{1}{h_S - h_R} \int_{h_R}^{h_S} \hat{c}(h) \, dh, \tag{210}$$

$$c_G = \bar{c} - \frac{\Delta c}{\Delta h} \frac{h_S + h_R}{2}. \tag{211}$$

The premise for the above calculations is $h_S > h_R$ and an atmosphere which is near enough to neutral conditions for validity of Equation (202). That means extreme atmospheric conditions are not in the scope of the above analysis. As Plovsing [29] suggests, to avoid extreme values of the average sound speed gradient for low receiver heights, the parameters are limited with $h_{\min} = 5z_0$. If the parameter is below this limit, $h_{\min}$ is used instead. To differentiate between an upward refracting atmosphere ξ_n is considered as the determining condition. For downward refraction $\xi_n > 0$ and for upward refraction $\xi_n < 0$.

4 Model Validation and Results

In connection with this work, an implementation of the model in *TypeScript* was carried out. The choice of the programming language is based on the introductory motivation for this project. The aim was the development of a noise propagation model which can be executed on any machine, particularly in a browser. Figure 27 illustrates the structure of the software. The modular design is based on the basic formula of the model. For each attenuation term there is a module that performs the corresponding calculations for each source receiver pair and center frequency. This structure allows adding, replacing and extending any attenuation process and makes the model dynamically expandable for future use.
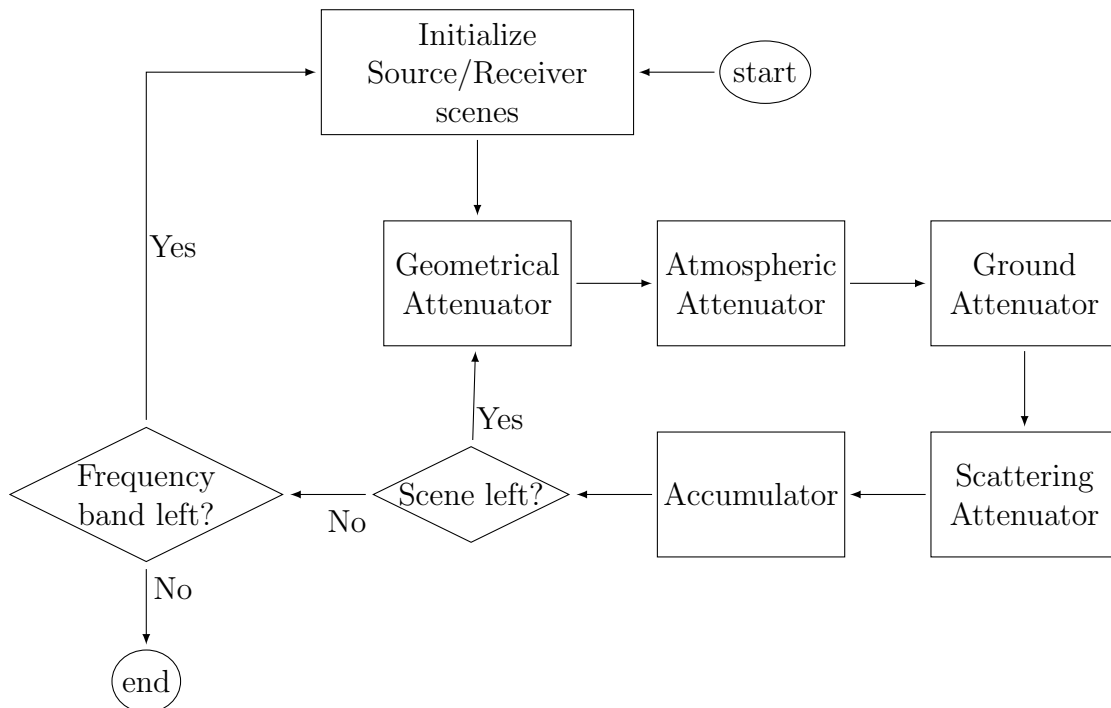
Figure 27: The modular structure of the model implementation. For every 1/3 center frequency a source-receiver pair is evaluated. For every receiver the resulting sound pressure level at every center frequency is summed in the accumulator. After all frequencies are processed, the model terminates with the spectral sound pressure levels for every given receiver location.

Based on this implementation, the next sections evaluate every module by comparing the individual results to measurements if available, otherwise results are compared to existing models. In order to demonstrate the sophisticated approach applied, the reference model is the widely employed ISO-9613. This way, results are validated and parameter studies present relevant domains of the underlying parameters. In general, it should be noted that in this context the following assumptions are made. First of

all, the spectrum in which wind turbines generate sound is set to 10 - 8 kHz. This range is based on measurement studies in Reference [26] and [20]. While it should be noted that the spectrum depends on the size of the wind turbine, the environmental conditions and various other factors, the given boundaries apply in general. However, the greatest emission is determined to be in the range of 200 Hz to 5 kHz. Besides the noise spectrum, it is necessary to stress the acceptable level of accuracy based on the project scope. By referring to Figure 3 in Section 2.1.1, it is not possible to give exact values for an acceptable error due to the nature of human perception. Nevertheless, an allowed deviation, derived from the equal loudness contours, offers initial approximations. If the sound signal has a SPL of 16.7 dB at 500 Hz, we can conclude from the curve for 20 phon, that the volume is perceived as equal for a SPL of 14.5 dB at 400 Hz and 18.6 dB at 630 Hz. That means, for a continuous signal in the 500 Hz band, an interpolation provides an acceptable range for the SPL value concerning the perception of equal loudness. Consequently, the following holds true for the example named above, within the 500 Hz band a deviation of -1.4 dB and $+3.3$ dB is thereby adequate. It must be pointed out at this point that this thesis does not pursue a deep analysis of the perception of environmental noise. This means that the given acceptable errors are only rough estimates.

4.1 Atmospheric Attenuation

This section shows results of the atmospheric attenuation module and introduces carefully determined domains for the necessary parameters. First of all it should be noted that the original Reference [15] already limits the method to temperatures between $-20\,°C$ and $+50\,°C$, a relative humidity from 10 % and 100 % and atmospheric pressure less than 200 kPa. At this range, the formula is valid for an altitude up to 3 km and the accuracy for pure tones is estimated at ± 10 %. Considering normal conditions and the sound spectrum of wind turbines, this error can lead to a deviation of 0.2 dB/(100m·atm) at 8 kHz. This means after 1 km distance an error of $\pm\,2$ dB. While this value might not be suitable for strict engineering purposes, it is still feasible in the context of auditory simulation. Besides this inherent imprecision, the general behaviour for different frequencies is clearly visible and meets the expectations. Figure 28 is based on the idea of Bass et al. [4] and shows the increase of the attenuation coefficient per atmosphere. The scaling with pressure at $20\,°C$ provides a graph for use with any pressure value. For example in order to find the value of α_{atm} at 2000 Hz at $20\,°C$, 10 % relative humidity and atmospheric pressure of 202.652 Pa $= 2$ atm, the values given in the figure can be found by dividing the input value by 2. With this representation of the coefficient, the linear relation of pressure and frequency is precisely articulated. Thus, by including the prior provided limits of the formula, increasing frequency and/or increasing pressure cause an approximate linear increase of the atmospheric absorption.

For the relative humidity, additional model results are provided in Figure 29 at $20\,°C$ and normal pressure $p_N = 101.325$ Pa for a range of relative humidity values. In gen-
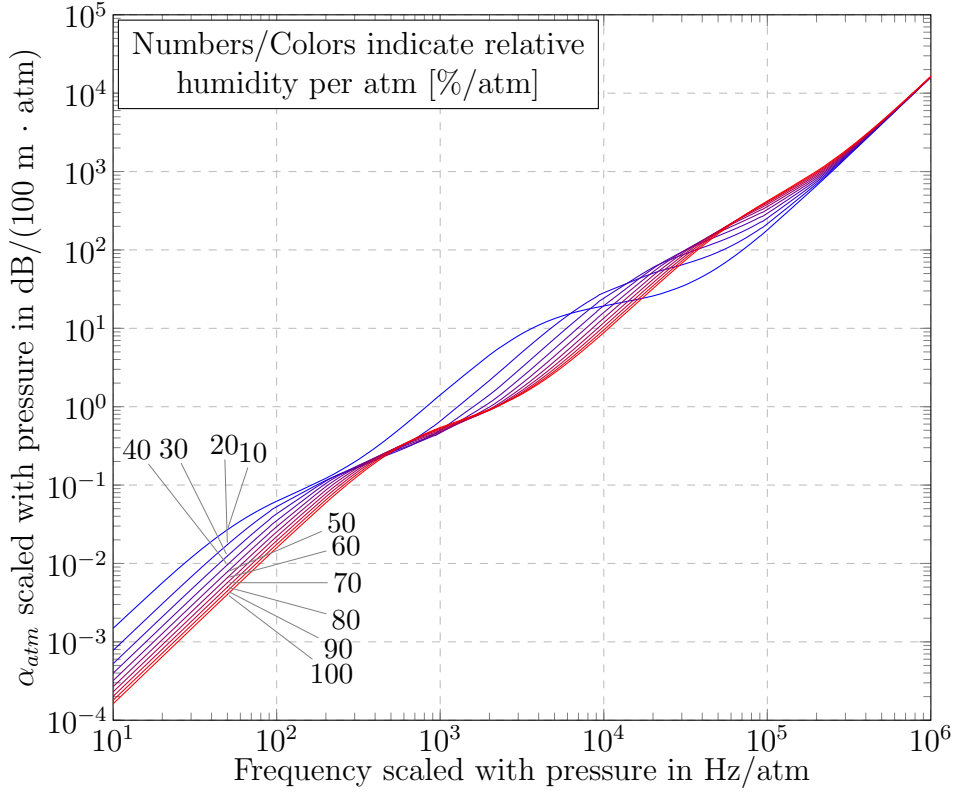
Figure 28: The attenuation coefficient per atm with frequency per atm on the abscissa. The pinned numbers describe the corresponding relative humidity per atm.

eral it can be seen that the attenuation increases with less humidity at the relevant frequency range. However, as seen in Figure 29b, the peak at which the attenuation starts decreasing shifts with higher frequencies. This effect is related to the correlation of humidity and relaxation frequencies of the involved molecules. This can be seen in the corresponding Equations (85) and (86), where the humidity is included as the dominant parameter in the relaxation frequencies f_N and f_O. With increasing frequency, the decline caused by the relaxation frequency is weakened by the center frequency term. Thus, a higher center frequency requires a higher humidity for the steady decrease rate. Referring to Rudolf Geiger [32], a physically realistic value for the lower atmosphere at midday is approximately $50 - 80\%$ relative humidity. It follows that for most scenarios it is safe to assume that with increasing humidity the model will predict less atmospheric attenuation. The temperature effect on α_{atm} is more elusive. Figure 29b shows how humidity and temperature interact. While it can be seen that for temperatures below $0\,^\circ\text{C}$ the attenuation coefficient increases with increasing humidity, the curves have no pronounced peak as previously described. Higher temperatures seem to shift the peak to lower humidity values, similar to the effect of higher frequencies. As a general guidance for the interaction of temperature and relative humidity, it can be said that the higher the temperature the more sensitive the attenuation coefficient reacts to a change in the relative humidity.
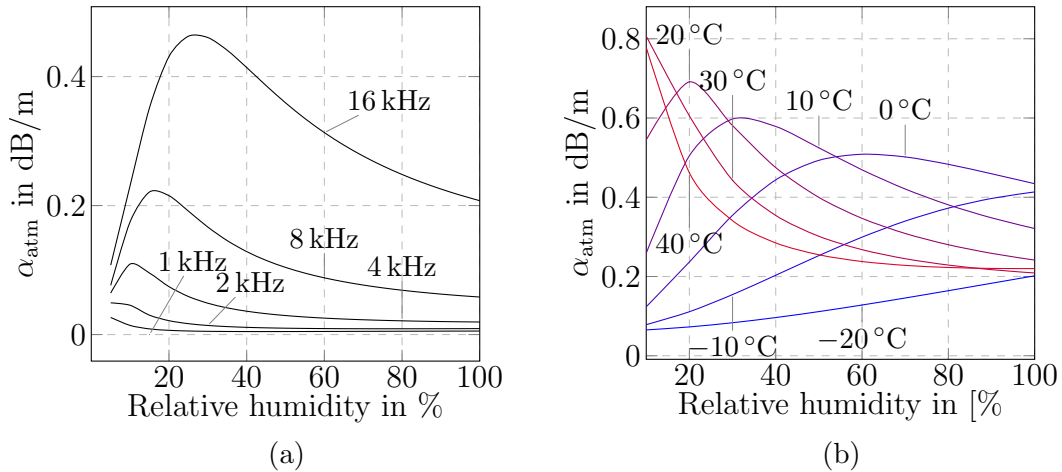
Figure 29: The correlation of relative humidity and temperature at a frequency of 2 kHz. Increase in temperature shifts the attenuation peak to lower values of relative humidity.

Lastly, Figure 30 illustrates the correction term applied in Equation 90 for frequency band errors. As this coefficient has a theoretically foundation it is empirically determined and compensates the overprediction of the coefficient at high frequencies. Figure 30 outlines how the difference between uncorrected pure tone attenuation and corrected attenuation increases with the value of attenuation. That implies that especially high frequencies are corrected downwards.
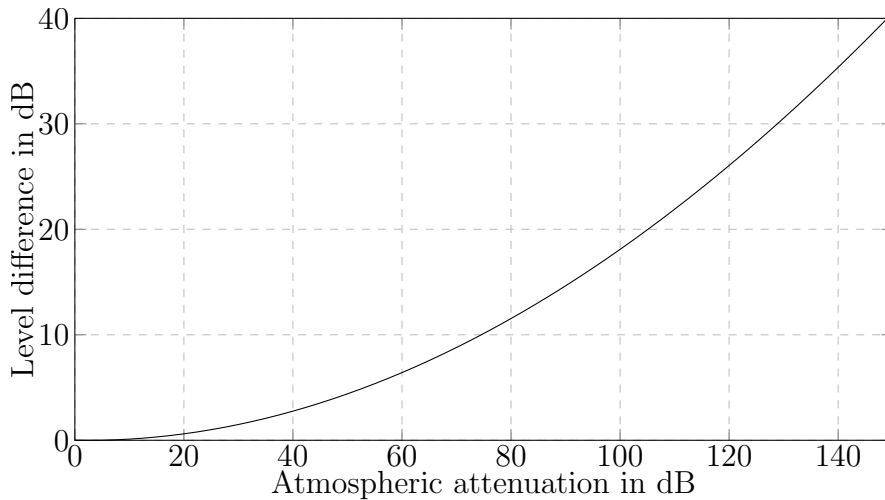
Figure 30: The difference between the pure tone attenuation and the corrected value for frequency bands. The ordinate contains the difference between the uncorrected level (abscissa) and the corrected level.
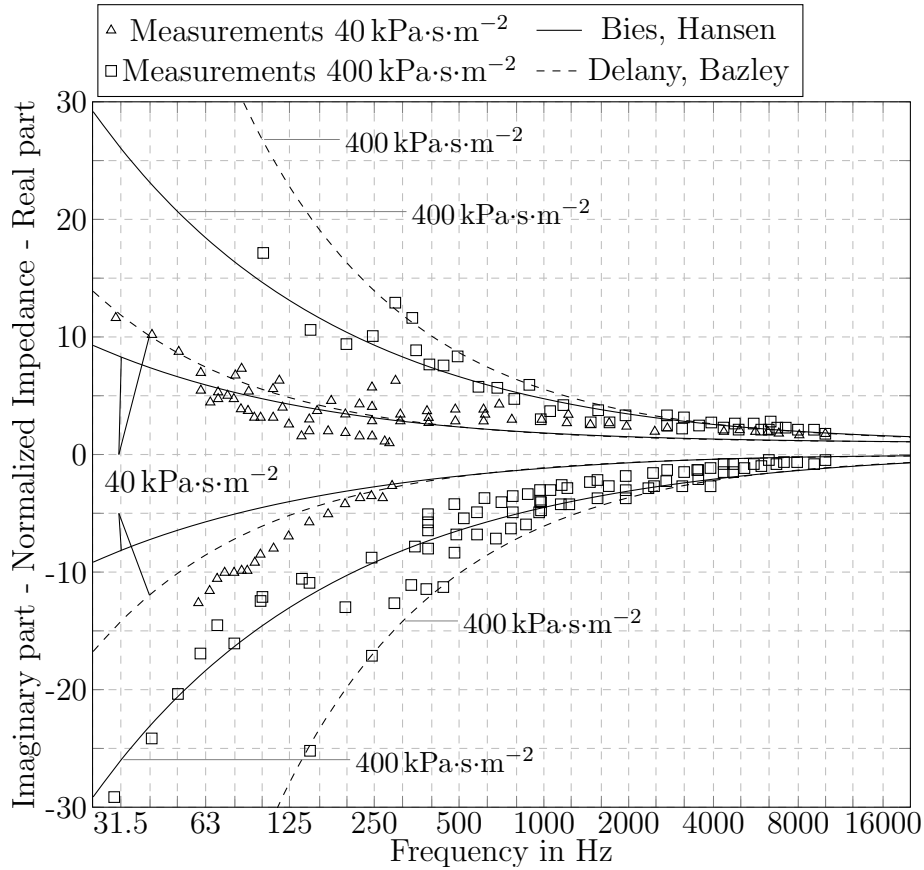
Figure 31: Comparison of the characteristic impedance predicted by the applied methods from Hansen et al. [13] and Delany and Bazley [9] measurements by reproduced from Crocker [8]

4.2 Ground Attenuation

The most simple representation of ground properties in regard to sound waves, is the classification into categories from acoustically hard to soft as in the ISO 9163 model. This oversimplification neglects strong differences inside these categories and by assigning simple reflection coefficients to this categories, the phase relations of the involved sound waves are completely disregarded. A more extensive approach is implemented in the model as described in Section 3.9, by calculating the characteristic impedance of the ground. The basis for the calculations are empiric best fits over measurements. While the original formula introduced by Delany and Bazley [9] tends to produce physical unrealistic values in case that the single input parameter is very high, the modification by Hansen et al. [13] which is used by the model counteracts this problem. Figure 31 lists measurements from different studies for normalized characteristic impedance values at $40\,\mathrm{kPa{\cdot}s{\cdot}m^{-2}}$ and $400\,\mathrm{kPa{\cdot}s{\cdot}m^{-2}}$. In addition the calculated impedance values of Reference [9] and Reference [13] are shown. As listed in Table 14, the model of Delany and Bazley [9] is closer to the measurements. It is important to emphasize that the given values come from different studies which were made independent of both methods.

63

Method	Absolute	Real part	Imaginary part
Bies, Hansen 40 kPa·s·m^{-2}	2.20	1.45	3.89
Delany, Bazley 40 kPa·s·m^{-2}	1.71	1.56	2.20
Bies, Hansen 400 kPa·s·m^{-2}	5.70	4.13	6.31
Delany, Bazley 400 kPa·s·m^{-2}	5.09	4.03	5.53

Table 14: Metrics of the comparison between different impedance calculations. The root mean square deviation (RMSD) is given for real part and imaginary part of the impedance. The absolute deviation denotes the difference of imaginary and real part.

Concerning the result, the only exception to the general better result of the approach by Delany and Bazley [9] is the 40 kPa·s·m^{-2} case, where the prediction of Hansen et al. [13] is closer to the measurement. That behaviour fits expectations, resulting in the use of the formula of Hansen et al. [13] for flow resistivity values above 500 kPa·s·m^{-2} and the formula of Delany and Bazley [9] below this boundary as suggested by Hansen et al. [13].

4.2.1 Test Case 1 - Høvsøre

In order to illustrate the difference of the more sophisticated ground model, Figure 32 shows the results of the ISO 9163 prediction and the thesis model prediction with measurements from Søndergaard and Plovsing [33]. Additionally, to further investigate the difference between the predicted impedance values, one calculation is carried out with the formula given by Delany and Bazley [9] and one with the formula by Hansen et al. [13].

The well documented measurements provide two test cases. The first one is a test site at *Høvsøre* in Denmark, where individual turbines on a flat agricultural ground were tested. It should be noted that for this and subsequent measurements from the reference, parameters have been applied wherever possible. For the remaining, estimates are applied which fit the description given in the reference. Figure 32 illustrates the different prediction results. According to ISO 9163, grass is considered a porous ground and thus classified with the ground factor $G = 1$. Whereas the thesis model uses a measured flow resistivity value of $\sigma = 600$ kPa·s·m^{-2} for grassland. For the validity of the ISO 9163 methods, the source and receiver heights are chosen to be relatively close to the ground. Table 15 lists the input parameters of the model. To allow for comparison, the calculation was carried out in octave bands and in the frequency range of measurement data. In this case, the comparison between the two used impedance predictions is remarkable, since it greatly shows how the prediction of the impedance improves when the flow resistivity exceeds 500 kPa·s·m^{-2}. Furthermore, a general improvement compared to the ISO 9163 prediction is clearly visible. Although the scenario lies within the application area of the ISO 9163 method, the predicted attenuation at the lowest frequency band with 125 Hz differs by an amount of 5.4 dB.

Parameter	Case 1 - Høvsøre	Case 2 - Høvsøre	Case 3 - Hitra
Temperature at ground level	293.15 K (20 °C)	293.15 K (20 °C)	293.15 K (20 °C)
Temperature lapse rate	$-0.06\,\mathrm{K/m}$	$0.06\,\mathrm{K/m}$	$0.06\,\mathrm{K/m}$
Wind speed at 10 m above the ground	5 m/s	5 m/s (-5 for up-wind)	5 m/s
Surface roughness length [13]	0.01 m	0.01 m	0.05 m
Average ground height variation	0 m	0 m	0.1 m
Ground flow resistivity [13]	$600\,\mathrm{kPa{\cdot}s{\cdot}m^{-2}}$	$600\,\mathrm{kPa{\cdot}s{\cdot}m^{-2}}$	$1000\,\mathrm{kPa{\cdot}s{\cdot}m^{-2}}$
Wind turbulence constant C_v	$0.012\,\mathrm{m^{4/3}{\cdot}s^{-2}}$	$0.012\,\mathrm{m^{4/3}{\cdot}s^{-2}}$	$0.012\,\mathrm{m^{4/3}{\cdot}s^{-2}}$
Temperature turbulence constant C_v	$0.0008\,\mathrm{K{\cdot}s^{-2}}$	$0.0008\,\mathrm{K{\cdot}s^{-2}}$	$0.0008\,\mathrm{K{\cdot}s^{-2}}$
Atmospheric pressure	1.205 Pa	1.205 Pa	1.205 Pa
Relative humidity	50 %	50 %	50%

Table 15: Input parameters for the thesis model for a neutral atmosphere. Most values are taken from Rudolf Geiger [32], other source are referenced.

As shown in Table 16, the root mean square deviation of the thesis model improves notably from the prediction of the ISO 9163 prediction. However, at the 250 Hz band the ISO 9163 method provides the best result and it is interesting to see that every prediction seems to underestimate the attenuation at this band. Overall it can be concluded from this test case that the general prediction accuracy has improved somewhat compared to the ISO 9163 model and the application of the more current impedance method has also achieved an improvement in the specified parameter boundary. Furthermore, it can be said that the thesis model does not exceed the introduced error metric in any band, while the reference calculations do slightly exceed the error metric at lowest frequency band.

4.2.2 Test Case 2 - Høvsøre

The previous test case included a scenario in which both models were valid. Nevertheless, another reason to implement more refined methods for the ground attenuation is the inflexibility of the ISO 1963 method. Upwind conditions or temperature lapse rates are are not included. In order to illustrate this difference, a test case for upwind

Model	Case 1 - Høvsøre	Case 2 - Høvsøre	Case 3 - Hitra
Thesis model (Bies & Hansen)	1.8	3.66	9.49
Thesis model (Delany & Bazley)	3.16	-	-
ISO-9613	3.36	9.91	-

Table 16: Metrics of the comparison between different ground attenuation predictions and measurements. The root mean square deviation (RMSD) in dB denotes the deviation from measurements.

Figure 32: Ground attenuation from 125 Hz to 2 kHz. The source is located at 30 m above the ground, the receiver is at 2 m above the ground and the horizontal distance amounts 500 m. Positive values of the ground attenuation denote a contribution to the SPL at the receiver.

conditions with a normal temperature lapse rate as given in Table 16 was carried out in [33]. The input parameters produce a considerable shadow zone in which the negative attenuation is clearly more pronounced as in downwind conditions. While the ISO 9163 is not capable of capturing this effect the prediction of the thesis model shows acceptable results within the prior given acceptable error boundary. The associated root mean squared deviation in is listed in Table 16.

4.2.3 Test Case 3 - Hitra

Besides an improved ground approximation in comparison to the ISO 9163 model, there are more properties which are still to be taken into account. An important condition for previous test cases was the homogeneous ground regarding height and composition. The consequences of this simplification can be seen in measurements
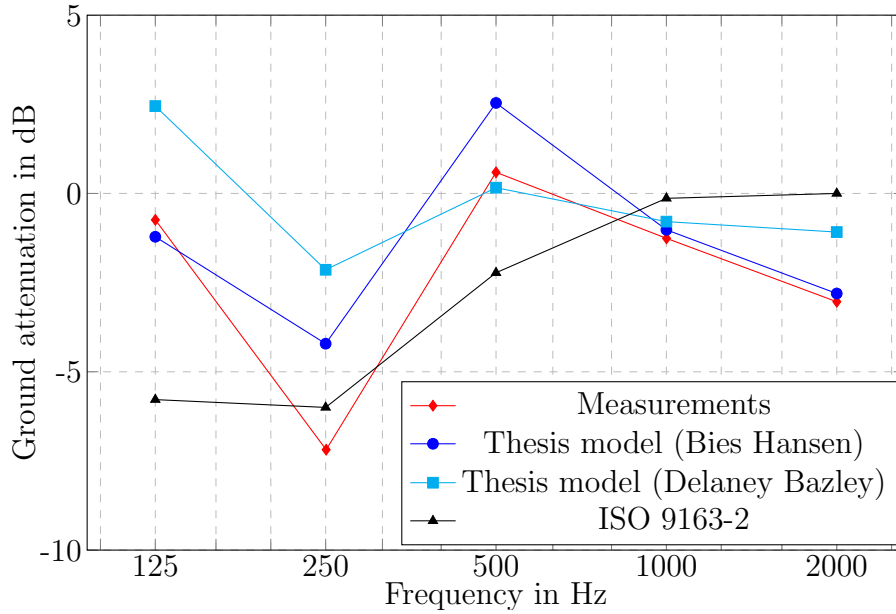
Figure 33: Ground attenuation from 125 Hz to 2 kHz. The source is located 30 m above the ground, the receiver is 2 m above the ground and the horizontal distance amounts 1000 m. Positive values of the ground attenuation denote a contribution to the SPL at the receiver.

at the wind farm *Hitra* in Norway. In the carried out case study, the average height difference between the source receiver geometry amounts 260 m. Furthermore, the ground composition is a mixture of rocks and hard soil, covered with thin surface of grass. While the height variation is only considered in the partial coherence coefficients, it is completely disregarded when calculating ray paths. In addition, the variation in the flow resisitivity of the ground is completely neglected when reflection with surface and ground waves is determined. As shown in Figure 34, the deviation of the thesis model is much more pronounced than in previous cases. The root mean squared deviation increases to 9.49 dB and especially at the frequency range above 500 Hz the error rises up to 13.88 dB, which is above the acceptable error boundary.

4.3 Attenuation of Scattering Zones

To investigate the results of the scattering zone module, the study of Reference [39] is used for comparison. In this study the attenuation of different forests was investigated by simulating a broadband noise emission with specialized speakers. Measurements were carried out for a deciduous forest and coniferous forest with 220 m length expansion. Source (loudspeaker) and receiver (microphone) were located in 55 m distance from the timber line. Moreover, detailed measurements of the meteorological conditions were made to correlate the effect of refraction and fluctuations with results. Table 17 and Table 17 provide the input parameters which are explicitly given by the reference or estimates according to the description of the setup.
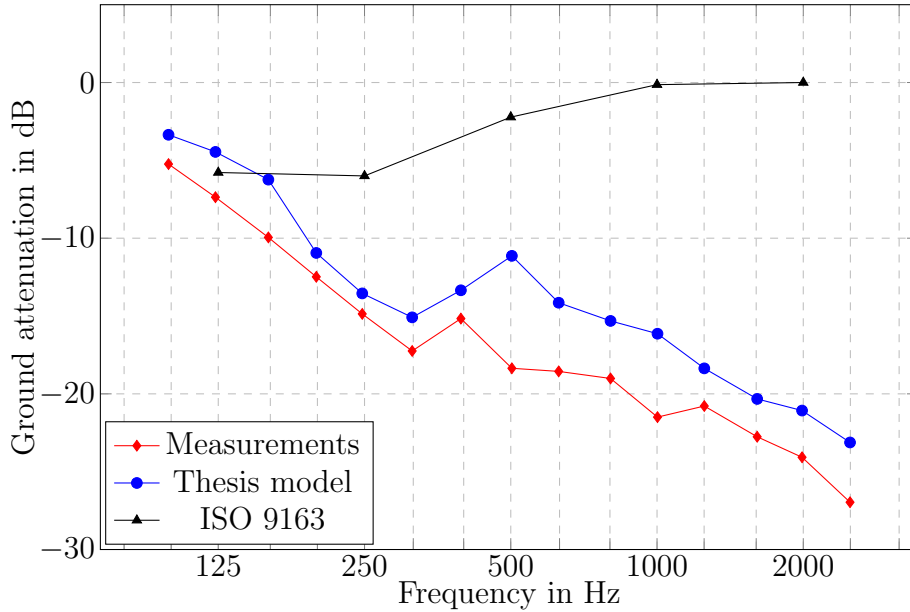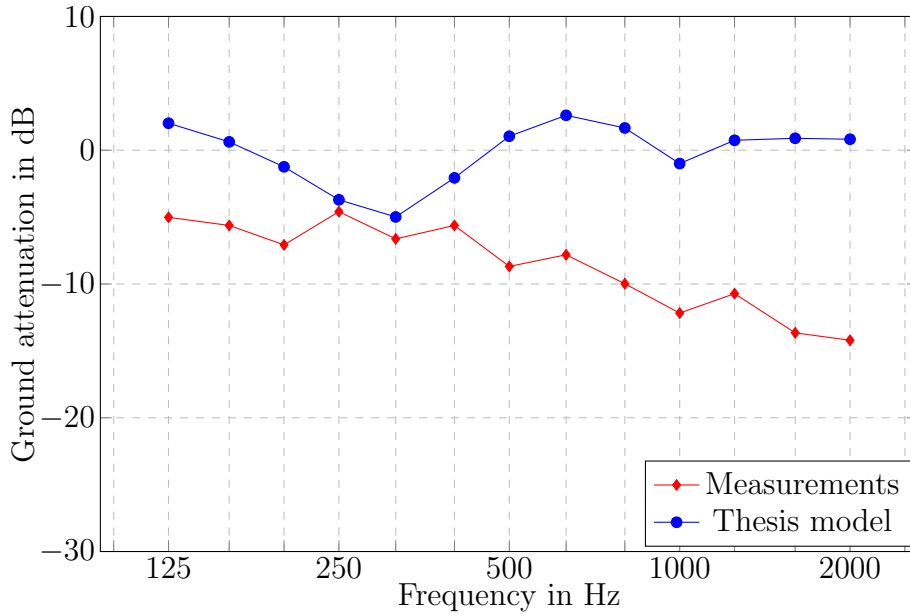
67

Figure 34: Ground attenuation at Hitra from 125 Hz to 2 kHz. The source is located at 70 m above the ground, the receiver is 2 m above the ground and the horizontal distance amounts 800 m. Positive values of the ground attenuation denote a contribution to the SPL at the receiver.

Resulting measurements for deciduous forest and coniferous forest including the corresponding calculations of the model are shown in Figure 35. The difference in both cases are significantly high, while the difference between forest types meets expectations. The ISO 9163 model does not include the meteorological conditions and thus severely underpredicts the attenuation effect. In the valid region from 125 Hz to 2 kHz the root mean square deviation is 28 dB which is far beyond the acceptable boundary. On the other hand, the root mean square deviation of the thesis model for both forest types is approximately 10 dB and individual deviation exceed 20 dB. This means the deviation is far beyond the acceptance limit. As clearly visible in the graph of both predictions, especially the lower frequency range is heavily error prone. The attenuation rise is shifted and steadily approaching its peak instead of the distinct curve at 500 - 1000 Hz. This behaviour is mainly related to the frequency weighting of Equation (109), where the coefficient k_f seems to underestimate the effects for frequencies below 250 Hz. Furthermore, the limit of 25 dB is due to the limitation of the formula by the author [30] and based on several supportive studies, which are in agreement to similar limits. Although it should be added that the situation from the study is not easily transferable to the model and therefore a notable error in the input parameters contributes to the high deviation, even when considering a deviation, which can be calculated from realistic deviations of the input parameter, no error below the specified one is reached. Nevertheless, the presented values from the study are average values with great deviations due to meteorological fluctuations. In conclusion, more

Source height	1 m
Receiver height	4 m
Horizontal distance between source and receiver	355 m
Average tree height	14 m
Trees per square meter	3 20
Average trunk diameter	0.7 m
Tree reflection coefficient	0.2
Length of the zone	220 m
Distance between source and start of the zone	55 m

Table 17: Input parameters for the coniferous forest scattering zone, described by Ziemann et al. [39].

measurement data is needed with distinct momentary recordings of the meteorological condition to validate the applied approach. Although this approach produces more compelling results and offers more scope of application compared to the ISO 9163 method, more investigation has to be done to ensure sufficient accuracy.

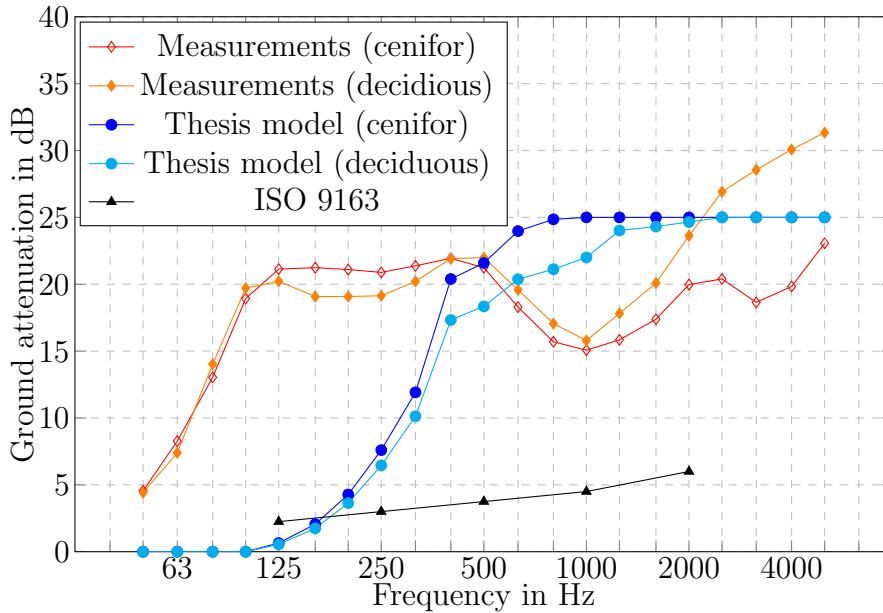Figure 35: Attenuation due to a coniferous forest at Langhennersdorf (Germany) from 25 Hz to 5 kHz. The source is located at 1 m above the ground, the receiver is 4 m above the ground and the horizontal distance amounts 355 m.

4.4 Exhaustive Simulation Results

This section shows the combined results of the model and afterwards transfers the application on complete wind farms instead of single scenes. Therefore, one simulation
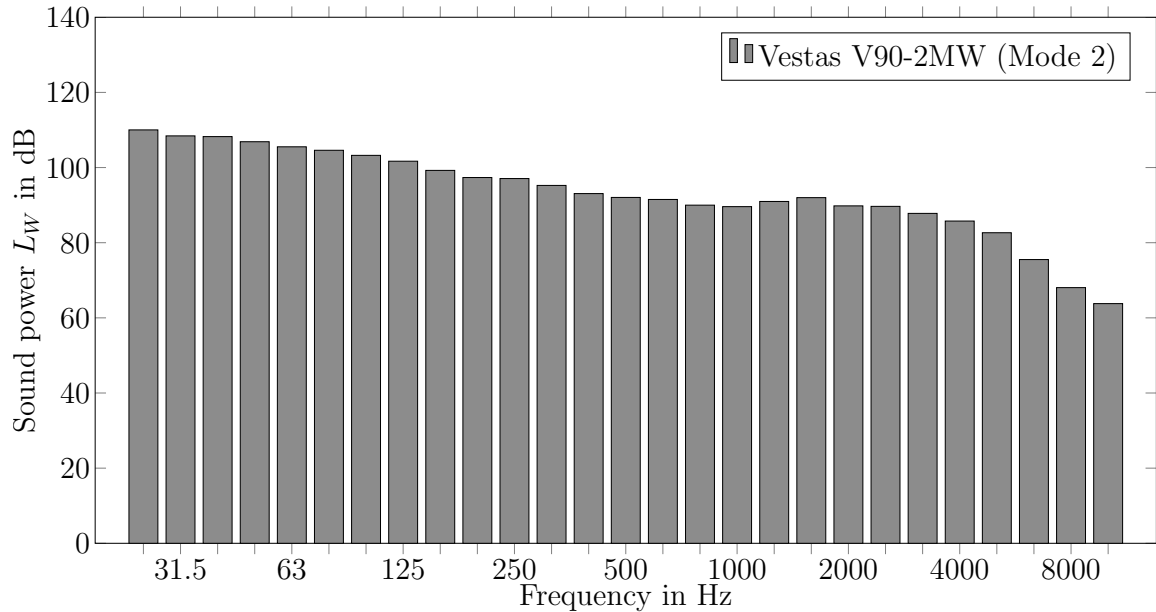
Figure 36: Sound power spectrum of the *Vestas V90-2MW (Mode 2)*. The data was modified from the original source by removing the A-weighting. [12]

for a single wind turbine is presented in Section 4.4.1. Additionally, Section 4.4.2 shows the results of the model when applied on a wind farm consisting of multiple turbines of the same type.

As pointed out in Reference [34], the strength of noise emission from wind turbines depends mainly on the type and wind speed. In this case, the term *type* refers to height, rotor diameter and nominal power. In general, it holds true that the more power a turbine produces and the bigger it gets, the higher the respective sound power of the whole spectrum becomes. As shown by Sondergaard [34] for a nominal power above 1 MW, the sound power of frequencies below 160 Hz increases at a rate of 0.43 dB per doubling of nominal power. That said, the difference is not particularly high and therefore such a clear statement about an increase of noise emission regarding the size of turbines is not possible. Similar applies for wind speed. Since the main source of sound generation is due to aerodynamic processes, different wind speeds have significant impact on the sound power spectrum. While the sensitivity to wind speed differences depends on a wide range of turbine characteristics, the general rule of thumb named above holds true aswell. The higher the wind speed, the higher is the total sound power level.

4.4.1 Simulation of a Single Wind Turbine

This section presents the result of a simulation based on the reference model *Vestas V90-2MW (Mode 2)*. Figure 36 shows the sound power levels obtained by removing the frequency weighting in Reference [12]. The measurements are in compliance with IEC 61400-11 [11] and dictate the corresponding wind speed and surface roughness

Parameter	Case 1	Case 2	Case 3
Source height	105 m	105 m	105 m
Receiver height	2 m	2 m	2 m
Receiver distances	up to 10 km	up to 10 km	up to 10 km
Temperature at ground level	283.15 K	283.15 K	283.15 K
Average ambient temperature	293.15 K	293.15 K	293.15 K
Temperature lapse rate	0.03 K/m	0.03 K/m	0.06 K/m
Wind speed at 10 m	8 m/s	15 m/s	5 m/s
Direction of wind	Northwest	Northwest	Northwest
Surface roughness length	0.05 m	0.05 m	0.05 m
Ground height variation	0 m	0 m	0 m
Ground flow resistivity	$600\,\mathrm{kPa\cdot s\cdot m^{-2}}$	$600\,\mathrm{kPa\cdot s\cdot m^{-2}}$	$600\,\mathrm{kPa\cdot s\cdot m^{-2}}$
Wind turbulence constant	$0.05\,\mathrm{m^{4/3}\cdot s^{-2}}$	$0.05\,\mathrm{m^{4/3}\cdot s^{-2}}$	$0.05\,\mathrm{m^{4/3}\cdot s^{-2}}$
Temperature turbulence constant	$0.1\cdot 10^{-4}\mathrm{K\cdot s^{-2}}$	$0.1\cdot 10^{-4}\mathrm{K\cdot s^{-2}}$	$0.1\cdot 10^{-4}\mathrm{K\cdot s^{-2}}$
Atmospheric pressure	1.205 Pa	1.205 Pa	1.205 Pa
Relative humidity	50 %	50 %	50%

Table 18: Input parameters for all Single Turbine Test Cases.

length applied in the simulation. Thus, the wind turbine is modelled as a point source at 105 m above the ground (hub-height) and a rotor diameter of 90 m. The meteorological conditions were chosen to be close to the conditions at point of measurement described in the reference. The input parameters for the different simulation parameters are listed in Table 18.

Figure 37 illustrates the produced results for Case 1. One the one hand Figure 37a depicts the results produced by the thesis model, one the other hand Figure 37b illustrates the results of the ISO-9613 model. Most notably, the huge difference in directional radiation is shown. This is mainly due to the application of different wind directions and refraction, which is completely ignored by the ISO-9613 model. Since a strong downwind situation occurs north-west wards from the turbine, the thesis model predicts a weaker sound attenuation in this direction. In this direction the RMSD value reduces to around 3.21 dB as opposed to an overall deviation of 187.88 dB. The darker color indicating strong attenuation appears when the receiver locations approach crosswind and upwind direction. This effect is caused by the appearance of meteorological shadow zones, where the temperature effect starts to prevail the wind speed effect and causes meteorological shadow zones with heavy attenuation. Figure 39 illustrates this behaviour with contrasting parameters for wind speed and temperature gradient. In Figure 39a a lighter temperature gradient with 0.03 °C per meter and a stronger wind gradient with 15 m/s result in a much broader emission shape, since the wind gradient is able to prevail the temperature effect much longer when approaching crosswind situations. Figure 39b illustrates the opposite, when the wind gradient is much lighter with

(a) Thesis Model.

(b) ISO-9613.

Figure 37: Contour plot of model results in a 10 km radius around the *Vestas V90-2MW (Mode 2)*, which is depicted a the white S-Symbol. Both figures take a top down (horizontal) perspective, with cardinal points as indicated on the axes.

(a) Prediction of the receiver R1.

(b) Prediction of the receiver R2.

Figure 38: Comparison of the predicted spectrum of the thesis model and the ISO-9613 model. The corresponding receiver coordinates are marked in Figure 37.

5 m/s combined with a stronger temperature gradient 0.06 K/m, the emission shape is much more narrow than before, since the temperature gradient prevails the wind

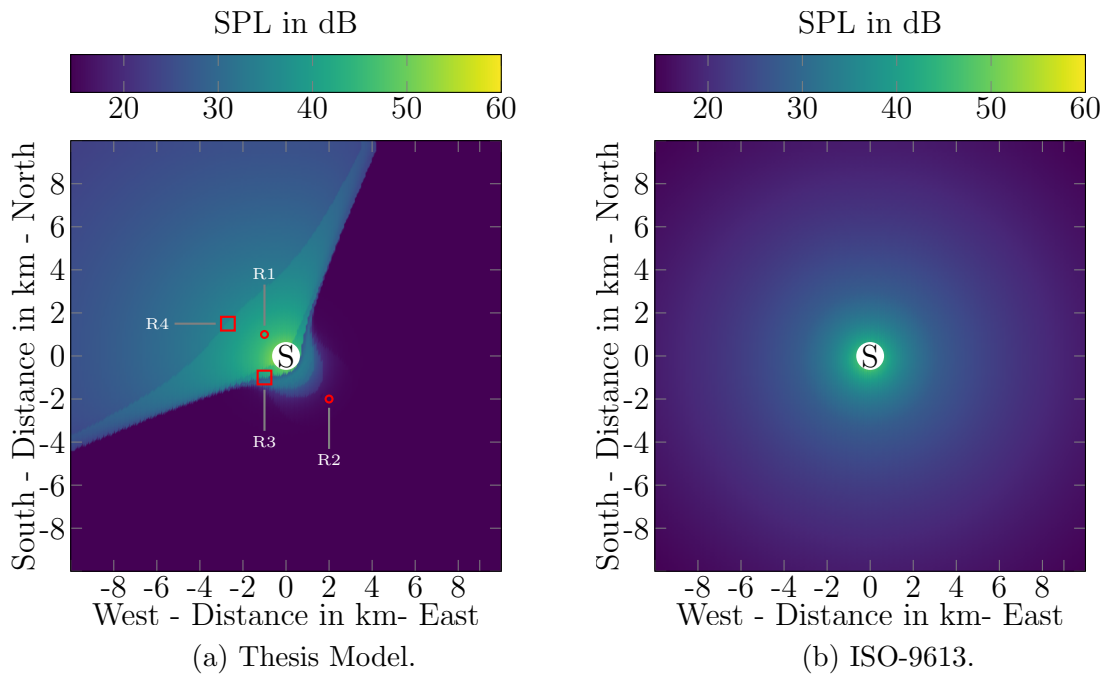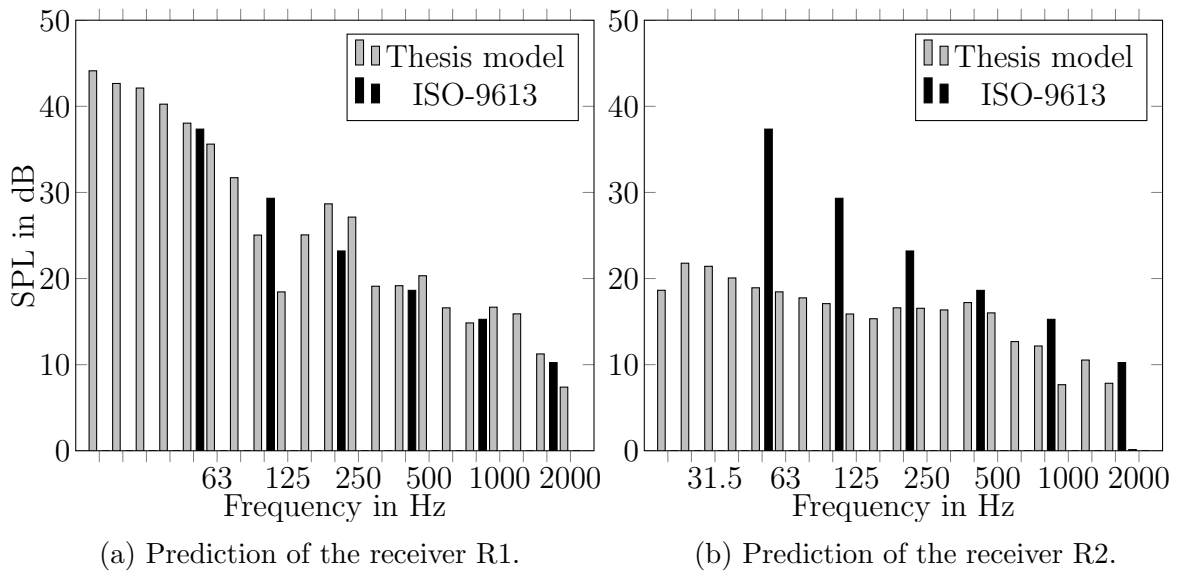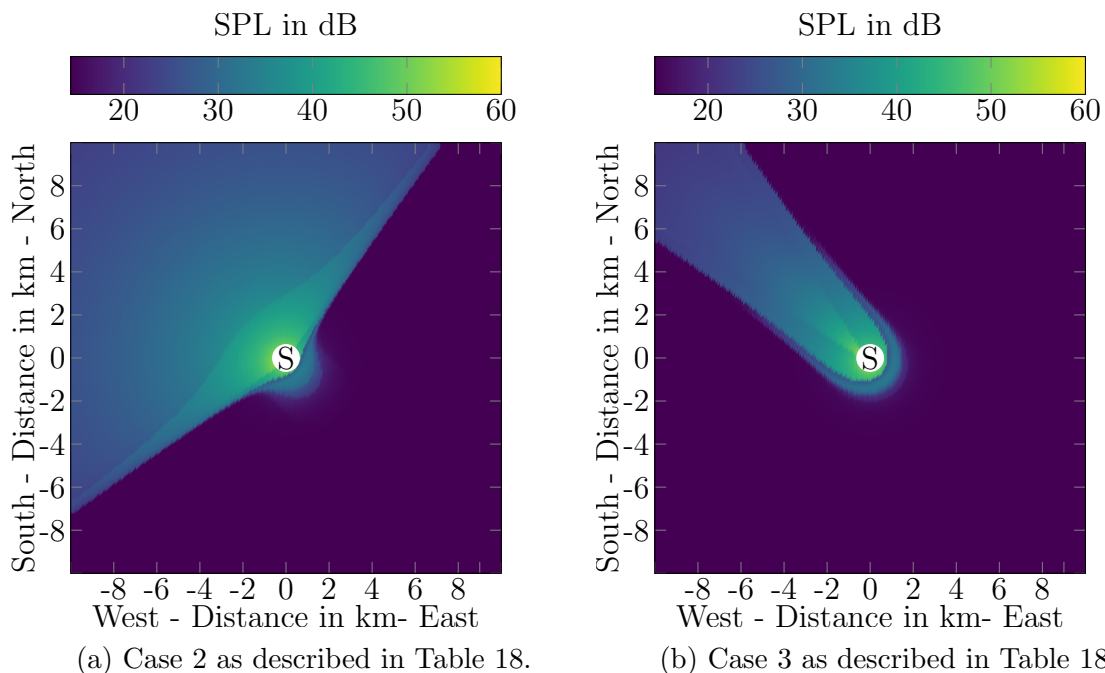(a) Case 2 as described in Table 18.   (b) Case 3 as described in Table 18.

Figure 39: Contour plot of model results in a 10 km radius around the *Vestas V90-2MW (Mode 2)*, which is depicted a the white S-Symbol. Both figures take a top down (horizontal) perspective, with cardinal points as indicated on the axes.

gradient much earlier. To further outline the significantly different behaviour of the thesis model in comparison to the ISO-9613 model, Figure 38 illustrates the predicted spectrum of the marked coordinates R1 and R2 in Figure 37. While R1 in downwind direction has only little difference in the spectrum prediction, the spectrum of R2 is severely overpredicted in every frequency range. Furthermore, both figures depict the expected high attenuation with increasing frequency and the more uniformly strong attenuation over each frequency band inside a shadow zone. Besides the fact that the behaviour of the model roughly fits expectations, the discrete change between propagation inside shadow zones and outside shadow zones create a strong contrast and models a strong directivity of the source. Furthermore, there is another odd characteristic reoccurring effect related to the ground contribution inside the shadow zone in upwind direction. In this region, which is indicated by the R3 in Figure 37a, the total sound pressure seems to drop heavily near by the source but increases shortly after. Apart from this anomaly, the attenuation further increases with distance. This effect is mainly due to the shadow zone and the contribution of the shielding which is employed for the simulation. While this effect is not necessarily contrary to the expected behaviour, it still needs to be further examined and validated against measurements. The same applies to the position marked R4, where a characteristic drop of the total pressure level of around 3 dB is visible. Particularly, this effect is not only in the marked area but spans an area between the occurrence of a shadow zone and regular

Parameter	Simulation 1	Simulation 2	Simulation 3
Source heights	105 m	105 m	105 m
Source count	20	100	40
Receiver heights	2 m	2 m	2 m
Receiver distances	up to 10 km	up to 10 km	up to 10 km
Temperature at ground level	283.15 K	283.15 K	283.15 K
Average ambient temperature	293.15 K	293.15 K	293.15 K
Temperature lapse rate	$-0.03\,\mathrm{K/m}$	$-0.03\,\mathrm{K/m}$	$0.06\,\mathrm{K/m}$
Wind speed at 10 m	8 m/s	15 m/s	15 m/s
Direction of wind	Northwest	South	South
Surface roughness length	0.05 m	0.05 m	0.05 m
Ground height variation	0 m	0 m	0 m
Ground flow resistivity	$600\,\mathrm{kPa{\cdot}s{\cdot}m^{-2}}$	$1000\,\mathrm{kPa{\cdot}s{\cdot}m^{-2}}$	$1000\,\mathrm{kPa{\cdot}s{\cdot}m^{-2}}$
Wind turbulence constant	$0.05\,\mathrm{m^{4/3}{\cdot}s^{-2}}$	$0.05\,\mathrm{m^{4/3}{\cdot}s^{-2}}$	$0.05\,\mathrm{m^{4/3}{\cdot}s^{-2}}$
Temperature turbulence constant	$0.1 \cdot 10^{-4}\mathrm{K{\cdot}s^{-2}}$	$0.1 \cdot 10^{-4}\mathrm{K{\cdot}s^{-2}}$	$0.1 \cdot 10^{-4}\mathrm{K{\cdot}s^{-2}}$

Table 19: Input parameters for wind farm simulations.

attenuation. The cause of this is related to the calculation of partial coherence. As the discrete color step indicates, in the marked region the calculation is effectively with partial coherence involved, while outside the region the calculation neglects partial coherence between the rays. As discussed previously, the interplay of the two gradients related to refraction in this region causes very light refraction, which in turn causes small differences in travel time between reflected ray and direct ray. This fact implies that the corresponding partial coherence coefficient regarding the travel time difference reaches around 99 % coherence in the lower frequency bands, which results in a much higher contribution of the ground effect. Furthermore, this behaviour is influenced by the turbulence parameters, the average ambient temperature and the ground height variation in Table 18, which are set to a relatively neutral atmosphere and homogeneously flat ground. This setting leads to illustrated behaviour, since partial coherence can occur without the disturbance of turbulence and homogeneous ground. Increasing these parameters removes the visible discrete change between incoherence and partial coherence calculation and overall increases the attenuation of the total sound pressure level due to a smaller contribution of the ground effect. Lastly, the parameter temperature at ground level and surface roughness length were examined by means of several simulations. Since both have small influence on the sonic gradient, the only notable difference is a small deviation in the overall attenuation of 0.8 dB to 5 dB with no distinct characteristic effect.
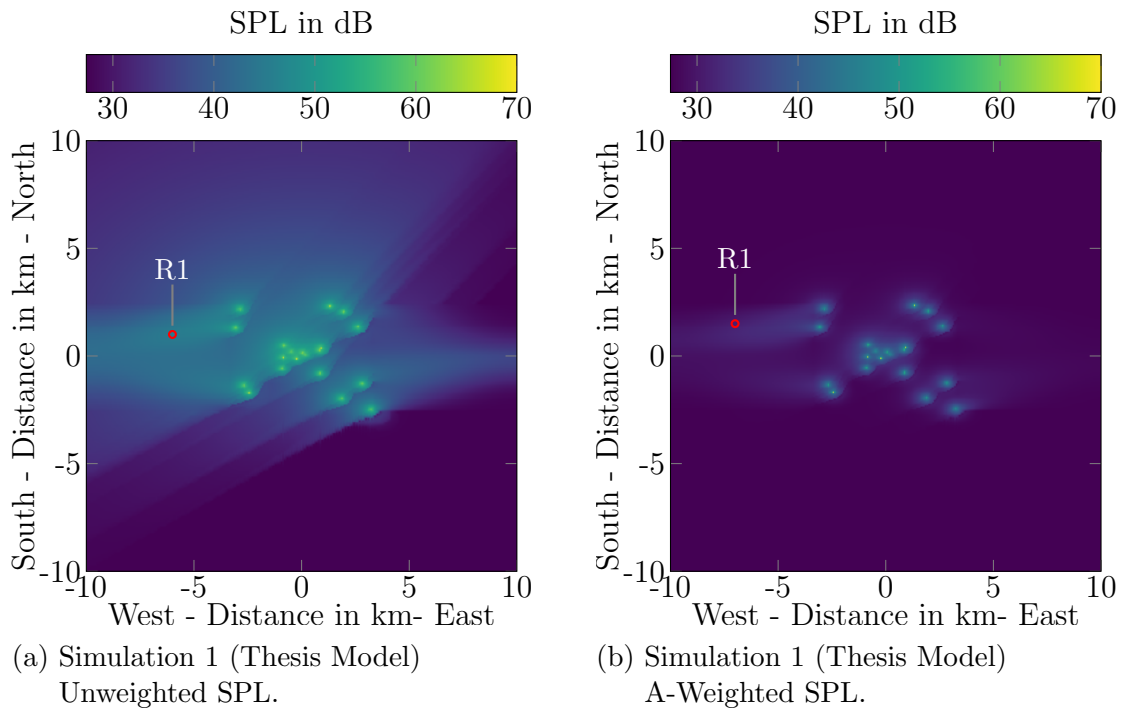
(a) Simulation 1 (Thesis Model)
   Unweighted SPL.

(b) Simulation 1 (Thesis Model)
   A-Weighted SPL.

Figure 40: Contour plot of model results in a 10 km radius around the wind farm. Input
values are provided in Table 19.

4.4.2 Simulation of a Wind Farm

In this section simulation results for complete wind farm consisting of several turbines is presented. Since there is no precise reference study with enough input data for the model available, this section is meant to only present results and briefly discuss their sincerity. However, it has to be pointed out that no detailed validation of the results is possible in the scope of this work. That said, the prior introduced reference wind turbine is employed for the wind farm simulation. The corresponding power levels are provided in Figure 36. The input parameters for the simulations are listed in Table 19. The placement of the turbines was randomized to ensure some variety. A resulting sound pressure level contour of the simulation of around 20 turbines is depicted in Figure 40. On the one hand in Figure 40a, the results are shown without any frequency weighting and on the other hand in Figure 40b, with an A-filter applied. It is clearly visible in the direct comparison of the contour plots that the frequency weighting which is commonly applied hides the sound pressure receivers are exposed to even at great distances. While the unweighted SPL is reaching up to 45 dB in a distance around 5 km away from the wind farm, the A-weighted SPL falls down to 15 dB(A) at 1 km distance to the nearest wind turbine. Figure 41 outlines this fact by illustrating the simulated spectral information. As is to be expected from an A-filter, the low frequencies from the spectrum are neglected. In this case the sound signal has predominantly low frequencies which results in the huge difference in total SPL values. At this point it is interesting to note that legal regulations usually require an
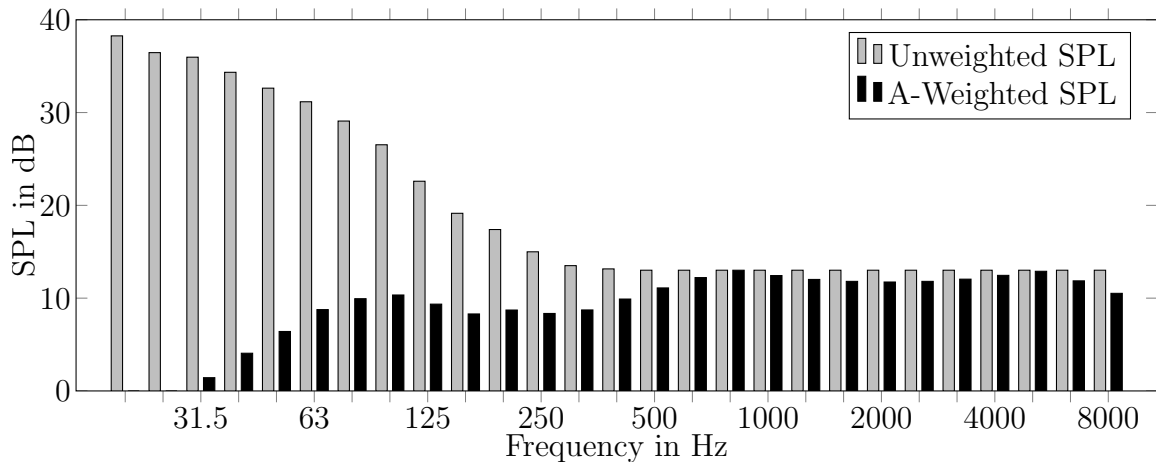
Figure 41: Comparison of the resulting spectral data at the marked coordinate R1 in Figure 40.

A-weighted sound emission level. For example, the maximum noise pollution level for residential areas in Germany is 55 dB(A) [5]. This level would be complied with for most residential areas concerning a small wind farm as shown here with only 20 turbines at a distance of 1 km. However, the unfiltered sound level transports considerably more sound energy and a remarkable proportion of low-frequency sound reaches residential areas even at a distance of up to 5 km. Simulation 2 in Figure 43a shows a simulation of a wind park with 100 turbines. Here the SPL reaches around 60 dB in a 2 km radius and up to 34 dB at 10 km radius, while the A-filtered signal barely reaches 35 dB(A) at 1 km distance. Additionally, Figure 43b includes one run with a forest marked by a red rectangular to illustrate the behaviour of scattering zones. As previously discussed, the attenuation of this area has a significant impact and also exerts a strong damping effect on the low frequency part of the signal such that the difference between unfiltered and filtered SPL falls behind such areas. For the sake of completeness, Figure 42 provides the simulation results of Simulation 1 performed by the ISO-9163 model. Here too, there is a clear difference between A-weighted and unweighted SPL, although not so distinguishable thanks to the octave band resolution. Furthermore, the aforementioned incapacity of the ISO-9613 model to consider the variety through a lot of parameters the emission contour is relatively even. As before, the immission values differ only slightly in the areas suitable for the model (downwind with low refraction) but significantly in every other area.

(a) Simulation 1 (ISO-9613)
Unweighted SPL.

(b) Simulation 1 (ISO-9613)
A-Weighted SPL.

Figure 42

(a) Simulation 2 (Thesis Model)
Unweighted SPL. 100 Turbines
are placed in $5\,\text{km}^2$ radius.

(b) Simulation 3 (Thesis Model)
Unweighted SPL. The red rectangle
mark identifies a forest.
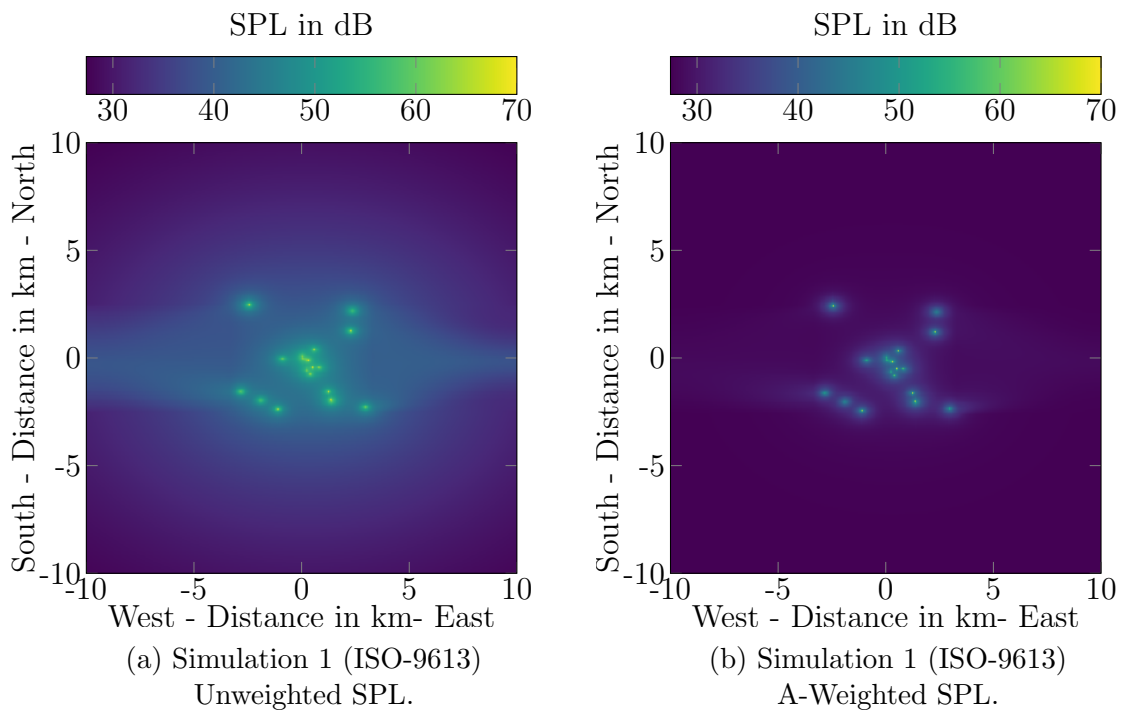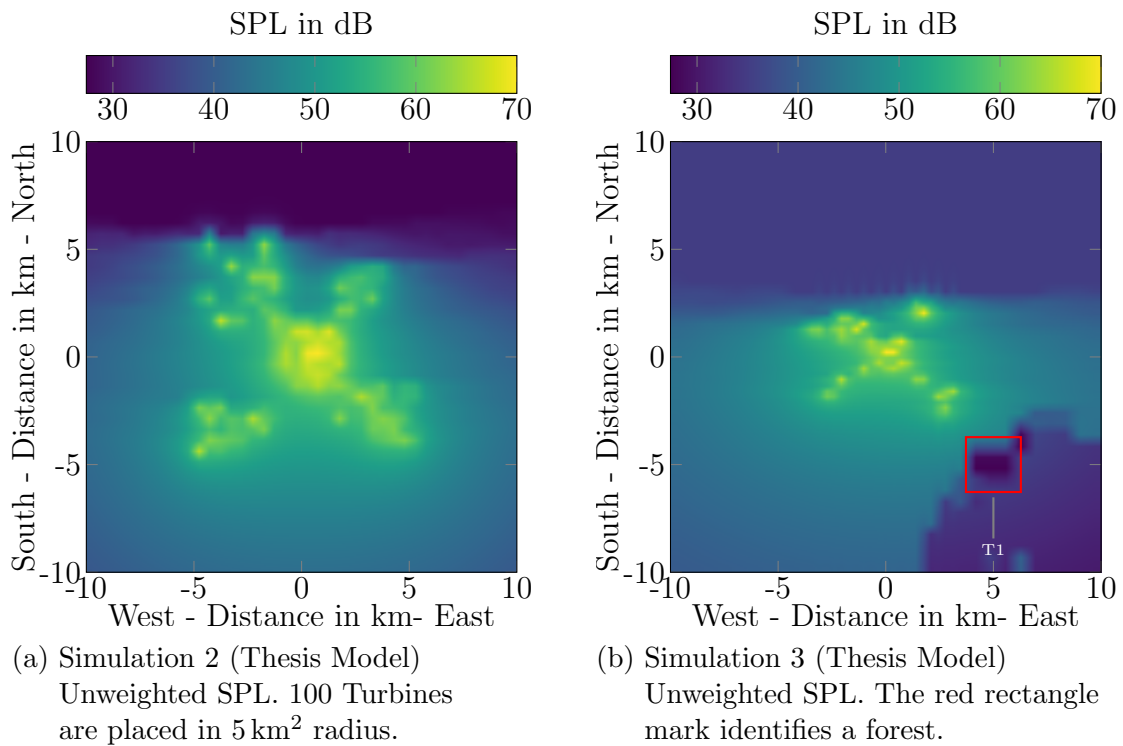
Figure 43

5 Conclusion and Future works

In the course of this work an efficient model for sound propagation concerning the noise of wind turbines has been developed. Building upon that, a model for noise propagation of wind farms was implemented and results were presented and validated against existing models and measurements. Based on the idea of determining individual effects of the atmosphere and surrounding environment with theoretical and empirical formulas, modules for all essential effects were gradually developed and combined to calculate the incoming sound in a broad spectrum at any location near a wind turbine. As this approach is well established in the area of acoustical simulation, well known effects were modelled according to the latest findings in corresponding scientific literature in great detail and additional newer and more current researched effects were added. In a direct comparison to the well established ISO-9613 model, results were generally more precise and the developed model showed greatly improved flexibility. In summary, the model foundation is predicated on the idea of individual wind turbines as point sources, which enables the determination of the energy based attenuation which only relies on the distance to the source. On that basis, the atmospheric attenuation is taken into account with only a few and easily determinable parameters. Furthermore, the impact of the atmospheric wind gradient and temperature gradient is taken into account by modelling sound as geometrical rays which are bent by temperature and wind. The modelling of sound propagation in this way enables a detailed inclusion of ground effects and scattering zones, which in relating models are often calculated purely empirically. In direct comparison with the ISO-9613 model, in which these effects are not considered at all or only by empirical equations, it showed how big the difference and the accuracy achieved by the model improves under consideration of the new approach.

As discussed in the beginning chapter, the motivation for this work was based on the current demand for practically applicable models that deliver results in realistic time without relying on input values that are difficult to measure and hardly available. To proceed on this motivation, the developed model meets expectations well. As the benchmarks of the implementation shows there is plenty of space for improvement. While the core calculation takes hardly any time and resources a very precise determination of the whole acoustic field around the source includes the calculation of up to millions of data points. Considering the sequential implementation in combination with the algorithms' complexity mainly determined by the cartesian product of receiver and source sets, the resulting runtime leads to unnecessary high resource consumption. This leads to noticeably slow computation when approaching simulations with high resolution (50 m steps) and a lot of wind turbines (>70) involved. Simulation 3 discussed in Section 4.4.2 already took around 6 hours of CPU Time and consumed a maximum of 6 GB of memory while running 16 Threads on an 16-Core Machine with 32 GB of working memory. However, it can be stated with great optimism that the model presented here is able to perform far better than comparable numerical models by simple parallelisation and more efficient data structuring in the implementation.

Besides improvements in the efficiency of the implementation, there are some further possible improvements to the theoretical foundation of the model. Room for further effects which could not yet be satisfactorily depicted at this point or were not yet relevant in the context of wind farms but could be in the future is foreseen in the design. This means that additional modules for these effects can simply be added to attenuation terms. That said as indicated by results of the ground module, future works should include the effect of multiple ground reflection, which is perfectly attachable to the current module and already available in other models such as the Nord2000 [30]. Moreover, the scattering module should be able to account for more variety of objects like housing areas in the future which can be accomplished by methods suggested in Reference [13]. Furthermore, an open point is the comprehensive inclusion of atmospheric turbulence, which has so far only been considered in the calculation of partial coherence. Finally, the model can be extended from only dealing with sound propagation to include sound generation aswell. The current state heavily depends on measurements of the sound power spectrum, which do not only involve complex methods, but is often only published by the manufacturer of the corresponding turbine.

References

[1] International Renewable Energy Agency. Global installed wind energy capacity, 2020. URL `https://www.irena.org/wind`.

[2] Emre Barlas, Wei Jun Zhu, Wen Zhong Shen, and Søren Andersen. Wind turbine noise propagation modelling: An unsteady approach. *Journal of Physics: Conference Series*, 753:022003, 09 2016. doi: 10.1088/1742-6596/753/2/022003.

[3] Emre Barlas, Wei Jun Zhu, Wen Zhong Shen, Kaya O Dag, and Patrick Moriarty. Consistent modelling of wind turbine noise propagation from source to receiver. *The Journal of the Acoustical Society of America*, 142(5):3297–3310, 2017.

[4] Henry E Bass, Louis C Sutherland, Allen J Zuckerwar, David T Blackstock, and DM Hester. Atmospheric absorption of sound: Further developments. *The Journal of the Acoustical Society of America*, 97(1):680–683, 1995.

[5] Christian Beckert and Sabine Fabricius. *TA Laerm: Technische Anleitung zum Schutz gegen Laerm mit Erlaeuterungen (2.)*. 2009.

[6] Karl Bolin, Gösta Bluhm, Gabriella Eriksson, and Mats Nilsson. Infrasound and low frequency noise from wind turbines: Exposure and health effects. *Environmental Research Letters*, 6:035103, 09 2011. doi: 10.1088/1748-9326/6/3/035103.

[7] CI Chessell. Propagation of noise along a finite impedance boundary. *The Journal of the Acoustical Society of America*, 62(4):825–834, 1977.

[8] Malcolm J Crocker. *Handbook of acoustics*. John Wiley & Sons, 1998.

[9] M.E. Delany and E. Bazley. N..: Acoustic properties of fibrous absorbent material. *Applied Acoustics*, 3(2):105 – 116, 1970.

[10] EN DIN. 61260: Bandfilter für oktaven und bruchteile von oktaven. *Deutsche Norm*, 2001.

[11] EN DIN. 61400-11: Windenergieanlagen–teil 11: Schallmessverfahren (iec 61400-11: 2012), 2013.

[12] Kaiser-Willhelm-Koog GmbH. Report of acoustical emmissions of a wind turbine generator system of the type vestas v90-2mw vcs, mode 2 near schönhagen in prignitz (germany). Report of acoustical emissions, Kaiser-Willhelm-Koog GmbH, 2005.

[13] Colin H Hansen, Con J Doolan, and Kristy L Hansen. *Wind farm noise: measurement, assessment, and control*. John Wiley & Sons, 2017.

[14] Takayuki Hidaka, Kenji Kageyama, and Sadahiro Masuda. Sound propagation in the rest atmosphere with linear sound velocity profile. *Journal of the Acoustical Society of Japan (E)*, 6(2):117–125, 1985.

[15] DIN ISO. 9613-1 (06.93) akustik. *Dämpfung des Schalls bei der Ausbreitung im Freien: Berechnung der Schallabsorption durch die Luft*, 1993.

[16] DIN ISO. 9613-2: Akustik–dämpfung des schalls bei der ausbreitung im freien–teil 2: Allgemeines berechnungsverfahren. *Beuth-Verlag, Berlin*, 1999.

[17] DIN ISO. 226: 2006–04, akustik–normalkurven gleicher lautstärkepegel (iso 226: 2003). *Beuth, Berlin*, 2006.

[18] Paul D. Joppa, Louis C. Sutherland, and Allan J. Zuckerwar. A new approach to the effect of bandpass filters on sound absorption calculations. *The Journal of the Acoustical Society of America*, 88(S1):S73–S73, 1990. doi: 10.1121/1.2029133.

[19] Kenneth Kaliski, Eddie Duncan, D Keith Wilson, and Sergey Vecherin. Improving predictions of wind turbine noise using pe modeling. In *INTER-NOISE and NOISE-CON Congress and Conference Proceedings*, pages 371–383. Institute of Noise Control Engineering, 2011.

[20] Vladislovas Katinas, Mantas Marciukaitis, and Marijona Tamašauskienė. Analysis of the wind turbine noise emissions and impact on the environment. *Renewable and Sustainable Energy Reviews*, 58:825–831, 05 2016. doi: 10.1016/j.rser.2015.12.140.

[21] Seongkyu Lee, Dongjai Lee, and Saskia Honhoff. Prediction of far-field wind turbine noise propagation with parabolic equation. *The Journal of the Acoustical Society of America*, 140(2):767–778, 2016.

[22] Reinhard Lerch, Gerhard Sessler, and Dietrich Wolf. *Technische Akustik: Grundlagen und Anwendungen*. Springer-Verlag, 2009.

[23] A L'Espérance, JR Nicolas, P Herzog, and GA Daigle. Heuristic model for outdoor sound propagation based on an extension of the geometrical ray theory in the case of a linear sound speed profile. *Applied Acoustics*, 37(2):111–139, 1992.

[24] K.J. Marsh. The concawe model for calculating the propagation of noise from open-air industrial plants. *Applied Acoustics*, 15(6):411 – 428, 1982. ISSN 0003-682X. doi: https://doi.org/10.1016/0003-682X(82)90003-2. URL `http://www.sciencedirect.com/science/article/pii/0003682X82900032`.

[25] S McBride and R Burdisso. A comprehensive hamiltonian ray tracing technique for wind turbine noise propagation under arbitrary weather conditions. In *Seventh International Meeting on Wind Turbine Noise*, pages 1–12, 2017.

[26] Henrik Møller and Christian Sejer Pedersen. Low-frequency noise from large wind turbines. *The Journal of the Acoustical Society of America*, 129(6):3727–3744, 2011.

[27] Michael Möser. *Technische Akustik -*. Springer-Verlag, Berlin Heidelberg New York, 9. aktualisierte aufl. 2012 edition, 2012. ISBN 978-3-642-30932-8.

[28] Henrik Møller and Christian Pedersen. Hearing at low and infrasonic frequencies. *Noise & health*, 6:37–57, 04 2004.

[29] Birger Plovsing. Proposal for nordtest method: Nord2000–prediction of outdoor sound propagation. *DELTA Acoustics, Report AV*, 1106(07), 2007.

[30] Birger Plovsing and J Kragh. Nord2000. comprehensive outdoor sound propagation model. part 2: Propagation in an atmosphere with refraction. *DELTA Acoustics & Vibration, Report AV*, 1851.

[31] John M Prospathopoulos and Spyros G Voutsinas. Application of a ray theory model to the prediction of noise emissions from isolated wind turbines and wind parks. *Wind Energy: An International Journal for Progress and Applications in Wind Power Conversion Technology*, 10(2):103–119, 2007.

[32] Dr. Paul Todhunter Ph.D. (auth.) Rudolf Geiger, Dr. Robert H. Aron Ph.D. *The Climate Near the Ground*. Vieweg+Teubner Verlag, 5 edition, 1995. ISBN 978-3-322-86584-7,978-3-322-86582-3.

[33] B Søndergaard and B Plovsing. Validation of the nord2000 propagation model for use on wind turbine noise. *Delta Acoustics*, 2009.

[34] Bo Sondergaard. Noise and low frequency noise from wind turbines. In *INTER-NOISE and NOISE-CON Congress and Conference Proceedings*, volume 249, pages 6201–6212. Institute of Noise Control Engineering, 2014.

[35] Renzo Tonin, James Brett, and Ben Colagiuri. The effect of infrasound and negative expectations to adverse pathological symptoms from wind farms. *Journal of Low Frequency Noise, Vibration and Active Control*, 35(1):77–90, 2016. doi: 10.1177/0263092316628257.

[36] Irene van Kamp and Frits van den Berg. Health effects related to wind turbine sound, including low-frequency sound and infrasound. *Acoustics Australia*, 46(1): 31–57, 2018.

[37] Akustische Wellen. Felder: Dega-empfehlung 101, deutsche gesellschaft für akustik, 2006.

[38] Sakae Yokoyama, Shinichi Sakamoto, and Hideki Tachibana. Perception of low frequency components in wind turbine noise. *Noise Control Engineering Journal*, 62(5):295–305, 2014.

[39] Astrid Ziemann, Hans-Jörg Ederer, Christoph Stüber, Markus Hehn, and Christian Bernhofer. Schalldämpfung durch wald (teil 1). 2016.